SUGRA AND THE STUECKELBERG EXTENSIONS: FROM COLLIDERS TO DARK MATTER

A dissertation presented

by

Daniel J. Feldman

to
The Department of Physics

In partial fulfillment of the requirements for the degree of
Doctor of Philosophy

in the field of

Physics

Northeastern University
Boston, Massachusetts
March, 2009

SUGRA AND THE STUECKELBERG EXTENSIONS: FROM COLLIDERS TO DARK MATTER

by

Daniel J. Feldman

ABSTRACT OF DISSERTATION

Submitted in partial fulfillment of the requirement
for the degree of Doctor of Philosophy in Physics
in the Graduate School of Arts and Sciences of
Northeastern University, March, 2009.

Abstract

Analyzed in detail are unified models of fundamental interactions based on supergravity (SUGRA) using effective Lagrangians valid near the grand unification scale, and $U(1)$ extensions of the Standard Model and of its supersymmetric (SUSY) extensions where the mass generation of new particle states arises through a Stueckelberg mechanism. Signals of new physics that can be measured at the Large Hadron Collider and at the Fermilab Tevatron in various final state channels are discussed in depth. Correlated signals of new physics relevant to both collider experiments and dark matter detection experiments are a focal point of the analysis and the prospects for the discovery of new physics is emphasized.

Acknowledgements

The work presented here was conducted with my Advisor, Matthews Distinguished Professor Pran Nath (Northeastern University), and with collaborators Dr. Zuowei Liu (Northeastern University and currently of the C.N. Yang Institute, SUNY Stony Brook) and with Dr. Boris Körs (at the time at MIT and CERN).

- I would like to express my gratitude to my Thesis Committee, Professors Pran Nath, Tom Taylor, and Darien Wood, for their guidance and support.
- Also, I would like to thank several faculty members at Northeastern for their help and support over the years including:
  Professors George Alverson, Arun Bansil, Ella Barberis, Haim Goldberg, Bob Lowndes, Brent Nelson, and Mike Vaughn.
- I thank the Office of the Provost at Northeastern University, and the Vice-Provost for Faculty and Graduate Education, Dr. Luis Falcón, for providing the Dissertation Completion Fellowship during my time of writing this Thesis.
- In particular I thank Zuowei Liu, who has been a collaborator on much of the research presented here; a humble friend and a strong colleague.
- I must single out Professor Pran Nath (PN).
  PN, it is an extraordinary privilege to have you as my Advisor. Thank you for your guidance, your time and commitment, and your patience. It is with the greatest level of gratitude that I thank you for the knowledge that you have imparted to me, and for showing me what it means to dedicate oneself to the search for truth in the realm of physics.
- Finally, I thank my family for their endless encouragement and support.

Contents

Chapter 1

Introduction and Overview

With the coming on-line of the Large Hadron Collider (LHC), we are entering a new and challenging phase in the quest to discover what lies beyond the Standard Model (SM) of particle physics. The LHC may very well provide us with a paradigm shift, opening a new window towards our collective understanding of the nature of fundamental physics. The exploration of the nature of new physics will be further facilitated by astrophysical data. The analysis presented in this Thesis is precisely related to the above.

We begin with a brief overview of supergravity unified models (SUGRA) and their low energy realizations. Following this, an analysis is given of the dual probes of supersymmetry through a simultaneous study of signals relevant to the direct detection of dark matter and from collider signatures of supersymmetry. It is first discussed how the LHC can allow one to decode the mechanism for the origin of dark matter production in the early universe in the framework of SUGRA models. Several correlated signatures of new physics emerge which allow for a discovery supersymmetry (SUSY) in this framework. The analysis exhibits for the first time in the literature a direct correlation between the signature space of dark matter direct detection and

the signature space of LHC signals. Indeed such a mapping between dark matter signatures and LHC signatures leads us to a more general method of pinning down the underlying model and such an approach to studying SUSY may point us to the mechanism for the production of dark matter in the early universe.

Next, an analysis is given in SUGRA/Brane models from the perspective of the Sparticle Landscape of Mass Hierarchies. Thus, in models built on the premise of supersymmetry, there is a large landscape of possible sparticle mass hierarchies, but these possibilities reduce drastically in well motivated models where supersymmetry breaking triggers electroweak symmetry breaking and the set of possible mass hierarchies becomes predictive. It is then found more generally that the nature of LHC signatures is correlated very strongly with such mass hierarchies and this is also the case for the predictions of cross sections from the scattering of neutralinos off nuclei which are relevant for dark matter direct detection experiments. Therefore, collider and dark matter experiments get closely tied together more generally. The possibility of relatively light Higgs bosons are also discussed and the convergence of constraints on light Higgses from experimental data is noted.

The second part of this Thesis focuses on collider signatures and the implications for dark matter that arise in the Stueckelberg extensions of the Standard Model and its minimal supersymmetric extension. Predictions are made for the discovery potential of narrow resonances at the Tevatron and the LHC and new candidates for dark matter and some of their experimental consequences are analyzed. We elaborate on this a bit further below.

In a broad class of models based on grand unification, on strings, and on D-Branes one expects extra Abelian gauge group factors beyond the Standard Model gauge group. It is often the case that one or more of these gauge groups remain unbroken at the grand unified scale or string scale and survive down to the electroweak scale.

The breaking of such factors at or near the electroweak scale can generate unexpected new phenomena. An interesting possibility arises when the Abelian gauge group is 'hidden' i.e. the matter fields in this sector are neutral with respect to the Standard Model (SM). The exploration of these issues can be tackled within certain low energy realizations of strings, in terms of their field theoretic manifestations. An example of this is the inclusion of Stueckelberg mass mixings in the low energy Lagrangian of the SM, as indeed such mass mixings are generic to many classes of string theories. In these extensions of the SM, the mass growth for the extra gauge bosons occurs via the so called Stueckelberg mechanism. In the simplest case, the mixing between the visible sector and the hidden sectors arises via an axionic field which is absorbed by the extra $U(1)$ vector boson rendering it massive. Upon coupling this mechanism of mass generation to the SM, which is distinctly different from the Higgs mechanism, several signatures of new physics arise that can be detected at the LHC. A very interesting consequence of the Stueckelberg mechanism that arises here is the appearance of a very narrow spin 1 resonance with a set of hypercharged enhanced decays into visible matter. Additionally, these models lead to two candidates for dark matter, one being a milli-weak Majorana fermion and the other a milli-charged Dirac fermion. These represent some of the unexpected (and testable) consequences of the hidden sector models. Further, it is also found that a class of these models can fit the anomalies seen in the PAMELA and ATIC data due to a Breit-Wigner enhancement of the dark matter annihilation cross sections in the halo of the galaxy, while the annihilations that gave rise to the relic density of dark matter also yield its correct relic abundance.

This Thesis is organized as follows: In Chapter(2) we give a very brief introduction to global and local supersymmetry and its implications. In Ch.(3) an analysis is given of the decoding of the origin of dark matter with LHC signals. In Ch.(4) the concept of Sparticle Landscapes and of Sparticle Mass Hierarchies is introduced and

correlated signatures of new physics are analyzed. In Chapters(5,6,7) we move on to the study of mass generation through the Stueckelberg mechanism. Specifically, in Ch.(5) we briefly introduce the Stueckelberg mechanism, and in Ch.(6) we study the mechanism for mass growth in supersymmetric models and explore its implications for dark matter. In Ch.(7), focus is given to the discovery potential of a light Z prime Boson at the Tevatron that manifests through the Stueckelberg mechanism. In Ch.(8), LHC signals in the context of narrow spin 1 resonances are analyzed and it is shown how they may be distinguished from models of warped geometry which also lead to narrow resonances. In Chapter (9) we generalize the Stueckelberg extensions in the framework of the SM and discuss dark matter and collider implications as well as the recent PAMELA/ATIC positron/electron excesses. In Chapter (10) we summarize and conclude.

Chapter 2

Supersymmetry and Supergravity Unification

2.1 A Brief History

Supersymmetry is an attractive symmetry for the construction of fundamental interactions in four dimensions[1] linking bosons and fermions through their field transformations. Local supersymmetry[2, 3] leads to what is referred to as supergravity. Supergravity models with chiral matter solve several phenomenological difficulties encountered in the soft breaking of global supersymmetry[4]. The minimal supergravity grand unified model[5] (mSUGRA) and its extensions including non-universalities (generally classified as SUGRA) resolves such difficulties.

To build models based on supergravity, $N = 1$ supergravity is coupled to $N = 1$ chiral multiplets and $N = 1$ gauge multiplets, the latter belonging to the adjoint representation of the gauge group [5, 6, 7]. Unlike the case of global supersymmetry, the scalar potential in the bosonic sector of the theory is not positive semi-definite, thus such a potential can lead to the breaking of supersymmetry consistent with the

vanishing of the vacuum energy. Phenomenologically viable SUGRA models rely on the concept of a so called hidden sector[8] (HS) which carry fields that may develop vacuum expectation values. The terminology 'hidden' implies simply that the fields in this sector do not carry quantum numbers of the Standard Model gauge group. Therefore, fields in the SM sector do not directly interact interact with these fields without the presence of some other underlying mechanism for mediation. In SUGRA models this underlying mediation mechanism is gravity. Thus, an intrinsic assumption in SUGRA models is that supersymmetry is broken in the hidden sector and the breaking of supersymmmetry is then communicated gravitationally to the sector where quarks, leptons and the Higgs fields reside[5]. In the context of gaugino condensation, this was discussed in Ref.[9]. SUGRA models are inherently high scale models which rely on Planck scale physics as well as the scale of grand unification. However quite remarkably, the resultant low energy theory is independent of both the Planck scale[5, 10] and the grand unification scale[5, 11, 12]. The minimal SUGRA model employs of a flavor independent Kähler metric and a gauge kinetic function that carries linear field dependence. The minimal model leads to four soft breaking parameters: the universal scalar and gaugino masses (m_0, $m_{1/2}$) and the universal (tri,bi)-linear couplings (A_0, B_0) [5]. In addition the model has a bi-linear Higgs mixing parameter μ [5, 6, 13, 14]. String models allow for Kähler potentials to have such a bi-linear Higgs term [15], [see also [16], and [17] in [18]], and through a Kähler transformation the μ term can be transported from the Kähler potential to the superpotential. A truly remarkable aspect of SUGRA models is that they dynamically lead to the breaking of electroweak symmetry[5]. Such a mechanism is natural in the context of radiative electroweak symmetry breaking (REWSB)[19, 20] through renormalization group evolution.

In the analysis presented in this Thesis, one of our focal points will be on soft

breaking from gravity mediation with GUT scale unification[5] (for an early foundational review see [21]) which give rise to experimentally testable signatures of low energy supersymmetry (for a detailed review and analysis see [22]). In general, SUGRA models give rise to a host of new signatures directly testable at the colliders and such models remain as leading candidates for the discovery of new physics at the LHC. Further, shortly after the discovery of viable SUGRA models[5, 11, 12] , around the same time when importance progress on SQCD was made [23] , it was proposed that supersymmetric models could in fact give rise to gaugino dark matter [24], and in particular neutralino dark matter[25], leading to large signatures of missing energy (originally referred to as UFOs[6][1]). Shortly after this great period of discovery, it was realized that SUGRA models can arise as the field point limit of string theory (see ex: [26]).

We note in passing some broader issues. As discussed above, in this Thesis we will address the low energy implications of unified models as they relate to the analysis of experimental data at colliders and in dark matter experiments. Other aspects of unified models such as neutrino masses and proton decay (for a review see [27]) which depend on high scales such as GUT masses are not explored. However, it may be noted that as shown in [5] the soft parameters which control low energy phenomenology are independent of the GUT scale. However, a true unified model will need to address all issues including the ones mentioned above.

In order to make contact with testable predictions of SUGRA models, a determination is needed of the sparticle spectrum arising from boundary conditions at the scale of grand unification (where the strong, electric and weak forces unify with greater precision than in the Standard Model [2]). The earliest detailed analyses focused on

[1]Historically: Unidentified Fermionic Objects[6] - the twilight Zino, or what we now all call large amounts of missing P_T.

[2] For early analyses on gauge coupling unification see [28].

such spectroscopy were given in the 1990's[29],[30],[31]. Such a determination depends critically on the renormalization group evolution (RGE) of the soft breaking parameters. A detailed analysis of RGEs has been given in Refs. [32]. One is then in the position to make concrete predictions in supersymmetric models including predictions on the relic abundance of dark matter, and implications for the direct detection of such matter, and supersymmetric signals of new physics at colliders. This will be taken up in Chapters(3,4). A brief review of the above developments will be given below.

2.2 Global SUSY

Supersymmetry (SUSY) is simply a generalization of the Poincaré group to include a graded Lie algebra with fermionic generators. Such fermionic generators Q satisfy anti-commutating relations $\{Q_\alpha, \bar{Q}_{\dot{\alpha}}\} = 2\sigma^\mu_{\alpha\dot{\alpha}} P_\mu$, where P is the generator of translations and the generators of the supersymmetry transformations, Q, commute with P. Massless representations of the extended algebra necessary for building particle physics models consist of chiral superfields where quarks, leptons, and Higgs fields and their superpartners reside, and of vector superfields which contain the vector gauge bosons and their supersymmetric partners the gauginos.

One can construct a globally supersymmetric Lagrangian (for reviews see [33], [34], [35]) by forming products of chiral superfields (with bosonic components ϕ_i and fermionic components ψ_i) and products of chiral and a vector superfields (the vector superfields in the Wess-Zumino gauge having bosonic components v^a_μ and Majorana fermionic components λ^a, where the index a belongs to the adjoint representation of the gauge group). This Lagrangian for a single non-Abelian gauge group connecting

gauge and matter fields (GM) in 2-component notation reads

$$\begin{aligned}\mathcal{L}_{GM} &= -\frac{1}{4}v^{a\mu\nu}v^a_{\mu\nu} - i\bar{\lambda}^a\bar{\sigma}^\mu\mathcal{D}_\mu\lambda^a + \frac{1}{2}D^aD^a \\ &\quad -(\mathcal{D}^\mu\phi_i)^\dagger(\mathcal{D}_\mu\phi_i) - i\bar{\psi}^i\bar{\sigma}^\mu\mathcal{D}_\mu\psi_i - F^{i\dagger}F_i \\ &\quad -(-i\sqrt{2}g\phi^{i\dagger}(T^a)_{ij}\psi^j\lambda^a + h.c.) + gD^a\phi^{i\dagger}T^a_{ij}\phi^j - \frac{1}{2}[\psi^i\mathcal{W}_{,ij}\psi^j + h.c.].\end{aligned} \tag{2.1}$$

Here $\mathcal{W}$ is the superpotential which is a holomorphic function of chiral superfields (and at most cubic in chiral superfields) and $\mathcal{W}_{,ij} = \partial^2\mathcal{W}/\partial\phi^i\partial\phi^j$ (formally the derivatives are with respect to chiral superfields). F, D are auxiliary fields satisfying $F_i = -(\mathcal{W}_{,i})^\dagger$ and $D^a = -g\phi^{i\dagger}T^a_{ij}\phi^j$, where the gauge group generators obey $[T^a, T^b] = if^{abc}T^c$, as usual, with antisymmetric structure constants f^{abc} . For an Abelian gauge group a Fayet-Iliopoulos D-term (see Ref 2 of [1]) is allowed and the D-term can contain an extra additive constant. The gauge covariant derivative acting on scalar and fermionic matter fields $m_i = \phi_i$ or ψ_i is $\mathcal{D}_\mu m_i = (\partial_\mu m)_i + igv^a_\mu(T^a m)_i$, while for the fermions transforming in the adjoint representation of the gauge group $\mathcal{D}_\mu\lambda^a = (\partial_\mu - gf^{abc}v^b_\mu)\lambda^c$. The potential of the system is defined in terms of the auxiliary fields

$$V_{\text{Global}} = F^{i\dagger}F_i + \frac{1}{2}D^aD^a. \tag{2.2}$$

The above is trivially generalized to a product gauge group. Although the above structure is aesthetically pleasing, it suffers from the major phenomenological issue that global supersymmetry *as constructed above*, cannot be an exact symmetry of nature as in its unbroken form it predicts the presence of scalars that are mass degenerate with fermions. Therefore, if SUSY it is to be realized at all, it must be a broken symmetry as scalar masses the size of electron masses are not observed. The breaking of SUSY is complicated by the following fact: If one traces the anticommutators of

the SUSY generators this leads to a vacuum energy $\langle 0|H|0\rangle \geq 0$, and therefore the potential of the system is positive semi-definite. If SUSY is preserved, the fermionic generators Q preserve the vacuum state, i.e. $Q_\alpha|0\rangle = 0 = \bar{Q}_{\dot{\alpha}}|0\rangle$ and the energy of the ground state is 0 ($E^{\rm vac}_{\rm Unbroken} = 0$). Conversely if SUSY is broken $Q_\alpha|0\rangle \neq 0, \bar{Q}_{\dot{\alpha}}|0\rangle \neq 0$, and the ground state energy is necessarily positive, $E^{\rm vac}_{\rm Broken} > 0$. Thus the supersymmetric vacuum lies lower than the broken vacuum suggesting that it may be difficult to break supersymmetry. One could in principle add soft parameters by hand to break supersymmetry at low energy of the form[3] [4]

$$\mathcal{L}_{Soft} \sim -\left(M\lambda^a\lambda^a + h.c.\right) - \left(m^2\right)^i_j \phi^{\dagger j}\phi_i - \left(\mu^{ij}\phi_i\phi_j + y^{ijk}\phi_i\phi_j\phi_k + h.c.\right) . \qquad (2.3)$$

However this approach is plagued by the fact the simplest possible extension known with the field content of the SM (the minimal supersymmetric extension $\equiv$ MSSM) has an enormous number of free parameters, i.e., upward of a hundred[4]. These problems are avoided in the framework of local supersymmetry/supergravity [2, 3] and in particular within supergravity grand unification [5] and models based on its structure.

2.3 SUGRA Unification

As indicated previously, in order to build models based on $N = 1$ supergravity one needs to use the techniques of applied supergravity which involves the coupling of supergravity with chiral multiplets and gauge multiplets belonging to the adjoint representation of the gauge group [5, 6, 7]. The effective $N = 1$ supergravity Lagrangian depends on three arbitrary functions: the superpotential $\mathcal{W}(\phi_i)$, the Kähler

[3] A linear term in ϕ is also soft.
[4] See Ch. 8.1.1 of [36] for various counts.

potential $\mathcal{K}(\phi_i, \phi^{i\dagger})$, and the gauge kinetic function $f_{\alpha\beta}(\phi_i, \phi^{i\dagger})$, where here α, β are gauge indices for the adjoint representation. $\mathcal{W}$ and $\mathcal{K}$ enter in the effective theory only in a fixed combination through the function $\mathcal{G}$ defined by

$$-\mathcal{G} = \kappa^2\mathcal{K} + \ell n[\kappa^6 \mathcal{W}\mathcal{W}^\dagger] \ , \tag{2.4}$$

$$\text{invariant under :} \qquad \mathcal{K} \to \mathcal{K} - F(\phi_i) - F^\dagger(\phi^{i\dagger}) \quad \text{with} \quad \mathcal{W} \to e^{\kappa^2 f}\mathcal{W} \ , \tag{2.5}$$

where F is an arbitrary function of chiral fields. The Kähler metric is given by $\mathcal{K}^i_j = \mathcal{K}^{,i}_{,j} \equiv \partial^2_{\phi_i \phi^{j\dagger}}\mathcal{K} = -\kappa^{-2}\mathcal{G}^{,i}_{,j}$. Here $\kappa = 1/\overline{M}_{\rm Pl}$ is the inverse reduced Planck mass so that $\overline{M}_{\rm Pl} = (8\pi G_N)^{-1/2} = 2.4 \times 10^{18}$ GeV. Now, from a practical point of view, one of the most important results that comes out of applied supergravity is the emergence of an effective potential which is not positive semi definite [5, 7]

$$V_{\rm SUGRA} = -\kappa^{-4} e^{-\mathcal{G}} \ \left[\mathcal{G}_{,i}(\mathcal{G}^{-1})^i_j \mathcal{G}^{,j} + 3\right] + V_D \ , \tag{2.6}$$

which upon expansion reads

$$V_{\rm SUGRA} = e^{\kappa^2\mathcal{K}} \ \left[\mathcal{D}_i(\mathcal{K}^{-1})^i_j \mathcal{D}^{\dagger j} - 3\kappa^2|\mathcal{W}|^2\right] \ + V_D \ , \tag{2.7}$$

$$\mathcal{D}_i = \mathcal{W}_{,i} + \kappa^2 \mathcal{K}_{,i}\mathcal{W} \ , \tag{2.8}$$

$$V_D = \frac{g^2}{2}\Re(f^{-1}_{\alpha\beta}) D^\alpha D^\beta = \frac{g^2}{2\kappa^4}\Re(f^{-1}_{\alpha\beta})\mathcal{G}^{,i}(T^\alpha)^j_i \phi_j \mathcal{G}^{,k}(T^\beta)^l_k \phi_l \ . \tag{2.9}$$

As the potential is no longer positive definite a remarkable aspect of the supergravity formulation emerges: supersymmetry may be broken spontaneously while allowing the vacuum energy to vanish. The relevant pieces of the Lagrangian that enter into this discussion are those involving the mass terms for the spin 3/2 fermionic partner of the spin 2 graviton; the gravitino (Ψ_μ), and the mass terms for the Majorana (λ^α)

fields[5], and are exhibited below (ignoring the determinant of the vierbein)

$$\begin{aligned} \mathcal{L}_{3/2} &\ni \kappa^{-1} e^{-\mathcal{G}/2} \bar{\Psi}_\mu \Sigma^{\mu\nu} \Psi_\nu \ , \\ \mathcal{L}_{1/2} &\ni \frac{1}{4} \kappa^{-1} e^{-\mathcal{G}/2} \mathcal{G}^i (\mathcal{G}^{-1})^j_i (\partial f^*_{\alpha\beta} / \partial \phi^{*j}) \bar{\lambda}^\alpha_L \lambda^\beta_R + h.c. \ , \end{aligned} \tag{2.10}$$

where $\Sigma_{\mu\nu} = (1/4)[\gamma_\mu, \gamma_\nu]$. It is worth pointing out, that the Bosonic Lagrangian also contains gauge (*non-diagonal*) kinetic terms [5, 6, 7], $\mathcal{L}_{\rm Kin} \ni -\Re(f_{\alpha\beta}) V^{\mu\nu\alpha} V^\beta_{\mu\nu}/4$ (and the imaginary part of the dual field strength). Non diagonal field strength tensors [5, 6, 7] can have important implications and this subject will be addressed in various contexts in Ch.(9).

To achieve the breaking of supersymmetry one invokes the existence of a sector of fields which do not carry the quantum numbers of the visible sector (where the Standard Model fields reside). This hidden sector is where supersymmetry is broken via a super Higgs effect. In the SUGRA framework the only communication between the hidden sector and visible sector occurs via gravity.

Returning to the potential, with a vanishing D-term at the minimum, a flat Kähler metric $\mathcal{K} = \phi_i \phi^{i\dagger}$, on a real manifold of VEVs, one readily derives upon minimization [5, 6]:

$$\begin{aligned} \mathcal{T}_{ij} \hat{\mathcal{W}}_{,j} &= \mathcal{T}_{ij} [\partial_{\phi_j} + \kappa^2 \phi_j] \mathcal{W} = 0 \ , \\ \mathcal{T}_{ij} &= \mathcal{W}_{,ij} + \kappa^2 \left(\phi_j \mathcal{W}_{,i} + \phi_i \mathcal{W}_{,j} \right) + \kappa^4 \mathcal{K} \mathcal{W} - 2\kappa^2 \mathcal{W} \delta_{ij} \ , \end{aligned} \tag{2.11}$$

where all fields in the above are evaluated at the minimum of the potential. One then has $\hat{\mathcal{W}}_{,j} = 0$ alone breaks the gauge symmetry but not supersymmetry as the VEV of chiral matter satisfies $\langle \delta\chi_L \rangle \ \propto \ \langle \hat{\mathcal{W}}_{,j} \rangle = 0$. Thus supersymmetry breaking is

[5] We have switched to four component notation here for the moment.

accomplished if at least one of the $\hat{\mathcal{W}}_{,j} \neq 0$ implying at least one eigenvalue of $\mathcal{T}_{ij} = 0$. This illustrates rather explicitly the breaking of both SUSY and gauge symmetry in a locally supersymmetric model[5, 6].

The simplest way to achieve a phenomenologically viable breaking of supersymmetry is through a singlet scalar field Z with a superpotential split between the visible and hidden sectors of the form $\mathcal{W} = \mathcal{W}_{VS} + \mathcal{W}_{HS}$ with $\mathcal{W}_{HS} = m^2(Z + B)$ and assuming a flat Kähler potential in the HS with $\langle Z \rangle = O(M_{\rm Pl})$. Direct interactions between the VS and HS will lead to sparticle masses $O(M_{\rm Pl})$ in the visible sector however such a problem is avoided if the two sectors communicate via gravitational interactions[5, 10]. Further, in the above example the tuning of the vacuum energy to zero arises with a particular value of B. The above phenomenon is a consequence of the super Higgs effect. Thus after spontaneous breaking the spin 3/2 gravitino absorbs the fermionic partner of the chiral field Z with mass given by

$$m_{3/2} = \kappa^{-1} \exp(-\langle \mathcal{G} \rangle/2) = \kappa^2 \exp(\kappa^2 \langle Z \rangle^2/2) \cdot |\langle \mathcal{W}(Z) \rangle| \ , \tag{2.12}$$

i.e., the gravitino, receives a mass of $m_{3/2} \sim \kappa m^2$ implying that $m \sim 10^{10-11}$ GeV will lead to $m_{3/2}$ in the electroweak to TeV region.

More generally, the conditions under which the soft breaking in the minimal supergravity model are derived are summarized as follows: (i) There exists a hidden sector, i.e. minimally the presence of a gauge singlet which breaks supersymmetry through a super Higgs effect giving mass to the gravitino; (ii) The two sectors, the hidden and the visible, interact only gravitationally; (iii) The Kähler potential is generation independent; (iv) The gauge kinetic $f_{\alpha\beta}$ is diagonal with higher order terms in its expansion assumed negligible, suppressed by powers of the Planck mass. This

then gives rise to soft terms of the form [5, 12, 37]

$$V_{SB} = V_{\rm Global} + m_0^2 \phi^{i\dagger}\phi_i + \frac{1}{2} m_{1/2} \bar{\lambda}^\alpha \lambda^\alpha + (A_0 \mathcal{W}^{(3)} + B_0 \mathcal{W}^{(2)} + h.c.), \quad (2.13)$$

where $\mathcal{W}^{(2)} = \mu_0 H_1 \cdot H_2$ and, $H_{i=1,2}$ are Higgs doublets, and $\mathcal{W}^{(3)}$ is tri-linear in superfields and A_0 has mass dimension in this notation, while $m_{3/2} \propto m_0$, and $m_{1/2}, A_0, B_0\mu_0$ are all of the same relative size $\approx \kappa m^2 \lesssim$ TeV.

Now, the result of Eq.(2.13) arises from the simplest Kähler metric and gauge kinetic function. It is however possible (and perhaps likely) that small deviations from flatness will manifest at the string scale and influence low energy physics. More generally, if the gauge kinetic energy function carries field dependence then after the spontaneous breaking of supersymmetry the above leads to gaugino masses. If $f_{\alpha\beta}$ transforms as a singlet of the underlying gauge groups the gaugino masses remain universal. Conversely, if $f_{\alpha\beta}$ transform as non-singlet irreducible representations then the gaugino masses will be non-universal at the high scale. Additionally a more general form of the Kähler potential which is not flavor blind will give rise to non-universalities in the soft breaking parameters in other sectors [13, 16, 17, 38]. Non-universalities typically arise in strings and in D-Brane models and Ibanez et. al [17] have devised a very convenient parametrization of generic soft breaking. This will be utilized in Chs.(4.4,4.5).

It should be noted that non-universalities are highly constrained by experimental data especially from constraints on flavor changing processes. Still, it is possible to find classes of viable models with non-universalities consistent with all the relevant experimental constraints. Indeed, recently there has been progress on building semi-realistic models with $N = 1$ supersymmetry based on D-Branes [39]. In certain classes of these models moduli are assumed to give rise to spontaneous breaking of

supersymmetry in the hidden sector with such moduli playing the role of Polonyi fields[16] in the breaking of supersymmetry. Particular classes of models include those based on orientifold compactifications of type II string theories with D-Branes that support semi-realistic chiral gauge theories for which the Kähler metric has been explicitly constructed [40]. Computations of disk scattering amplitudes have been given in [41] (see also [42],[43]). The Kählers arising from these calculations are often complicated in their structure containing functions of products of moduli fields $M = \{s, t_m, u_m\}$ and angular variables describing the orientation of the Branes in the compactified space, the stretching of strings between Brane stacks, and also set the conditions for the model to be supersymmetric. These models also include gauge kinetic functions that depend on the moduli and wrapping numbers. We will discuss some phenomenology of these scenarios in Chapter(4). The point to be made here is that indeed we can begin to make important progress on testing such scenarios [44],[45], [46].

2.3.1 Low energy realizations

The simplest scenario is that the field content of low energy supersymmetry is described by the minimal particle content. For the case of the MSSM, which is the minimal supersymmetric generalization of the SM with product gauge group $G_{SM} = SU(3)_C \times SU(2)_L \times U(1)_Y$, the R-Parity preserving superpotential [6] is taken to be quadratic and cubic with[7]

$$\mathcal{W}^{(2)} = \mu \Phi_{H_u} \Phi_{H_d}; \quad \mathcal{W}^{(3)} = \Phi_{\bar{u}} Y^u \Phi_Q \Phi_{H_u} - \Phi_{\bar{d}} Y^d \Phi_Q \Phi_{H_d} - \Phi_{\bar{e}} Y^l \Phi_L \Phi_{H_d} \ , \quad (2.14)$$

[6] R-Parity is Z_2 symmetry which will be assumed intact throughout this analysis.
[7] Later we will use the notation $H_1 = H_d$, and $H_2 = H_u$.

where Y are in general 3×3 matrices in flavor space containing Yukawa couplings. In the gauge sector, the vector superfields are $V^{A=1-8}, V^{\alpha=1,3}, V$ transforming as $(8,1,0),(1,3,0),(1,1,0)$ respectively under G_{SM} introducing new spin 1/2 particles, namely the gaugino colored octet and the weak and hypercharge gauginos. In the chiral sector two Higgs superfields are introduced whose scalar doublet fields carry hypercharge of opposite sign to avoid anomalies from the presence of their fermionic partners. Finally, new scalar fields are introduced for each fermionic matter state of the SM (sfermions = squarks + sleptons). In terms of the MSSM the soft terms

Chiral superfield	$(SU(3)_{\rm rep}, SU(2)_{\rm rep}, Y/2)$	spin 1/2	spin 0
Φ_Q	$(3,2,+1/6)$	(u_L, d_L)	$(\tilde{u}_L, \tilde{d}_L)$
$\Phi_{\bar{u}}$	$(\bar{3},1,-2/3)$	$u_R^\dagger$	$\tilde{u}_R^\dagger$
$\Phi_{\bar{d}}$	$(\bar{3},1,+1/3)$	$d_R^\dagger$	$\tilde{d}_R^\dagger$
Φ_L	$(1,2,-1/2)$	(ν_e, e_L)	$(\tilde{\nu}_e, \tilde{e}_L)$
$\Phi_{\bar{e}}$	$(1,1,+1)$	$e_R^\dagger$	$\tilde{e}_R^\dagger$
Φ_{H_u}	$(1,2,+1/2)$	$(\tilde{H}_u^+, \tilde{H}_u^0)$	(H_u^+, H_u^0)
Φ_{H_d}	$(1,2,-1/2)$	$(\tilde{H}_d^0, \tilde{H}_d^-)$	(H_d^0, H_d^-)
Vector superfield	$(SU(3)_{\rm rep}, SU(2)_{\rm rep}, Y/2)$	spin 1/2	spin 1
V^A	$(8,1,0)$	$\tilde{\lambda}_g$	g
V^α	$(1,3,0)$	$\tilde{\lambda}_W \ni \tilde{\lambda}^3, \tilde{\lambda}_\pm$	$A_\mu^3, A_\mu^\pm$
V	$(1,1,0)$	$\tilde{\lambda}_Y$	B_μ

Table 2.1: Chiral and Vector Superfields of the MSSM: In the chiral/matter sector, in addition to quarks and leptons, there are squarks, sleptons ($\times 3$ families), there is an an extra Higgs doublet, and the fermionic partners, the Higgsinos. In the gauge sector in addition to the $SU(3)_C \times SU(2)_L \times U(1)_Y$ gauge bosons there is a set of corresponding gauginos.

generated by supergravity in Eq.(2.13) read (following a similar notation to [47] and suppressing gauge/family indices)

$$\begin{aligned} -\mathcal{L}_{soft} \;\ni\; & m_{H_u}^2 H_u^\dagger H_u + m_{H_d}^2 H_d^\dagger H_d + (B\mu H_u H_d + h.c.) \\ & + \tilde{Q}^\dagger M_{\tilde{Q}}^2 \tilde{Q} + \tilde{L}^\dagger M_{\tilde{L}}^2 \tilde{L} + \tilde{\bar{u}} m_{\tilde{u}}^2 \tilde{\bar{u}}^\dagger + \tilde{\bar{d}} m_{\tilde{d}}^2 \tilde{\bar{d}}^\dagger + \tilde{\bar{e}} m_{\tilde{e}}^2 \tilde{\bar{e}}^\dagger \end{aligned} \tag{2.15}$$

$$+(\tilde{\bar{u}} h_u \tilde{Q} H_u - \tilde{\bar{d}} h_d \tilde{Q} H_d - \tilde{\bar{e}} h_e \tilde{L} H_d + h.c.) \ ,$$
$$+\frac{1}{2}(M_3 \tilde{\lambda}_g \tilde{\lambda}_g + M_2 \tilde{\lambda}_W \tilde{\lambda}_W + M_1 \tilde{\lambda}_Y \tilde{\lambda}_Y + h.c.) \ ,$$

where $h_{u,d,e}$ are 3×3 matrices (in general complex) in the flavor space and the $M^2_{\tilde{Q}}$, $M^2_{\tilde{L}}$, $m^2_{\tilde{u}}$, $m^2_{\tilde{d}}$, and $m^2_{\tilde{e}}$ are 3×3 and Hermitian.

As previously noted, another remarkable aspect of soft breaking is that it leads to spontaneous breaking of the electroweak symmetry [5], and such a breaking may be accomplished radiatively (for a useful review see [48]). To exhibit this, consider the effective scalar potential constructed out of the Higgs F terms (i.e the derivative of the superpotential) and D terms of the Higgs sector, and the first line of Eq.(2.15). Defining $H_{(1,2)} = H^0_{(d,u)}$ the renormalization group improved scalar potential is

$$\begin{aligned} V &= m_1^2|H_1|^2 + m_2^2|H_2|^2 - m_3^2(H_1 H_2 + h.c.) \\ &+ \frac{(g_2^2 + g_Y^2)}{8}(|H_1|^2 - |H_2|^2)^2 + \Delta V_1, \\ \Delta V_1 &= (64\pi^2)^{-1} \sum_a (-1)^{2s_a}(2s_a+1) M_a^4 \left[ln \frac{M_a^2}{Q^2} - \frac{3}{2} \right] \ . \end{aligned} \tag{2.16}$$

The term ΔV_1 is the one loop correction [49, 50] to the effective potential. Here s_a is the spin of the particle a, and all parameters, run with scale and are subject to boundary conditions $\alpha_2(0) = \alpha_G = \frac{5}{3}\alpha_Y(0)$; $m_i^2(0) = m_0^2 + \mu_0^2$, $i = 1, 2$; and $m_3^2(0) = -B_0\mu_0$. Electroweak symmetry breaks down when the determinant of the Higgs mass^2 matrix turns negative (i) $m_1^2 m_2^2 - 2m_3^4 < 0$, and (ii) $m_1^2 + m_2^2 - 2|m_3^2| > 0$, where the second condition is the requirement that the potential be bounded from below. Minimization of the potential, leads to (a) $M_Z^2 = 2(\mu_1^2 - \mu_2^2 \tan^2\beta)(\tan^2\beta - 1)^{-1}$, and (b) $\sin 2\beta = 2m_3^2(\mu_1^2 + \mu_2^2)^{-1}$, where $\mu_i^2 = m_1^2 + \Sigma_i$ where Σ_i is the loop correction [51] and $\tan\beta = v_2/v_1$ is the ratio of the Higgs VEVs. The electroweak symmetry breaking constraint (a) can be used to fix μ using the experimental value

of the Z boson mass M_Z, and the constraint (b) can be utilized to eliminate B_0 in favor of $\tan\beta$. Therefore, the supergravity model at low energy can be parametrized by $(m_0, m_{1/2}, A_0, \tan\beta, sign(\mu))$.

The philosophy should now be evident. Four parameters and a sign induced by the gravitational mechanism for breaking of SUSY can be used to generate the low energy spectrum through renormalization group evolution and the radiative breaking of electroweak symmetry. Thus, a theoretically well motivated and applicable approach to testing supersymmetry is summarized as follows [29, 31, 30] :

- Start from a High Scale model where supersymmetry is spontaneously broken.
- Specify the the low energy field content (in the discussion here, the MSSM).
- Implement the Renormalization group improved effective Higgs Potential.
- Run the RGEs from the high scale (M_G) to the electroweak scale (M_Z), or the scale at which REWSB occurs, and calculate all the sparticle masses from knowledge of 4 parameters and a sign. In the case of non-universalities implement an extended parameter set.
- Impose experimental constraints and determine the viable model.
- Test such model predictions by examining their collider and astrophysical signatures.

A sample of recent works based on this general philosophy with emphasis on LHC predictions from the high scale include [52, 53, 54, 55, 56, 57, 58, 59, 45, 60, 61, 62, 63].

2.3.2 The Spectra

In the MSSM there are 32 massive supersymmetric particles including the Higgs Bosons. There are the neutral Higgs mass eigenstates $\Phi \equiv (h, H, A)$, the first two be-

ing CP even and the third CP odd, and one charged Higgs mass from the states $H^{\pm}$. In the gaugino-Higgsino sector there are two charged mass eigenstates (charginos) $\tilde{\chi}^{\pm}_{i=1,2}$, four charge neutral states (neutralinos) $\tilde{\chi}^{0}_{i=1,4}$, and finally there is the Majorana gluino mass. In the sfermion sector, before diagonalization, there are 9 scalar leptons (sleptons) which are superpartners of the leptons denoted with left and right chirality to identify them as superpartners of the leptons: $\{\tilde{e}_{L,R}, \tilde{\mu}_{L,R}, \tilde{\tau}_{L,R}, \tilde{\nu}_{e_L}, \tilde{\nu}_{\mu_L}, \tilde{\nu}_{\tau_L}\}$. Finally there are 12 squarks which are the superpartners of the quarks and are represented by: $\{\tilde{u}_{L,R}, \tilde{c}_{L,R}, \tilde{t}_{L,R}, \tilde{d}_{L,R}, \tilde{s}_{L,R}, \tilde{b}_{L,R}\}$. Mass diagonal slepton and squark states will in general be mixtures of L, R states.

After the neutral components of the Higgs doublets obtain VEVs, the analogues of the first and third terms on the third line of Eq.(2.1) and the the last term involving the electroweak gauginos in Eq.(2.15) give rise to neutralino and chargino mass matrices. For the neutral sector one has, in the basis $(\tilde{\lambda}_Y \ \tilde{\lambda}^3_W \ \tilde{H}^0_d \ \tilde{H}^0_u)$

$$M_{\tilde{\chi}^0} = \begin{pmatrix} M_1 & 0 & -M_Z s_W c_\beta & M_Z s_W s_\beta \\ 0 & M_2 & M_Z c_W c_\beta & -M_Z c_W s_\beta \\ -M_Z s_W c_\beta & M_Z c_W c_\beta & 0 & -\mu \\ M_Z s_W s_\beta & -M_Z c_W s_\beta & -\mu & 0 \end{pmatrix},$$

where θ_W is the weak angle, $s_W = \sin\theta_W$, $s_\beta = \sin\beta$, etc. For the charged sector

$$M_{\tilde{\chi}^\pm} = \begin{pmatrix} 0 & M_\pm^T \\ M_\pm & 0 \end{pmatrix}, \quad M_\pm = \begin{pmatrix} M_2 & \sqrt{2} M_W s_\beta \\ \sqrt{2} M_W c_\beta & \mu \end{pmatrix},$$

with $\lambda_+^T = (\tilde{\lambda}^+ \ \tilde{H}_u^+)^T$ and $\lambda_-^T = (\tilde{\lambda}^- \ \tilde{H}_d^-)^T$ such that in the diagonal basis, $\chi_\pm^T = (\chi_1^\pm \ \chi_2^\pm)^T$ with $\chi_+ = V\lambda_+$ and $\chi_- = U\lambda_-$ leading to $M_{\chi^\pm}^{\rm Diag} = U^* M_\pm V^{-1}$, where U, V are unitary matrices.

The squark and slepton physical masses arise from the second and third line Eq.(2.15) and and the F and D terms of the potential. Thus for example, assuming

$h_f = Y_f A_f$ then in the s-chiral basis one has

$$\mathcal{L}_{\tilde{f}} = -\begin{pmatrix} f_L^\dagger & f_R^\dagger \end{pmatrix} \begin{pmatrix} M_{\tilde{f}}^2 + m_f^2 + \Delta_f^L & m_f(A_f^* - \mu\hat{\beta}) \\ m_f(A_f - \mu^*\hat{\beta}) & m_{\tilde{f}}^2 + m_f^2 + \Delta_f^R \end{pmatrix} \begin{pmatrix} f_L \\ f_R \end{pmatrix} ,$$

where

$$\Delta_f^L = (T_{3f} - Q_f s_W^2) M_Z^2 \cos(2\beta) \qquad \Delta_f^R = (Q_f s_W^2) M_Z^2 \cos(2\beta) , \tag{2.17}$$

and where Q_f is fermionic charge and for up scalars $\hat{\beta} = \cot\beta$ while for down scalars $\hat{\beta} = \tan\beta$. Note that the mass and couplings in the mass^2 matrices are running parameters (for an introduction to calculating sparticle masses through the RGEs see [64, 65, 47],[66],[67])

At tree level the CP odd Higgs mass is simply $M_A = \sqrt{2|\mu B|/|\sin 2\beta|}$ and the charged Higgses satisfy $M_{H^\pm} = \sqrt{M_A^2 + M_W^2}$. The CP even Higgs mass receives a relatively large radiative correction[68] with the largest effect coming from the top (s,q)uark Yukawa couplings. The mass of the light CP even Higgs is bounded above in SUGRA models roughly by $m_h \lesssim 130$ GeV, and is predicted within a ~ 30 GeV mass spread, while in a complete generic MSSM one can push the limit up by about 20 GeV. In singlet Higgs extensions there is the ability to push the light CP even Higgs mass up further. The gluino mass receives radiative corrections at around the 25% level from quark squark loops (see [69]) and corrections to the squark, slepton and gaugino masses can be modest [70].

2.3.3 Branches of REWSB

It is known that there are two branches of the parameter space that follow from the radiative breaking of the electroweak symmetry. These branches are labeled by

their geometrical structure, namely an Ellipsoidal Branch and a Hyperbolic Branch (as discovered in Ref. 1 of [71]). These branches are intimately connected to the μ parameter and the radiative breaking equations which determine it. In Ref. 1 of [71] it was shown that $C_1 m_0^2 + C_3 m_{1/2}'^2 + C_2' A_0^2 + \Delta\mu_{loop}^2 = \mu^2 + \frac{1}{2} M_Z^2$, where $m_{1/2}' = m_{1/2} + \frac{1}{2} A_0 C_4/C_3$, and where C_i are functions of gauge and Yukawa couplings and $\Delta\mu^2$ are loop corrections. For small to moderate values of $\tan\beta$ the loop corrections are relatively small. In this case one finds that the soft parameters for fixed μ lie on the surface of an ellipsoid and the constraint becomes

(i) Ellipsoidal Branch:

$$\frac{m_{1/2}'^2}{a^2} + \frac{m_0^2}{b^2} + \frac{A_0^2}{c^2} \simeq 1; \quad m_{1/2}'^2 = m_{1/2} + cA_0. \tag{2.18}$$

(ii) Hyperbolic Branch: A very interesting phenomenon exhibited in the analysis of Ref. 1 of [71] is that multi-TeV squarks and sleptons can emerge in certain regions of the parameter space with a small amount of fine tuning. We reproduce below the argument of the work of Ref. 1 of [71] as to how this comes about. The important factor here are the loop corrections to the μ parameter which for certain regions of the supergravity parameter space can be rather significant. However, the size of the loop corrections to μ depends critically on the scale Q_0 where the minimization of the effective potential is carried out. In fact, for the case at hand, there is generally a strong dependence on Q_0 for both the tree and the loop contributions to μ, which however, largely cancel in the sum, leaving the total μ with a sharply reduced but still non-negligible residual Q_0 dependence. Now the choice of the value of Q_0 is rather arbitrary and one can choose any value of Q_0 for convenience. An interesting choice for the value of Q_0 is the point where the loop corrections to μ are rather small. It turns out that typically the Q_0 value where the loop correction to μ is minimized is

roughly the average of the smallest and the largest sparticle masses, a value not too far from $\sqrt{m_{\tilde{t}_L} m_{\tilde{t}_R}}$, which is also the Q_0 value where typically the 2-loop correction to the Higgs mass are minimized. The choice of such a Q_0 leads often to the case $\text{sign}(C_1(Q_0)) = -1$. In this circumstance Eq.(2.18) turns from an equation of an ellipsoid to that of a hyperboloid and hence such a branch is appropriately called the Hyperbolic Branch (HB) of REWSB so that [71]

$$\frac{m'^2_{1/2}}{\alpha^2(Q_0)} - \frac{m_0^2}{\beta^2(Q_0)} \simeq \pm 1 \ , \tag{2.19}$$

where α, β are functions of the μ, the Z mass, A_0, and the coefficients C_i (see Ref. 1 of [71]). If indeed nature has chosen the hyperbolic branch, the lightest particles will be the light Higgs and $\chi_1^0, \chi_2^0, \chi_1^\pm$, with a reasonably light gluino mass in many cases, while the scalars would be rather heavy. We will discuss this scenario in further detail shortly.

2.3.4 Dark Matter

Relic Density

The principle behind the analysis of relic (leftover) density of dark matter (DM) is as follows: The early universe was a hot dense soup of rapidly annihilating particles. At some epoch, these particles were all in thermal equilibrium. As the universe expanded and cooled down, the reaction rates of these particles became smaller than the expansion rate (H) (the Hubble function), and the particles were no longer able to annihilate rapidly enough to maintain thermal equilibrium. As a consequence, these particles no longer maintained the ability to interact with the cosmic soup and they decoupled. Their total number became locked in at a freeze-out temperature, however their number density became depleted, or diluted, with the expanding volume of the

universe.

The analysis of relic density involves the total number density $n = \sum_i n_i$, where n_i are the number of particle species of species i that survived annihilation and eventually decay into χ_1, the lightest surviving particle. The analysis is governed by the Boltzmann evolution equation [72]

$$\frac{dn}{dt} = -3Hn - \sum_{ij} \langle \sigma_{ij} v_{ij} \rangle (n_i n_j - n_i^{\rm eq} n_j^{\rm eq}) \ . \tag{2.20}$$

Here σ_{ij} are the cross sections for annihilation of fermionic particle species i, j, and $n_i^{\rm eq}$ is the number density of χ_i in thermal equilibrium. The approximation $n_i/n = n_i^{\rm eq}/n^{\rm eq}$ gives the well known

$$\frac{dn}{dt} = -3nH - \langle \sigma_{\rm eff} v \rangle (n^2 - (n^{\rm eq})^2), \tag{2.21}$$

where the bracket denotes thermal average with a normalized Boltzmann distribution and the effective cross section and velocity of annihilating matter enter via

$$\sigma_{\rm eff} v = \sum_{i,j} \sigma_{ij} v_{ij} \gamma_i \gamma_j. \tag{2.22}$$

Here the γ_i are the Boltzmann suppression factors [73] and are given by

$$\gamma_i = \frac{n_i^{\rm eq}}{n^{\rm eq}} = \frac{g_i (1+\Delta_i)^{3/2} e^{-\Delta_i x}}{\sum_j g_j (1+\Delta_j)^{3/2} e^{-\Delta_j x}} \ , \quad x \equiv m_1/T, \quad X \equiv 1/x. \tag{2.23}$$

In the above $v_{ij} = \sqrt{(p_i \cdot p_j)^2 - m_i^2 m_j^2}/(E_i E_j)$ and the units are taken with the Boltzmann constant $K_B = 1$, and g_i are the spin degrees of freedom of the particles and $\Delta_i = (m_i - m_1)/m_1$.

The freeze-out temperature is then determined iteratively through

$$x_f = ln\left[x_f^{-1/2}\langle\sigma_{eff}v\rangle m_1\sqrt{\frac{45}{8\pi^6 N_f G_N}}\right], \tag{2.24}$$

where N_f is number of degrees of freedom at freeze-out, whose value is roughly 100. Numerically one finds $x_f^{-1} = X_f = T_f/m_1 \sim 1/20$ for DM in the mass range 50-1000 GeV. The relic density of cold dark dark matter (CDM) is determined through the ratio $\Omega_{\chi_1} = \rho_{\chi_1}/\rho_c$ where $\rho_c = 3H_0^2/(8\pi G_N) = h_0^2 \times 8.1 \times 10^{-47}\text{GeV}^4$ is the critical closure energy density of the universe and h_0 is the rescaled Hubble constant related to H_0 via $H_0 = h_0 100\text{Km/sec/Mpc}$. The density ρ_{χ_1} is

$$\rho_{\chi_1} = m_1 n_{\text{NR}}^{\chi_1}(T_\chi) = (4\pi^3/45)^{1/2} M_{\text{Pl}}^{-1}(T_\chi/T_\gamma)^3 T_\gamma^3 N_f^{1/2}\left[\int_0^{X_f}\langle\sigma_{\text{eff}}v\rangle dX\right]^{-1}. \tag{2.25}$$

This may be put in a more useful form taking into account both neutrino and the LSP decoupling, by eliminating $(T_\chi/T_\gamma)^3$, the standard result is

$$\Omega_{\chi_1}h_0^2 = \frac{1.07\times 10^9\text{GeV}^{-1}}{N_f^{1/2}M_{\text{Pl}}}\left[\int_0^{X_f}\langle\sigma_{\text{eff}}v\rangle dX\right]^{-1}. \tag{2.26}$$

From here on we will drop the subscript "0" on h_0. Eq.(2.26) provides a starting point for calculating the relic density under standard assumptions. However, the spin degrees of freedom are $g_{spin} = 2$ for Majorana DM and for a Dirac DM, $g_{spin} + \bar{g}_{\text{spin}} = 2 + 2 = 4$. For Dirac DM a factor of 2 enters in the number density relative to the Majorana case as can easily be seen by noting $n_{\text{NR}}^{\chi} = n_{\text{NR}}^{\bar{\chi}}$ (see ex: [74]). For the case of SUSY, the thermally averaged cross sections depend on a large number of possible annihilation channels. We will discuss this in a bit more detail later. A listing of such channels may be found in Table 3 of [75] and the the current DarkSusy (DS) manual (available on the DS webpage).

Direct Detection

As will be discussed in detail shortly, experiments are actively attempting to detect the presence of WIMPS (weakly interacting massive particles) [8] via their spin dependant and spin independent scattering with nuclei. For SUSY models the WIMP dark matter will be the LSP (lightest R-parity odd sparticle). The WIMPs have a velocity distribution near the earth and in the local galactic halo, and they are travelling with non relativistic speed order $0.001c$. This then translates into the fact that their momentum transfer is very small (order 100 MeV for LSP masses of order 100 GeV), and therefore the relevant interactions for the direct detection of DM may be calculated in the limit of zero momentum transfer in collisions with nuclei. For the case of the MSSM, the interaction Lagrangian relevant to this discussion is given by [77][78]

$$\mathcal{L} = \bar{\chi}\gamma^{\mu}\gamma^{5}\chi\bar{q}_i\gamma_{\mu}(\alpha_{1i}+\alpha_{2i}\gamma^{5})q_i+\alpha_{3i}\bar{\chi}\chi\bar{q}_iq_i+\alpha_{4i}\bar{\chi}\gamma^{5}\chi\bar{q}_i\gamma^{5}q_i+\alpha_{5i}\bar{\chi}\chi\bar{q}_i\gamma^{5}q_i+\alpha_{6i}\bar{\chi}\gamma^{5}\chi\bar{q}_iq_i \ . \tag{2.27}$$

Experimental sensitivity currently best allows for the probes of the spin independent cross section for neutralinos scattering elastically off target nuclei. In terms of the reduced mass of the neutralino and the target system ($\mu_{\chi T}$) one has

$$\sigma_{\chi(T)} = \frac{4\mu_{\chi T}^2}{\pi}(Zf_p + (A-Z)f_n)^2 \ , \tag{2.28}$$

where (Z, A) are the atomic (number,mass) of the nucleus, and interactions with the quarks in the target nuclei through t-channel CP-even Higgs exchange, and s-channel

[8] For a historical account of this terminology see [76].

squark exchange are contained in

$$f_{p/n} = \sum_{q=u,d,s} f_{T_q}^{(p/n)} a_q \frac{m_{p/n}}{m_q} + \frac{2}{27} f_{TG}^{(p/n)} \sum_{q=c,b,t} a_q \frac{m_{p/n}}{m_q} \ . \tag{2.29}$$

Here $f_{TG}^{(p/n)}$ is given by $1 - f_{T_u}^{(p/n)} - f_{T_d}^{(p/n)} - f_{T_s}^{(p/n)}$ and arises via gluon exchange with the nucleon and the $f_{T_q}^{(p/n)}$ are determined from light quark masses obtained from baryon masses via matrix elements and from the value of the pion-nucleon sigma-term. Numerical values and further details are given in, for example, the second Ref. of [38] and [78]. Entering importantly to the discussion is the LSP neutralino decomposition in terms of its Bino, Wino and Higgsino eigen components (In terms of the previous notation $(\tilde{B}, \tilde{W}^3) \equiv (\tilde{\lambda}_Y, \tilde{\lambda}^3)$)

$$\chi \equiv \chi_1^0 \ = \ n_{11}\tilde{B} + n_{12}\tilde{W}^3 + n_{13}\tilde{H}_1 + n_{14}\tilde{H}_2 \ . \tag{2.30}$$

The relevant couplings that enter in the spin independent cross section are [77][78]

$$\begin{aligned} a_q \equiv a_{3i} \ = \ & -\frac{1}{2(m_{1i}^2 - m_\chi^2)} \Re\left[(X_i)\,(Y_i)^*\right] - \frac{1}{2(m_{2i}^2 - m_\chi^2)} \Re\left[(W_i)\,(V_i)^*\right] \\ & -\frac{g_2 m_q}{4 m_W B}\left[\Re\left(\delta_1[g_2 n_{12} - g_Y n_{11}]\right) DC \left(-\frac{1}{m_H^2} + \frac{1}{m_h^2}\right)\right. \\ & \left. +\Re\left(\delta_2[g_2 n_{12} - g_Y n_{11}]\right)\left(\frac{D^2}{m_h^2} + \frac{C^2}{m_H^2}\right)\right] \ . \end{aligned} \tag{2.31}$$

The first term arises from squark exchange and is typically much suppressed over most of the signature space consistent with WMAP constraints, (it is given in full in [77][78]) however the largest contribution from squark exchange is typically seen for the case of a pure Bino LSP which can arise when the stop is the NLSP in SUGRA models [45]. The parameters $\delta_{1,2}$ depend on eigen components of the LSP wave function and B, C, D depend on VEVs of the Higgs fields and the Higgs mixing

parameter α and are given by

$$\text{for u quarks}: \quad \delta_1 = n_{13} \quad \delta_2 = n_{14} \quad B = \sin\beta \quad C = \sin\alpha \quad D = \cos\alpha \tag{2.32}$$

$$\text{for d quarks}: \quad \delta_1 = n_{14} \quad \delta_2 = -n_{13} \quad B = \cos\beta \quad C = \cos\alpha \quad D = -\sin\alpha \ . \tag{2.33}$$

2.3.5 Sparticle Production at Hadron Colliders

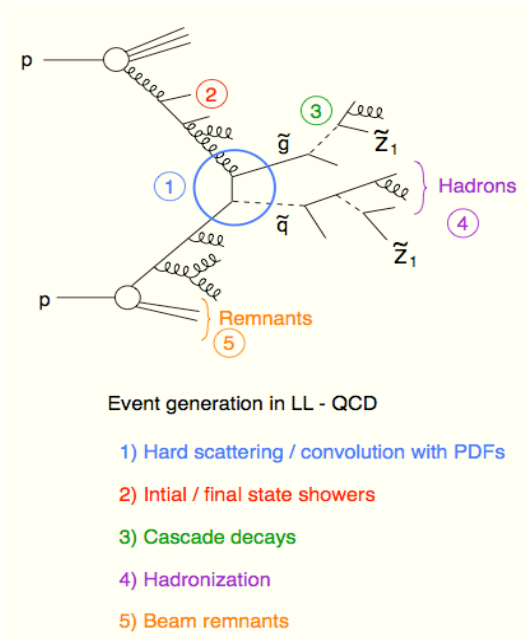

Figure 2.1: Sparticle Production at Hadron Colliders, figure by H. Baer and X. Tata, SUSY 07, Karlsruhe.

Simulating sparticle production at hadron colliders is a multi-step process. It involves (a) the hard scattering of initial state quarks and gluons of the partonic sub-processes, followed by (b) parton showering for colored particles, (c) the implementation of Monte Carlo techniques to describe the probability of a produced particle to decay into a daughter particle over sometimes very long decay chains, (d) the hadronization of the produced elementary colored particles from the decay chains

leading to a large collections of mesons and baryons, which can also decay further. (e) Finally, one needs to take care of remnants that were not involved in the hard scattering process. After all of these steps are accomplished one needs to sort out the number and type of events produced by the production of (s)particles and do so over a large class of final state state channels by collecting angular and four momentum information per particle per event. Specific programs have been created to accomplish these steps, and some details regarding these steps can be found in [79] and in [80] and [36].

Sparticle production involves a plethora of production modes. Many of the most relevant modes are reviewed in [36]. At the LHC the dominant production modes arise from the creation of gluino pair production ($\widetilde{g},\widetilde{g}$), mixed gluino ($\widetilde{g}$) squark ($\tilde{q}$) production, squark pair production, and chargino $\tilde{\chi}^{\pm}_{1,2}$ neutralino $\tilde{\chi}^{0}_{1-4}$ production. Perhaps the most interesting class of final states from the production of sparticles at hadron colliders involve mutli-lepton final states, tagged b-jets and missing energy/momentum. Here I will briefly discuss some of these relevant production modes.

Missing Energy/Momentum: Technically, the missing transverse energy is the negative vector sum of the transverse energy deposited in the EM and hadronic calorimeters. The modulus of this quantity is often referred to as missing $E_T^{\rm miss}$, $P_T^{\rm miss}$ or MET. In general, this should include transverse momenta of any muons. Since in practice, each calorimeter cell is labeled by a four vector with zero mass, and we are speaking of directed energy, the appropriate terminology becomes $P_T^{\rm miss}$. Early on, as mentioned already, it was realized that the stability of the LSP could lead to large amounts of $P_T^{\rm miss}$[6]. Due to the stability of a neutral LSP, every SUSY event leads to a large amount of $P_T^{\rm miss}$, though this largeness can vary based on the sparticle mass hierarchy responsible for the production of the missing P_T [58] as we soon will discuss in detail.

Tri-leptons: It was noted shortly after the discovery of SUGRA models that $W^{\pm}$ decay into a chargino and the second lightest neutralino can lead to a clean tri-leptonic signal [81] and further work was carried out in Ref.[82]. In Ref.[83] it was observed that the decays from an off-shell W can extend very significantly the potential for the discovery of the $3l$ mode. Many important works followed (for a sample of early papers see [84]). Thus the classic examples of tri-lepton production proceeds through the following sub-process: $q\bar{q}' \to W^* \to \tilde{\chi}_1^{\pm}\tilde{\chi}_2^0$ (production of $\tilde{\chi}_1^{\pm}\tilde{\chi}_2^0$ can also arise from intermediate squark exchange) followed by chargino decay through an off shell W via $\tilde{\chi}_1^{\pm} \to W^*\widetilde{\chi}_1^0 \to l\nu_l\widetilde{\chi}_1^0$, and neutralino decay $\tilde{\chi}_2^0 \to Z^*\widetilde{\chi}_1^0 \to l^{\pm}l^{\mp}\widetilde{\chi}_1^0$ or chargino/neutralino decays via off shell sleptons $\chi_1^{\pm} \to \tilde{l}^*\nu_l \to l\widetilde{\chi}_1^0\nu_l$, with $\chi_2^0 \to \tilde{l}^*l^{\mp} \to l^{\mp}l^{\pm}\widetilde{\chi}_1^0$. However, a copious number of tri-leptons may also be produced due to production of staus. It was pointed in the 3rd Ref. of [84] that if the following sparticle mass hierarchy is achieved $\widetilde{\chi}_1^0 < \widetilde{\tau}_1 < \widetilde{l}_R < \widetilde{\chi}_1^{\pm} \sim \widetilde{\chi}_2^0$ then the branchings $\widetilde{\chi}_2^0 \to \widetilde{l}_R l$, $\widetilde{\chi}_2^0 \to \widetilde{\tau}_1\tau$, and $\widetilde{\chi}_2^{\pm} \to \widetilde{\tau}_1\nu_\tau$, can all be enhanced. In the latter cases one may then have $\widetilde{\tau}_1 \to \widetilde{\chi}_1^0\tau$ followed by leptonic decaying of the taus $\tau \to \nu_\tau\nu_l l$, where $l = (e, \mu)$. In fact if the stau is much lighter than the chargino, the latter 2 branching fractions $\widetilde{\chi}_2^0 \to \widetilde{\tau}_1\tau$, and $\widetilde{\chi}_2^{\pm} \to \widetilde{\tau}_1\nu_\tau$ can proceed with essentially 100 % probability and enhance the $3l$ signal. Additional sources of tri-leptons are from light sleptons and sneutrinos, contributions from the production of 2 of the heavier neutralinos and charginos, and from SQCD sparticles (squark or gluino) being produced with EW-inos, however these modes are often sub-dominant.

Third Generation: The importance of b-tagging has been discussed in [85][87]. In certain regions of the parameter space it is found that there is an enhancement of the gluino decays to third generation quarks . This is most importantly the case when the LSP has a large Higgsino component, which occurs on the HB as we will show explicitly in the next chapter. Thus it is found that here the gluino decays to a quark

and an off shell squark the latter leading to an ino ($\tilde{\chi}^{\pm}_{1,2}, \tilde{\chi}^{0}_{i=1,4}$) and quark producing $\widetilde{g} \to (\tilde{\chi}^{-}_{1,2} + t\bar{b}) + h.c.$ and $\widetilde{g} \to \tilde{\chi}^{0}_{i=1,4} + t\bar{t}/b\bar{b}$. The opening up of the three body decays leads to a large number of heavy flavor final states which are detectable above the SM background.

It has also been pointed out that hadronically decaying *tau* jets, can lead to a substantial number of events above the backgrounds at the Tevatron and the LHC [86, 52, 57, 56, 45, 58, 60, 87]. For example through left handed squark decay, it becomes possible to get a large branching into $\widetilde{\chi}^{0}_{2}$ which as discussed already leads to a τ jet + LSP. As will be discussed shortly, the right handed squark may lead to a sizeable branching fraction into the LSP + quark yielding large amounts of $P_T^{\rm miss}$.

Detailed Reviews: Here we have a given a very brief summary of some of the features of SUGRA. More detailed reviews can be found in a number of works some of which we list below: Thus for a pedagogical discussion of SUSY see[47]; for a clear step by step constructions of the MSSM see the appendices of [22], and [67] and [36]. For reviews of the technical construction of applied $N = 1$ supergravity see [34],[6], and for the nice summaries of the end point of these constructions see [21],[67],[36]. For a review of radiative corrections to the Higgs masses see [67]; for reviews of SUGRA phenomenology see [88] and [66], [67],[36], and for an exceptionally clear overview see [89].

Chapter 3

Towards Decoding the Mechanism for the Origin of Dark Matter

It is shown that LHC signals of supersymmetric models carry sufficient information to allow one to decode the mechanism by which dark matter is generated in the early universe within a class of supersymmetric theories based on supergravity grand unification. The ability to decipher the mechanism for the production of dark matter in the early universe is further facilitated by correlating supersymmetric signals in experimentally relevant channels at the LHC with the cross sections from the scattering of neutralinos off nuclei.

3.1 Prelude

In the very near future, data from the LHC will be available allowing one to test models of physics beyond the Standard Model. As emphasized already, supersymmetry, and more specifically supergravity grand unified models, are of great interest due to their predictive nature and their ability to resolve several issues encountered

in low scale globally supersymmetric theories. Further, the nature of dark matter[90] and dark energy continues to be one of the primary open questions in both particle theory and cosmology. It is now widely believed that dark matter must be constituted of particles outside the standard list of known particles. Chief among these are the so called weakly interacting massive particles (WIMPS). Supersymmetry with R-parity conservation leads naturally to such a particle in the form of the lightest supersymmetric particle (LSP). In the framework of SUGRA unified models the lightest neutralino is a particularly attractive possibility.

Quite generally, an analysis of the relic density of the LSP reveals three broad regions where the the Wilkinson Microwave Anisotropy Probe (WMAP) [91] constraint on the density of dark matter $0.0855 < \Omega_{\widetilde{\chi}_1^0} h^2 < 0.1189$ (2σ) is satisfied. These include (a) the Hyperbolic Branch (HB)[71, 92] where multi TeV scalars can appear consistent with small fine tuning (sometimes referred to as the Focus Point region (FP) or as HB/FP), (b) the co-annihilation regions[73], (c) the Higgs pole region[93]. Of these, the stau co-annihilation region and the HB region are more generic while the pole region (light Higgs and the CP odd Higgs A) is more fine tuned. (d) In addition there is also the parameter space in the bulk region where the constraint from WMAP on the relic abundance of dark matter is satisfied, and this is due to a combination of effects.

Now, an interesting issue relates to the following: to what extent can the LHC data allow one to decode the mechanism by which dark matter is generated in the early universe? Specifically we will focus on dark matter originating in the Stau co-annihilation (Stau-Co) region or in the HB region to begin to answer this question.

Details regarding experimental constraints imposed in the analysis and a description of the analysis routine may be found in the Appendix(4.8). Here we briefly summarize as we wish to get to the main point. For concreteness in this chapter we

we work within the framework of the mSUGRA model. In the analysis, the sparticle masses and mixings are derived from the GUT scale with the SuSpect code [94] coupled to micrOMEGAs [95]. We merge the models via the SUSY Les Houches Accord format [96] into PYTHIA [79] for the computation of SUSY production at the LHC, in concert with PGS4 [97], to simulate LHC detector effects, and obtain the final event record. The models are constrained by their ability to properly break electroweak symmetry, by sparticle mass limits from LEP and Tevatron analyses, flavor constraints including $b \to s\gamma$ and $B_s \to \mu^+\mu^-$, by the supersymmetric contribution to the muon anomalous magnetic moment, and the double sided bound on the relic density. Our post trigger level cuts are as given in [60] and designed to emphasize the SUSY signatures of new physics over the SM background for a broad class of models.

Here it is necessary to briefly describe the Stau co-annihilation and the HB further. The Stau-Co arises on the branch of REWSB where the mass splitting between the LSP neutralino and the NLSP stau is relatively small. It is found that 77% percent of the model points in the Stau-Co from our Monte Carlo scan over the parameter space obey $\Delta M = M_{\rm NLSP} - M_{\rm LSP} = M_{\tilde{\tau}_1} - M_{\tilde{\chi}_1^0} \leq 10$ GeVwith 18 % of the model points having this mass splitting of $10 < \Delta M/{\rm GeV} < 40$ with the remaining 5% satisfying $\Delta M/{\rm GeV} \lesssim 100$. The possibility of rather light $\tilde{\tau}$ masses arise with more than 80 % of the model points in our scan having $M_{\tilde{\tau}_1} < 400$ GeV, with a rather even distribution of model points with $M_{\tilde{\tau}_1}$ in the mass ranges of $(100-200), (200-300), (300-400)$ GeV. However, here the discovery of light Higgses becomes challenging as the heavy SUSY Higgses are typically larger than $M_{A/H/H^\pm} > 300$ GeV. On the Stau-Co, the Bino Branch of radiative electroweak symmetry breaking, prominent processes entering in the relic density annihilation cross sections include: $\tilde{\tau}_1\widetilde{\chi}_1^0 \to (\tau Z), (\tau h), (\tau\gamma)$, $\tilde{\tau}_1\tilde{\bar{\tau}}_1 \to (f_i\bar{f}_i), (WW), (ZZ), (\gamma Z), (\gamma\gamma)$, and $\tilde{\tau}_1\tilde{\ell}_i (i \neq \tau) \to \tau\ell_i$.

On the the dense part of the HB there is a controlled set of annihilations giv-

ing rise to the satisfaction of the relic density and this is dominated by $\widetilde{\chi}_1^0\widetilde{\chi}_1^0 \to (WW), (ZZ), (t\bar{t}), (b\bar{b})$, over most of the parameter space, with a strongly Higgsino like LSP. Additionally there are a significant number of cases where the annihilation is dominated by the processes $\widetilde{\chi}_1^0\widetilde{\chi}_1^0 \to b\bar{b}$ [$\sim (85-90)\%$] and $\widetilde{\chi}_1^0\widetilde{\chi}_1^0 \to \tau^+\tau^-$ [$\sim (5-10)\%$], and these cases typically occur for larger neutralino masses which are more Bino like, but can also occur for low values of the neutralino masses as well on the HB. In terms of dominant final states for the Higgsino like LSP, it is found that the thermal annihilation cross sections would have arisen mostly from $\widetilde{\chi}_1^0\widetilde{\chi}_1^0$ annihilations into $WW(84\%)_{\rm Max}$ and $ZZ(24\%)_{\rm Max}$ as well as $t\bar{t}(77\%)_{\rm Max}$. Most often these channels conspired to produce the correct relic abundance, with sub-leading contributions from other channels.

Now, we discuss our findings from a study of SUSY signatures that reveals several correlated signals allowing a clear discrimination between the Bino and the Higgsino branches which may be responsible for dark matter annihilations in the early universe.

3.2 Decoding the Mechanism For Dark Matter Production with the LHC

3.2.1 The Chargino Wall and Chargino Ball

$N_{\rm SUSY}(leptons/jets)$ and $\langle P_T^{miss}\rangle$ vs $\sigma^{\rm SI}_{\widetilde{\chi}_1^0 p}$;

The LSP gaugino-Higgsino content enters importantly in the thermal annihilation cross sections that determine the proper relic density of decoupled neutralinos from the epoch of freeze-out. It also enters prominently in the strength of the scalar neutralino-proton cross section which we now discuss.

Significant information regarding the co-annihilation region and the HB region can

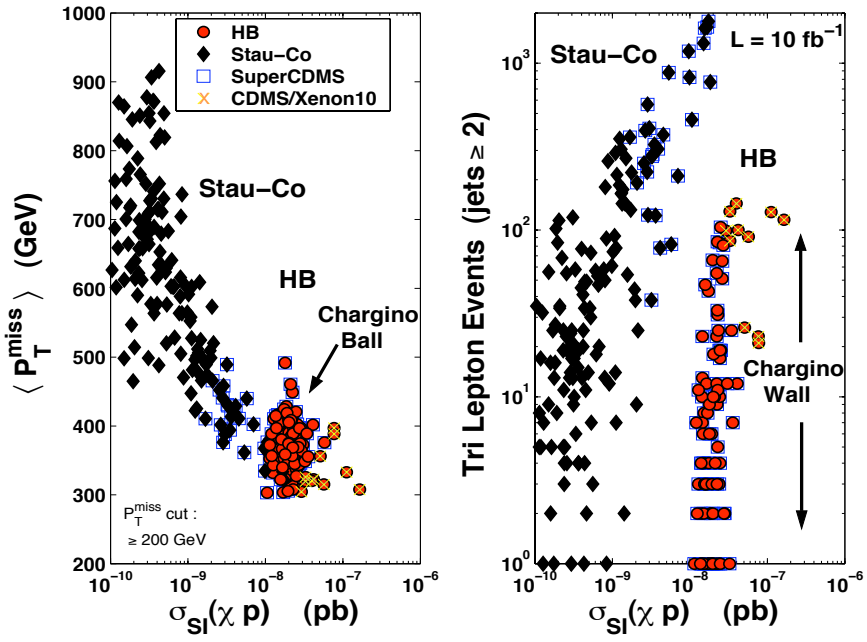

Figure 3.1: Right panel: An exhibition of the tri-leptonic signal vs $\sigma^{\rm SI}_{\widetilde{\chi}^0_1 p}$. Points in the vertical region to the right constitute the Chargino Wall. Left panel: an exhibition of $\langle P_T^{miss} \rangle$ vs $\sigma^{\rm SI}_{\widetilde{\chi}^0_1 p}$. The cluster of points at the end to the right constitute the Chargino Ball. The CDMS/Xe10 constraints[98] and constraints expected from SuperCDMS[99] are also shown. A clear discrimination of Stau-Co and HB can be seen in these plots. (From [87]).

be obtained by an analysis of the number of SUSY events at the LHC vs the spin-independent neutralino-proton cross section $\sigma^{\rm SI}_{\widetilde{\chi}^0_1 p}$ along with the current limits on the direct detection of dark matter. We give an illustration of the above in Fig.(3.1). The analysis of Fig.(3.1) (right panel) shows that the co-annihilation and the HB regions are well separated in the space spanned by the tri-leptonic signature 3L (L=e,μ) and $\sigma^{\rm SI}_{\widetilde{\chi}^0_1 p}$. One also finds the presence of a Chargino Wall (CW)[45, 87]. It refers to the region of HB where the NLSP is the lightest chargino, the LSP is mostly Higgsino like, and the spin independent cross section is essentially constant $O(10^{-8})$ pb as function of the neutralino mass for neutralino mass in the range $\sim$(80-650) GeV. In fact a flat region in the spin independent neutralino nucleon cross section was first seen in Ref. [92] and then following this in Ref. [100]. That the sparticle mass content or

hierarchies throughout the flat region remain uniform was first seen in [45], where it was further found that the flatness, or the Wall, is generic to SUGRA models studies with non-universalities which enters importantly in the analysis of LHC signatures. Flatness has been in observed in other recent works as well (see ex: [101]).

Further one observes that in Fig.(3.1) (left panel) the parameter points in the HB region in the $\langle P_T^{miss}\rangle - \sigma^{\rm SI}_{\widetilde{\chi}^0_1 p}$ plot are clustered together in a ball shaped region (the Chargino Ball (CB)[87]) and are well separated from points in the Stau-Co region which lie on a slope providing a strong discrimination between the Stau-Co and the HB regions. Therefore the HB lies in exceptionally predictive region, with a tight corridor on the amount of missing P_T^{miss} that it can produce (under the cuts imposed, but this remains generic under other cuts that reduce the SM background). However the Stau-Co can generally produce much larger amounts of P_T^{miss}, making it somewhat easier to discover in some cases. We will come back to this issue shortly.

It is however useful to see why the CW exists in the first place. Thus to explain the CW we observe that: (a) On the CW one typically has $m_H^2 \gg m_h^2$, and the heavier of the CP Higgs mass has a lower limit near 300 GeV and more typically it extends into the range of a TeV to several TeV, (b) $\sin\alpha \approx \alpha$ where α is the Higgs mixing parameter which enters in the diagonalization of the CP even Higgs mass^2 matrix, and $\alpha \times \tan\beta \simeq -1$, (c) further, the sfermion poles can be neglected as they make a small contribution in this region. In the absence of CP phases we obtain

$$\sigma^{\rm SI}_{\widetilde{\chi}^0_1 p}({\rm WALL}) \sim C_{\rm SM}(g_Y n_{11} - g_2 n_{12})^2 (n_{14} + \alpha n_{13})^2 (9f^p + 2f^p_{TG})^2 \tag{3.1}$$

where the SM content is

$$C_{\rm SM} = \frac{m_p^2 \mu^2_{\chi p} g_2^2}{324\pi m_h^4 M_W^2} \tag{3.2}$$

and $f^p = \sum_{q=u,d,s} f^{(p)}_{T_q}$ and $f^p_{TG} = 1 - f^p$ (see Ch.(2.3.4)). The typical ranges for n_{1i}

on the wall are: $n_{11} \in (.85, .99)$, $n_{12} \ll n_{11}$, and $n_{13} \in (.1, .6) \sim -\mathcal{O}(n_{14})$. Using numerical values one gets $\sigma^{\rm SI}_{\widetilde{\chi}^0_1 p}({\rm WALL}) \sim 2 \times 10^{-8}$ [pb]. In our analysis however, we have implemented the full cross section calculation without any of the above approximations. This analysis leads to $\sigma^{\rm SI}_{\widetilde{\chi}^0_1 p}$ (WALL) lying in the range $\sim (1.5 - 5) \times 10^{-8}$ pb while the most recent limits give $\sigma^{\rm SI}_{\widetilde{\chi}^0_1 p} \sim 5 \times 10^{-8}$ pb [98] for $m_\chi \approx 60$ GeV. Thus this region of the parameter space is within reach of the current and the next generation of dark matter experiments. As noted already, the CW is also a very interesting region for LHC signatures.

The analysis of Fig.(3.1) is really quite unique, and very important. For the first time, one sees the mapping of the LHC signature space of prominent channels connected to the signature space of direct detection [87]. It shows us that the HB should either be discovered or ruled out by dark matter experiments, while the LHC should be able to probe a good chunk of the Wall in the tri-lepton channel. Further the sensitivity from direct detection experiments may be greater than that of the LHC for the case of the HB. For the case of the Stau-Co, however, direct detection becomes less sensitive than that of the LHC over a large region of the signature spaces. In the context of the spin independent cross sections, this result is closely tied to the Bino vs. Higgsino content of the LSP wave-function.

3.2.2 Geometry of $P_T^{\rm miss}$ Distributions:

A powerful signature for the discrimination of Stau-Co and HB is the total number of SUSY events $N_{\rm SUSY}$ as a function of the missing transverse momentum. An analysis of this signature is given in Fig.(3.2) (left panel) where one finds different geometries in these distributions. Here we emphasize that the significantly fatter $P_T^{\rm miss}$ distributions for points in the Stau-Co region contrast sharply with the $P_T^{\rm miss}$ distributions from points in the HB region which are much thinner[60] as exhibited for the case given in

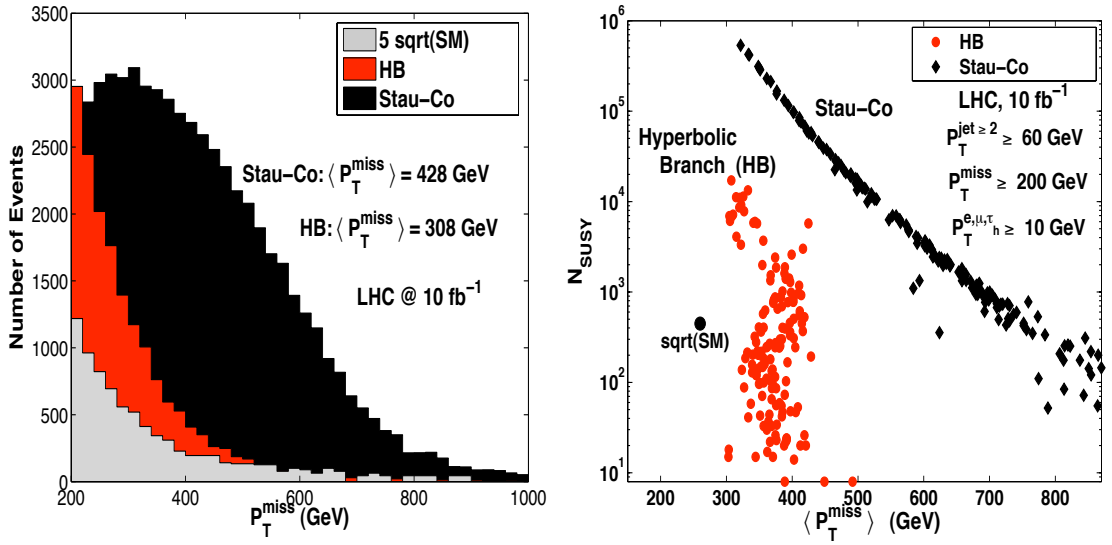

Figure 3.2: (Left): $N_{\rm SUSY}$ vs. $P_T^{\rm miss}$ for points in the Stau-Co and HB regions along with the SM background under the standard post-trigger level cuts. The Stau-Co and HB model points given here have $(m_0, m_{1/2}, A_0, \tan\beta, sign(\mu))$ as $(71.5, 348, 334, 10, +)$ and $(1694, 216, -740, 50, +)$ respectively (all masses are in GeV). The top mass is taken to be 170.9 GeV. (Right): $N_{\rm SUSY}$ vs. $\langle P_T^{\rm miss}\rangle$ for each parameter point in the Stau-Co and HB. $\langle P_T^{\rm miss}\rangle$ acts as an indicator of Stau-Co and HB regions. (From [87]).

Fig.(3.2)(left panel). Such a signature has the interesting feature in that the discovery potential is increased over a larger region in the SUGRA parameter space than for the case of counting fractional number of such events in separate channels. The above is due in part because every SUSY event that passes the trigger has $P_T^{\rm miss}$, and so one maximizes the signal events as opposed to obtaining a fraction of them. Further, the SM $P_T^{\rm miss}$ falls off rapidly beyond the peak value coupled with the fact the $P_T^{\rm miss}$ from SUSY events can be significantly larger, and can extend out to momenta where the SM cannot produce a large number of events.

3.2.3 $\langle P_T^{\rm miss}\rangle$ as a Discriminator

A remarkable signature emerges distinguishing the stau co-annihilation region and the HB region if one analyzes $N_{\rm SUSY}$ for each parameter point as a function of $\langle P_T^{\rm miss}\rangle$

which is the mean $P_T^{\rm miss}$ calculated by averaging the $P_T^{\rm miss}$ over the entire model event record. The above phenomenon is shown in Fig.(3.2) (right panel). Here one finds that $\langle P_T^{\rm miss}\rangle$ has a very wide range from 300 GeV to a TeV or more for the stau co-annihilation region, while $\langle P_T^{\rm miss}\rangle$ for the HB region lies in a much narrower band centered around 350 GeV - a phenomenon which originates for parameter points on the Chargino Wall. Thus the $\langle P_T^{\rm miss}\rangle$ ranges in Fig.(3.2) can be viewed as one of the smoking gun signatures which can discriminate between the two mechanisms using LHC data. This is in fact related to the presence of the Chargino Ball in Fig.(3.1).

Although a quantitative analysis of $\langle P_T^{\rm miss}\rangle$ is rather complicated since it involves many particles and depends in part on post trigger level cuts, one can give a qualitative picture of the disparity between the $P_T^{\rm miss}$ on the Stau-Co and the HB regions by analyzing the decay chains of sparticles into their final products culminating into an odd number of LSPs (per sparticle decay chain) and the SM particles. Here one finds that often the sparticle decays on the Stau-Co involve two body decays. For the HB case, however, one finds that the sparticles produced in pp collisions have typically a longer decay chain which depletes the $P_T^{\rm miss}$ in this case.

We illustrate these features by analyzing the two specific benchmarks given in the caption of Fig.(3.2)(left panel). For the HB model point of Fig.(3.2)(left panel) the following production cross sections are dominant: $pp \to (\widetilde{g}\widetilde{g}/\widetilde{\chi}_2^0\widetilde{\chi}_1^{\pm}/\widetilde{\chi}_1^{\pm}\widetilde{\chi}_1^{\mp})$ at the level of $(45, 25, 15)\%$. While squark production is highly suppressed ($m_{\widetilde{g}} \sim 622$ GeV $\ll m_{\widetilde{q}_L,\widetilde{q}_R,\widetilde{b}_1,\widetilde{t}_1} \in (1.2, 1.7)$ TeV). One finds that the dominantly produced $\tilde{g}$ decays via $\mathcal{BR}[\widetilde{g} \to \widetilde{\chi}_i^0 + q + \bar{q}] \sim 50\%$ and $\mathcal{BR}[\widetilde{g} \to \widetilde{\chi}_j^{\pm} + q + \bar{q}'] \sim 50\%$ with the LSP contributing only 10%. The reason for this largeness is because the on-shell decay of the gluino into $q\tilde{q}$ is suppressed due to largeness of the squark masses (a phenomenon which typically holds for the gluino decays on the HB). Further, the $\widetilde{\chi}_2^0$ and $\widetilde{\chi}_1^{\pm}$ produced on HB have $\mathcal{BR}[\widetilde{\chi}_2^0 \to \widetilde{\chi}_1^0 + f + \bar{f}] \sim 100\%$ and $\mathcal{BR}[\widetilde{\chi}_1^{\pm} \to \widetilde{\chi}_1^0 + f + \bar{f}'] \sim 100\%$.

Thus the decay chain for sparticles produced on the HB tend to be longer resulting in reduced P_T^{miss}. Now, for the Stau-Co model point of Fig.(3.2)(left panel) the leading SUSY production level cross sections are from $(\widetilde{g}\widetilde{q}, \widetilde{q}\widetilde{q}, \widetilde{g}\widetilde{g})$ at the level of $(41, 33, 7)\%$, with the corresponding 2 body decay modes $\mathcal{BR}[\widetilde{q}_R \to \widetilde{\chi}_1^0 + q] \sim 100\%$ (1st and 2nd generation), and $\mathcal{BR}[\widetilde{q}_L \to (\widetilde{\chi}_2^0, \widetilde{\chi}_1^\pm) + (q, q')] \sim (60, 30)\%$. Since the decay chain for sparticles on the Stau-Co tend to be shorter the resulting P_T^{miss} is larger. In summary the main reason why the HB tends to give lower values of missing P_T relative the Stau-Co is simply due to the fact that on the HB, in order to get to the LSP from the dominant gluino production mechanism one usually needs at least 2 successive 3 body decays, while on the Stau-Co the right-squarks ($\tilde{q}_R$) from the first and second generations, which are dominantly produced, each of which here, decays right into the LSP + quark. The above also holds more generally in that one finds that sparticles arising from the Stau-Co have much shorter decay chains resulting in fewer final particles and thus the missing energy can get large. Our more general results given here on a large spread in $P_T^{\rm miss}$ agree with the analysis given in[52] and with the analyses of the CMS and ATLAS collaborations [102, 103, 104]. Conversely the models on the HB have longer decay chains with more final state particles and thus the missing energy carried by the neutrals is depleted leading to missing $P_T^{\rm miss}$ which is more SM like. This feature has also been discussed in the CMS analysis of [105].

3.2.4 Cutting on Jets, n_{jet}^*:

Another powerful signature for discriminating the Stau-Co and the HB regions is $N_{\rm SUSY}$ taken as a function of $P_T^{*\rm miss}$and n_{jet}^*, i.e.,

$$N_{\rm SUSY} = N_{\rm SUSY}(n_{jet} \geqslant n_{jet}^*, P_T^{\rm miss} \geqslant P_T^{*\rm miss}), \tag{3.3}$$

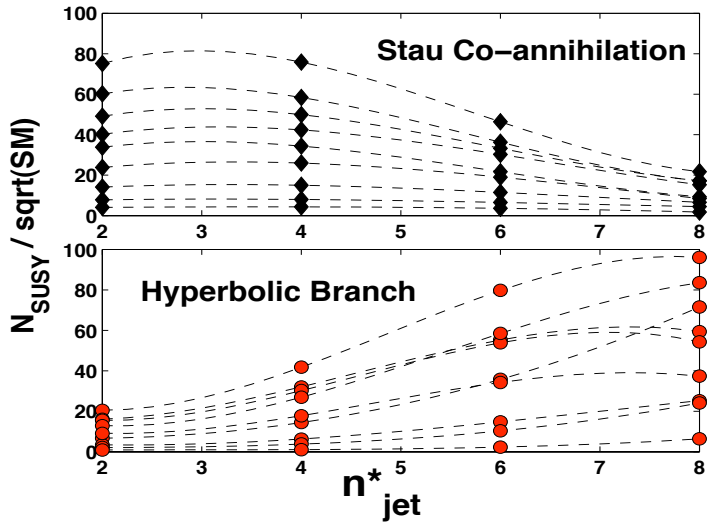

Figure 3.3: A discrimination of the two mechanisms for the satisfaction of the relic density, where the mechanism for the origin of dark matter is governed by stau co-annihilation and annihilation on HB with assumed LHC luminosity of 10 fb^{-1}. Curves (connecting $N_{\rm SUSY}/\sqrt{\rm SM}$ for discrete n^*_{jet}) correspond to various models with $M_{\rm LSP} < 275$ GeV for the Stau-Co and $M_{\rm LSP} <$ 230 GeV for the HB. The ratio of $N^{\rm HB/Stau-Co}_{\rm SUSY}/\sqrt{\rm SM}$ is computed under the standard post-trigger level cuts (see also Fig.(3.2)) but with n^*_{jet} taken as a variable. (From [87]).

where the $*$ indicates a fixed cut value. Here features specific to the co-annihilation branch and to the HB emerge when $P_T^{*\rm miss}$ is fixed, and n^*_{jet} is varied. This is shown in Fig.(3.3). In particular one finds that for the co-annihilation branch there is an optimal n^*_{jet} near 4 because the discovery limit criteria $N^{\rm Stau-Co}_{\rm SUSY}/\sqrt{\rm SM}$ decreases as a function of increasing n^*_{jet} and has a max near $n_{jet} \sim 4$, while for the HB, specifically on the Wall, the situation is quite different, in that the larger the n^*_{jet} the larger is the value of $N^{\rm HB}_{\rm SUSY}/\sqrt{\rm SM}$ (where of course the SM is subject to the same * cuts). Thus, as the jet number n^*_{jet} becomes large $N^{\rm HB}_{\rm SUSY}$ sustains a much stronger signal than $N^{\rm Stau-Co}_{\rm SUSY}$, and thus $N_{\rm SUSY}/\sqrt{\rm SM}$ is a strong discriminator between the Stau-Co and the HB regions.

The above becomes very significant if the SUSY scale is high with the LSP mass lying in the several hundred GeV range. Also, this type of large n-jet cut can deplete

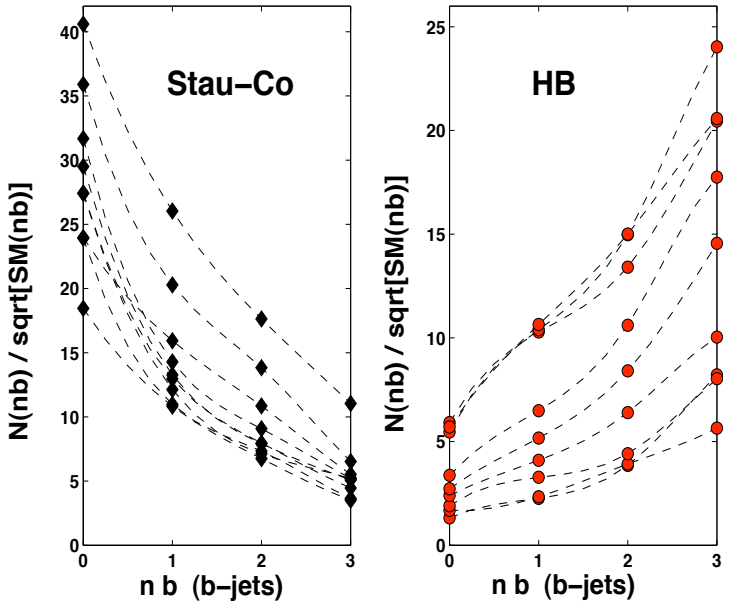

Figure 3.4: $N(nb)/\sqrt{\mathrm{SM}(nb)}$ vs nb for the Stau-Co and HB regions where $N(nb)$ (SM(nb)) is the number of SUSY (SM) events that contain n b-tagged jets. A sharp discrimination between the Stau-Co and the HB by b-tagging is observed. The number n^*_{jet} is fixed at 2. Here $m_{\tilde{g}} \leq 1.1$ TeV. (From [87]).

the leptonic signal, so a delicate balance of jet cuts is very important. In fact, if the SUSY signal is not highly leptonic, the analysis of the above type would be an efficient way to decipher new physics. Further, even if one has signatures with many leptons, the jet analysis will provide additional corroborating signatures for discovery and discrimination.

3.2.5 Importance of b-Tagging

The utility of b-tagging for the HB region has previously been emphasized in [85, 55, 60]. In Fig. (3.4) we give an analysis exhibiting how b-tagging provides a striking discrimination between the Stau-Co and HB regions where we plot $N(nb)/\sqrt{\mathrm{SM}(nb)}$ as a function of the number of tagged b-jets (nb) and find this dependence to be drastically different for Stau-Co vs HB regions. Here one observes that the discovery

limit becomes enhanced on the HB with increasing the number of tagged b-jets. Conversely, on the Stau-Co the discover limit fades with increasing the number of tagged b-jets. This is easily seen by following the lowest curve on each plot in Fig. (3.4). This is a rather significant result. It means quite simply, that while one class of models, originating from annihilations on the HB, will not be discoverable with a small number of b-tags, it will becomes discoverable by increasing the number of b-tags, while a Stau-Co model point which appears discoverable with a smaller number of tagged b-jets will fade out in its ability to be discovered as the number of tagged b-jets is increased. However, one may observe that the tagging of b-jets is really more crucial for the discovery of a model on the HB than for the Stau-Co, as the discovery limit never fall below ~ 5 sigma for the model points shown in the Stau-Co.

One can again see why this occurs. As already discussed, on the HB gluino production is dominant in pp collisions at the LHC. Continuing with the previous example, one further finds that the gluino decays dominantly into $b\bar{b}$, i.e., $\mathcal{BR}[\widetilde{g} \to \widetilde{\chi}_i^0 + b + \bar{b}] \sim 40\%$ and $\mathcal{BR}[\widetilde{g} \to \widetilde{\chi}_j^{\pm} + b(\bar{b}) + \bar{t}(t)] \sim 40\%$. Thus, the gluino 3 body decays are very rich in b quarks. Conversely for the Stau-Co model point of Fig.(1) (left panel) the pp production cross sections are as follows: $(\tilde{g}\tilde{q}) \sim 41\%$, $(\tilde{q}\tilde{q}) \sim 33\%$, $(\tilde{g}\tilde{g}) \sim 7\%$ (as already noted). Further, the gluino has only a small branching ratio into $b\bar{b}$ in this case via $\tilde{g} \to \tilde{b}b$. Including the production cross sections for $\tilde{g}\tilde{g}$ and the branching ratios, we find that overall the $b\bar{b}$ production on Stau-Co is smaller relative to that on the HB.

This is supported more generally in in Fig. (3.5) where the fractional number of events with 2b-jets vs the number of events with 2b-jets is given, and again one sees a strong discrimination between the parameter points in the Stau-Co region vs those in the HB region where a larger percentage of events that pass the cuts contain tagged b-jets for the case of the HB relative to those on the Stau-Co.

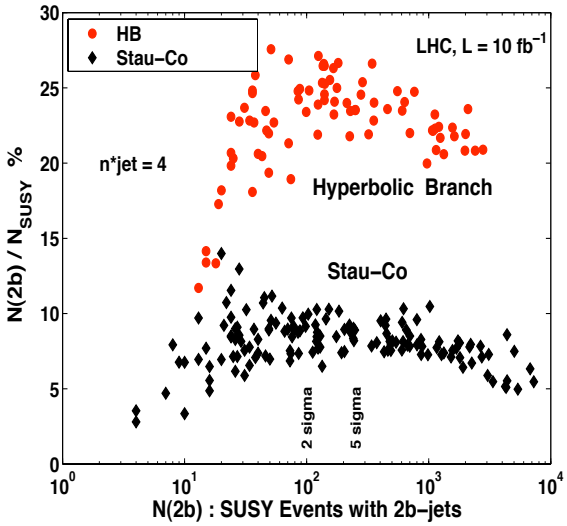

Figure 3.5: $N(2b)/N_{\rm SUSY}$ vs $N(2b)$ where n^*_{jet} is fixed at 4. Also shown are the 2σ and 5σ discovery reaches at 10/fb. Indeed the HB leads to a higher percentage of tagged b-jets. (From [87]).

In Fig.(3.6) we extend the analysis to the 4b-jet mode and correlate this signature to events with two hadronically decaying tau jets and to events that do not contain tagged b-jets. Here we find sharp discrimination. The boxed region forms the 1 sigma discovery limit boundary. Clearly any point falling in the box is not discoverable in these channels at the LHC with 10/fb of integrated luminosity under the cuts taken. We note however, that in these heavy flavor channels a very large set of model points become discoverable and indeed the classes of models are well separated in the LHC signature space. Fig.(3.6) shows quite clearly that the LHC event rates can distinguish between the HB and the Stau-Co, and that it is possible to pin down the model and the mechanism for the origin of dark matter in this framework, even at very low luminosities, i.e with only 10/fb of data. Of course, with higher luminosities we should be able to pull up some of the models that are suppressed in the event rates, and further one expects sharper discrimination with larger luminosities for models that are already discoverable and separated in these plots.

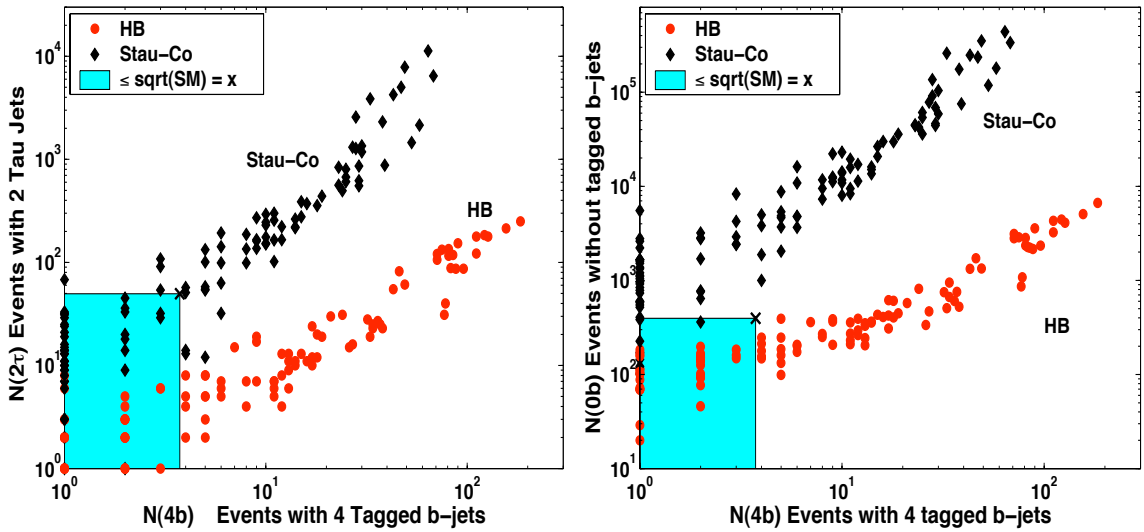

Figure 3.6: (Left panel) $N(2\tau)$ (the number of events with two hadronically decaying τ-jets) vs $N(4b)$ (the number of events with 4 tagged-b jets). A similar plot with $N(2\tau)$ replaced by $N(0b)$ (the number of events with no tagged b-jets) . (Right panel). The $\sqrt{\text{SM}}$ values in each channel are indicated by 'X' on the plots. Signatures arising from Stau-Co and from the HB regions are clearly discriminated.(From [87]).

More generally the analysis of Figs.[(3.2)-(3.6)] shows that the LHC signatures arising from the Stau-Co are easily distinguishable from those arising from the HB, while the analysis of Fig.(3.1) leads us to a more general method of pinning down the underlying model by correlating signals for the direct detection of neutralino dark matter with final state channels of missing P_T and leptonic signatures from sparticle production at the LHC. Indeed, such an analysis may point us to the mechanism for the production of dark matter in the early universe in this class of models.

In the above we have analyzed in detail how the LHC data can allow one to discover if the mechanism for the origin of dark matter in the early universe arises in the HB region or in the Stau-Co region. This opens up the issue if the above type analysis can be done more generally to identify the dominant mechanism for the generation of dark matter in the early universe using LHC data. Below we discuss briefly how one may extend the analysis to the stop co-annihilation region and the A-pole region. As

already discussed, in addition to the Stau-Co region there is also a stop co-annihilation (Stop-Co) region where the relic density constraint is satisfied. However, regions of the parameter space which give rise to Stop-Co have signatures which are highly non-leptonic relative to those of the Stau-Co and of the HB [58, 60]. Thus correlations such as 0L + jets vs 1L+ jets allow one to distinguish Stop-Co regions from others as discussed in the analysis of [58, 60]. Such correlations if observed, would be a good indication of stop co-annihilation as the origin of dark matter. We note in passing that the LSP is mostly all Bino in this case which suppresses the scalar cross sections in the direct detection of dark matter[45]. Next we discuss the A-funnel region. Here the relic density is satisfied because the LSP mass is nearly half the CP odd Higgs mass. The analysis of parameter points which cluster near the pole region do not have the same NLSP for all parameter points unlike the case of HB where $\tilde{\chi}_1^{\pm}$ is the NLSP, or the Stau-Co region where $\tilde{\tau}_1$ is the NLSP. However, in the pole region the NLSP could be $\tilde{\chi}_1^{\pm}$ or $\tilde{\tau}_1$ or even $H^{\pm}$ ($\tilde{t}_1$ is seldom seen in the pole region). Thus the A-pole region can give mixed signatures, sometimes characteristic of HB and sometimes characteristic of the Stau-Co. To firmly establish the pole region one would need a global analysis with many signatures which would give a determination of the Higgs A^0 mass and the mass of the LSP. A similar situation holds for other isolated regions of the parameter space which cannot be classified in the above categories which satisfy the relic density constraints. Here also one would need a global analysis on the signatures to identify the mechanism that gives rise to the origin of dark matter. Some of this issues are taken up in the next chapter.

3.3 Summary

The analysis presented here shows that with sufficient LHC data one can discriminate between the Stau-Co and the HB regions regarding the origin of dark matter in the early universe in the mSUGRA model using lepton, jet and missing energy signatures. We discussed several smoking gun signatures for such a discrimination. It was also shown that further discrimination is possible by combining LHC data with the limits on $\sigma^{\rm SI}_{\widetilde{\chi}^0_1 p}$ from the direct detection of dark matter. Within this framework, it is clear that a study of LHC signatures and dark matter signatures allow us to distinguish between the Higgisino vs. Bino dominated scenarios over a broad class models. While the analysis presented in our work illustrates our main points in the mSUGRA model, similar analyses along these lines should be pursued for other models of soft breaking including string and D-Brane models. Specifically, it would be interesting to analyze what the LHC can tell us about the origin of dark matter in cases where one has departures from the case of neutralino dark matter.

Chapter 4

Sparticle Landscape and Light Higgses in SUGRA/D-Brane Models

In the previous chapter it was emphasized that one can begin to decode the origin of dark matter in the early universe by examining correlated signatures of LHC signals with signals relevant to the direct detection of dark matter. It begs the question, is this possible more generally? One can indeed make progress in this direction by sorting out the landscape of sparticle mass hierarchies [58, 45, 60] and examining correlated signatures of new physics in multiple ways. A brief review of some of the details discussed here can be found in [106, 107].

4.1 Resolving the Sparticle Landscape

We begin with the concept of the Sparticle Landscape[58]. There are a total of 32 massive particles predicted in the MSSM. The number of ways in which the sparticle

masses can stack up in their mass hierarchy is a priori undetermined without the assumption of a model choice and imposition of phenomenological constraints. Thus, if 32 masses are treated as essentially all independent, then aside from sum rules on the Higgs, sfermions, chargino and neutralino masses, and without imposition of any constraints, the number of hierarchical patterns for the sparticles could be as many as $O(10^{25-28})$ or larger. One may compare this with the landscape of string vacua in type II-B strings which lead to $O(10^{1000})$ possibilities.

Now, the number of possibilities can be reduced by very significant amounts in supergravity models with the imposition of the constraints of radiative electroweak symmetry breaking (REWSB), and other phenomenological constraints. In fact, the number of possibilities is drastically reduced in the minimal supergravity grand unified model although no classification had ever been made and the precise number of possibilities of the full landscape is still not known. A cartography of the landscape was first undertaken in [58]. Such a cartography is important for devising strategies for analyzing data from the LHC. In the analysis of [45] a larger set of sparticles mass patterns were uncovered by extending the minimal framework to include a larger landscapes in mSUGRA, in SUGRA models with non-universalities (NUSUGRA), and in D-Brane models.

The focus here is on the sparticle mass patterns for the four lightest particles (discounting the lightest Higgs) as they would to a great degree influence the discovery of SUSY while keeping the size of the landscape in check. We have carried out a mapping of the mSUGRA parameter space and for the first four particles we find 22 mass patterns with all constraints as discussed in the Appendix(4.8). We label these as mSUGRA pattern 1 (mSP1) through mSUGRA pattern 22 (mSP22), the first 16 arising for $\mu > 0$ [58].

In Table(4.1) we exhibit these mass orderings. The groupings may be considered more simply in terms of the NLSP, thus there are Chargino Patterns (CPs), Stau Patterns (SUPs), Stop Patterns (SOPs), Higgs Patterns (HPs), and an isolated Neutralino (2) pattern.

mSP	Mass Pattern	μ
mSP1	$\widetilde{\chi}_1^0 < \widetilde{\chi}_1^\pm < \widetilde{\chi}_2^0 < \widetilde{\chi}_3^0$	$\mu_\pm$
mSP2	$\widetilde{\chi}_1^0 < \widetilde{\chi}_1^\pm < \widetilde{\chi}_2^0 < A/H$	$\mu_\pm$
mSP3	$\widetilde{\chi}_1^0 < \widetilde{\chi}_1^\pm < \widetilde{\chi}_2^0 < \widetilde{\tau}_1$	$\mu_\pm$
mSP4	$\widetilde{\chi}_1^0 < \widetilde{\chi}_1^\pm < \widetilde{\chi}_2^0 < \widetilde{g}$	$\mu_\pm$
mSP5	$\widetilde{\chi}_1^0 < \widetilde{\tau}_1 < \widetilde{l}_R < \widetilde{\nu}_\tau$	$\mu_\pm$
mSP6	$\widetilde{\chi}_1^0 < \widetilde{\tau}_1 < \widetilde{\chi}_1^\pm < \widetilde{\chi}_2^0$	$\mu_\pm$
mSP7	$\widetilde{\chi}_1^0 < \widetilde{\tau}_1 < \widetilde{l}_R < \widetilde{\chi}_1^\pm$	$\mu_\pm$
mSP8	$\widetilde{\chi}_1^0 < \widetilde{\tau}_1 < A \sim H$	$\mu_\pm$
mSP9	$\widetilde{\chi}_1^0 < \widetilde{\tau}_1 < \widetilde{l}_R < A/H$	$\mu_\pm$
mSP10	$\widetilde{\chi}_1^0 < \widetilde{\tau}_1 < \widetilde{t}_1 < \widetilde{l}_R$	μ_+
mSP11	$\widetilde{\chi}_1^0 < \widetilde{t}_1 < \widetilde{\chi}_1^\pm < \widetilde{\chi}_2^0$	$\mu_\pm$
mSP12	$\widetilde{\chi}_1^0 < \widetilde{t}_1 < \widetilde{\tau}_1 < \widetilde{\chi}_1^\pm$	$\mu_\pm$
mSP13	$\widetilde{\chi}_1^0 < \widetilde{t}_1 < \widetilde{\tau}_1 < \widetilde{l}_R$	$\mu_\pm$
mSP14	$\widetilde{\chi}_1^0 < A \sim H < H^\pm$	μ_+
mSP15	$\widetilde{\chi}_1^0 < A \sim H < \widetilde{\chi}_1^\pm$	μ_+
mSP16	$\widetilde{\chi}_1^0 < A \sim H < \widetilde{\tau}_1$	μ_+
mSP17	$\widetilde{\chi}_1^0 < \widetilde{\tau}_1 < \widetilde{\chi}_2^0 < \widetilde{\chi}_1^\pm$	μ_-
mSP18	$\widetilde{\chi}_1^0 < \widetilde{\tau}_1 < \widetilde{l}_R < \widetilde{t}_1$	μ_-
mSP19	$\widetilde{\chi}_1^0 < \widetilde{\tau}_1 < \widetilde{t}_1 < \widetilde{\chi}_1^\pm$	μ_-
mSP20	$\widetilde{\chi}_1^0 < \widetilde{t}_1 < \widetilde{\chi}_2^0 < \widetilde{\chi}_1^\pm$	μ_-
mSP21	$\widetilde{\chi}_1^0 < \widetilde{t}_1 < \widetilde{\tau}_1 < \widetilde{\chi}_2^0$	μ_-
mSP22	$\widetilde{\chi}_1^0 < \widetilde{\chi}_2^0 < \widetilde{\chi}_1^\pm < \widetilde{g}$	μ_-

Table 4.1: The Sparticle Landscape of Mass Hierarchies in mSUGRA. In patterns mSP14,15,16 the $\tilde{\chi}_1^0$ and the Higgs bosons (A, H) are sometimes seen to switch in their order.(From [58, 60].)

Since the nature of physics at the Planck scale is largely unknown it is useful to consider other soft breaking scenarios beyond mSUGRA. One such possibility is to consider non-universalities in the Kähler potential, (or non-diagonal gauge kinetic functions) which can give rise to non-universal soft breaking consistent with flavor

constraints. We consider three possibilities which are non-universalities in (i) the Higgs sector (NUH), (ii) the third generation squark sector (NUq3), and (iii) the gaugino sector (NUG) (for a sample of previous work on dark matter analyses with non-universalities see [38]). We parametrize these at the GUT scale as follows:

$$(i)\ \text{NUH} : M_{H_u} = m_0(1+\delta_{H_u}), \quad M_{H_d} = m_0(1+\delta_{H_d}), \tag{4.1}$$

$$(ii)\ \text{NUq3} : M_{q3} = m_0(1+\delta_{q3}), \quad M_{u3,d3} = m_0(1+\delta_{tbR}), \tag{4.2}$$

$$(iii)\ \text{NUG} : M_1 = m_{1/2}, \quad M_2 = m_{1/2}(1+\delta_{M_2}), \quad M_3 = m_{1/2}(1+\delta_{M_3}). \tag{4.3}$$

NUSP	Mass Pattern	Model
NUSP1	$\widetilde{\chi}_1^0 < \widetilde{\chi}_1^\pm < \widetilde{\chi}_2^0 < \widetilde{t}_1$	NU3,NUG
NUSP2	$\widetilde{\chi}_1^0 < \widetilde{\chi}_1^\pm < A \sim H$	NU3
NUSP3	$\widetilde{\chi}_1^0 < \widetilde{\chi}_1^\pm < \widetilde{\tau}_1 < \widetilde{\chi}_2^0$	NUG
NUSP4	$\widetilde{\chi}_1^0 < \widetilde{\chi}_1^\pm < \widetilde{\tau}_1 < \widetilde{l}_R$	NUG
NUSP5	$\widetilde{\chi}_1^0 < \widetilde{\tau}_1 < \widetilde{\nu}_\tau < \widetilde{\tau}_2$	NU3
NUSP6	$\widetilde{\chi}_1^0 < \widetilde{\tau}_1 < \widetilde{\nu}_\tau < \widetilde{\chi}_1^\pm$	NU3
NUSP7	$\widetilde{\chi}_1^0 < \widetilde{\tau}_1 < \widetilde{t}_1 < A/H$	NUG
NUSP8	$\widetilde{\chi}_1^0 < \widetilde{\tau}_1 < \widetilde{l}_R < \widetilde{\nu}_\mu$	NUG
NUSP9	$\widetilde{\chi}_1^0 < \widetilde{\tau}_1 < \widetilde{\chi}_1^\pm < \widetilde{l}_R$	NUG
NUSP10	$\widetilde{\chi}_1^0 < \widetilde{t}_1 < \widetilde{g} < \widetilde{\chi}_1^\pm$	NUG
NUSP11	$\widetilde{\chi}_1^0 < \widetilde{t}_1 < A \sim H$	NUG
NUSP12	$\widetilde{\chi}_1^0 < A \sim H < \widetilde{g}$	NUG
NUSP13	$\widetilde{\chi}_1^0 < \widetilde{g} < \widetilde{\chi}_1^\pm < \widetilde{\chi}_2^0$	NUG
NUSP14	$\widetilde{\chi}_1^0 < \widetilde{g} < \widetilde{t}_1 < \widetilde{\chi}_1^\pm$	NUG
NUSP15	$\widetilde{\chi}_1^0 < \widetilde{g} < A \sim H$	NUG
DBSP1	$\widetilde{\chi}_1^0 < \widetilde{\tau}_1 < \widetilde{\nu}_\tau < A/H$	DB
DBSP2	$\widetilde{\chi}_1^0 < \widetilde{\tau}_1 < \widetilde{\nu}_\tau < \widetilde{l}_R$	DB
DBSP3	$\widetilde{\chi}_1^0 < \widetilde{\tau}_1 < \widetilde{\nu}_\tau < \widetilde{\nu}_\mu$	DB
DBSP4	$\widetilde{\chi}_1^0 < \widetilde{t}_1 < \widetilde{\tau}_1 < \widetilde{\nu}_\tau$	DB
DBSP5	$\widetilde{\chi}_1^0 < \widetilde{\nu}_\tau < \widetilde{\tau}_1 < \widetilde{\nu}_\mu$	DB
DBSP6	$\widetilde{\chi}_1^0 < \widetilde{\nu}_\tau < \widetilde{\tau}_1 < \widetilde{\chi}_1^\pm$	DB

Table 4.2: The Sparticle Landscape in NUSUGRA and the D-Brane model considered. (From [58, 45, 60].)

For the case of non-universalities , we find 15 new mass patterns labeled NUSP(1-15). We also find in a phenomenological class of models based on D-Branes, 6 more new patterns labeled as DBSP(1-6). A complete sets of benchmarks for each pattern can be found in [58, 45, 60]. In Fig.(4.1) we show the sparticle landscape for the mSUGRA case for $\mu > 0$. We have carried out similar analyses for the NU and DB cases (see [45, 60]). Our analysis uncovers a much larger set of mass hierarchies than has previously been thought to exist; even in the minimal model. This is so because one usually is searching the parameter space with vanishing tri-linear coupling. Such an assumption is ad hoc, and needs to be dispensed with. Here we specifically observe several classes of sparticle mass patterns not discussed in the literature prior to this analysis. There are in fact Higgs Patterns which occur for large $\tan\beta$ in mSUGRA where the CP odd/heavier CP even Higgses are in fact the lightest particles beyond the LSP neutralino and in some cases they can be even lighter (we remind the reader that the Higgses are R-Parity even). These Higgs Patterns (HPs)[58] are labeled mSP(14-16). Along the large m_0 region with lower values of $m_{1/2}$ the mass hierarchy is

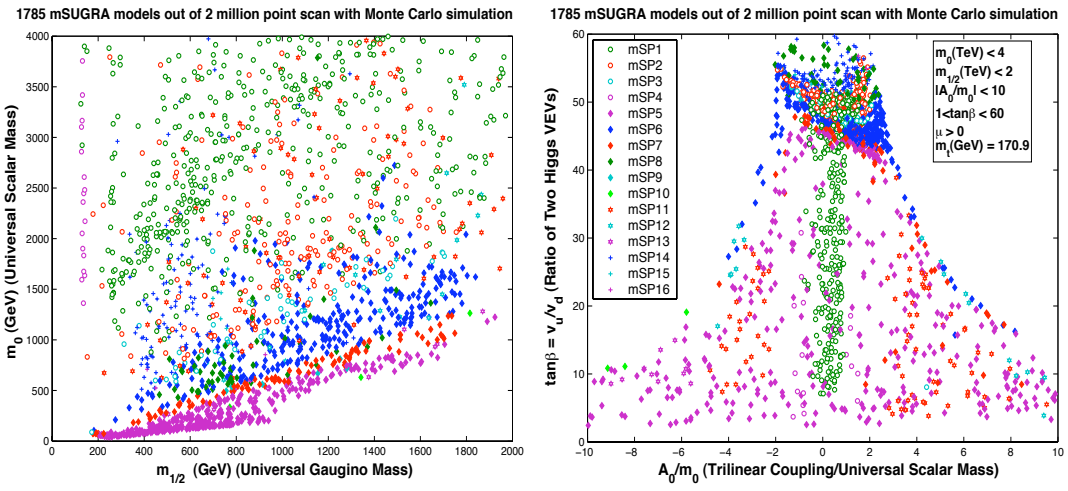

Figure 4.1: Parameter space in terms of the sparticle mass hierarchies for $\mu > 0$ under the 2 sided WMAP constraints, and REWSB constraints, and all other constraints discussed in the Appendix(4.8). (From [58].)

dominantly composed of mSP1 with annihilations on the HB, while there is also a Bino branch of mSP1 in which the the lightest chargino and next heavier neutralino are very close in mass, really effectively degenerate. One also observes several more chargino patterns (CPs) where the NLSP is a chargino (mSP1-mSP4), where mSP4 is rather special with a very light neutralino mass less than ~ 55 GeV. Further there are stau patterns (SUPS) mSP(5-10), and they are stop patterns (SOP) mSP(11-13). There are also patterns where the gluino is light and is the NLSP and where the sneutrino of the third generation is light and is the NLSP occurring in the NU and DB cases respectively as illustrated in Table(4.1). Earlier works which advocated benchmark points and slopes do not cover the more broad set of possible mass hierarchies we discuss here. That is, a large number of the mSP patterns do not appear in previous works. All of the Snowmass mSUGRA points (labeled SPS) [108] are only of types mSP(1,3,5,7) as follows:

$$\begin{aligned} &(\mathrm{SPS1a}, \mathrm{SPS1b}, \mathrm{SPS5}) \to \mathrm{mSP7} \qquad \mathrm{SPS2} \to \mathrm{mSP1} \\ &\mathrm{SPS3} \to \mathrm{mSP5} \qquad (\mathrm{SPS4}, \mathrm{SPS6}) \to \mathrm{mSP3}\ . \end{aligned} \tag{4.4}$$

Regarding the Post-WMAP points [109] one has the following mapping

$$\begin{aligned} &(\mathrm{A}', \mathrm{B}', \mathrm{C}', \mathrm{D}', \mathrm{G}', \mathrm{H}', \mathrm{J}', \mathrm{M}') \to \mathrm{mSP5}, \\ &(\mathrm{I}', \mathrm{L}') \to \mathrm{mSP7}, \mathrm{E}' \to \mathrm{mSP1}, \mathrm{K}' \to \mathrm{mSP6}\ . \end{aligned} \tag{4.5}$$

The CMS benchmarks classified as (Low/High) Mass (LM)/(HM) [110] do a better job of representing mSP1 which is the dominant pattern we find, and the mapping is

$$\mathrm{LM1}, \mathrm{LM6}, \mathrm{HM1} \to \mathrm{mSP5}\ , \tag{4.6}$$

$$\text{LM2, LM5, HM2} \rightarrow \text{mSP7} \ ,$$

$$\text{LM3, LM7, LM8, LM9, LM10, HM4} \rightarrow \text{mSP1} \ ,$$

$$\text{LM4, HM3} \rightarrow \text{mSP3} \ .$$

Note there are no Higgs patterns or stop patterns discussed in the CMS benchmarks as well as in SPS or in Post-WMAP benchmarks. Thus a very large class of models consistent with all known experimental constraints have not been studied in the current literature. However in the pursuit of SUSY at the LHC, inclusion of the missing patterns is essential as the sparticle mass hierarchies are intimately connected to to LHC signatures of new physics. The most transparent example of why this is so follows from the fact that the mass hierarchies dictate which sparticle decay chains are kinematically accessible.

4.2 The Direct Detection of Dark Matter as a Probe of the Landscape

We discuss now the direct detection of dark matter from the context of the sparticle landscape. In Fig.(4.2)(left panel) we give an analysis of the scalar neutralino-proton cross section $\sigma^{\rm SI}_{\widetilde{\chi}^0_1 p}$ as a function of the LSP mass in mSUGRA for $\mu > 0$. It is clear that the Higgs patterns give the largest dark matter cross sections over most of the signature space and are therefore the first ones to be constrained by experiment. The second largest cross sections arise from the Chargino Patterns which shows the Wall, with a copious number of points with cross sections in the range $\mathcal{O}(10^{-8})$ pb followed by Stau Patterns , with the Stop Patterns producing the smallest cross sections as they are nearly % 100 Bino like. The analysis of Fig.(4.2) shows more generally, as pointed out in the previous chapter, that the scalar cross sections lie in an interesting

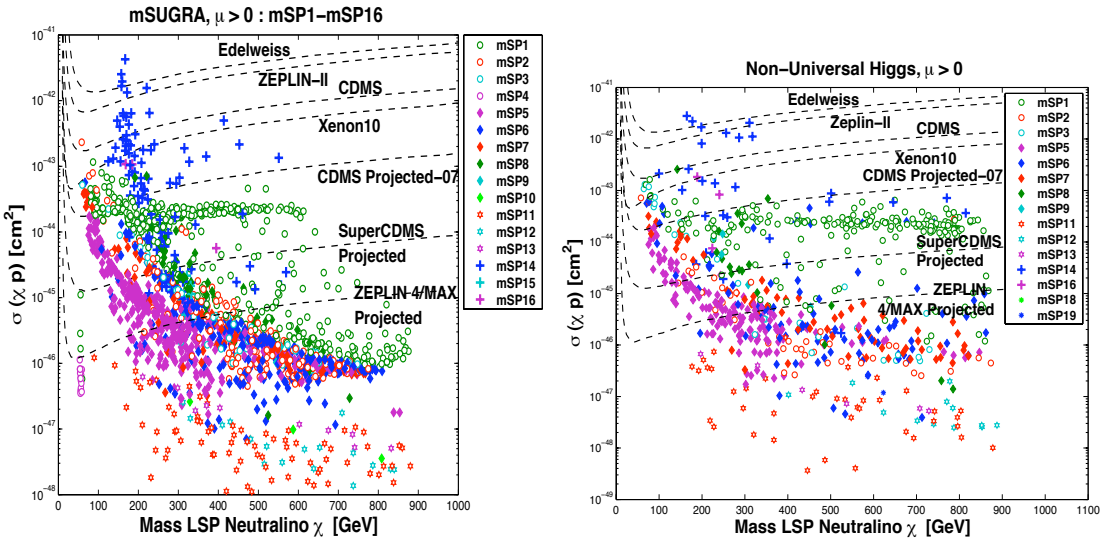

Figure 4.2: Analysis of the scalar cross section $\sigma^{\rm SI}_{\widetilde{\chi}^0_1 p}$ for MSUGRA and NUH. The sparticle mass hierarchies act as prism separating out the signatures space relevant for dark matter direct detection experiments. A Wall of nearly constant $\sigma^{\rm SI}_{\widetilde{\chi}^0_1 p}$ exists in both mSUGRA and in NUH. (From [45]).

region and are accessible to dark matter experiments currently underway and will be accessible to improved experiments in the future [111, 112, 113, 114, 115, 116]. Indeed the analysis of Fig.(4.2) shows that some of the parameter space of the Higgs Patterns is beginning to be constrained by the CDMS and the Xenon10 data [115].

We also can see that the signature space for direct detection of dark matter in NUSUGRA exhibits similarities to the mSUGRA case. The results of the analysis are presented in Fig.(4.2)(right panel) and Fig.(4.3). As in the mSUGRA case one finds that the largest dark matter cross sections still arise from the Higgs Patterns followed by the Chargino Patterns within the three types of non-universality models considered: NUH, NUq3 , and NUG. Again the analysis within NUSUGRA shows the phenomenon of the Chargino Wall, i.e., the existence of a copious number of Chargino Patterns (specifically mSP1) in all cases with cross sections in the range $\mathcal{O}(10^{-8})$ pb. Indeed as in the mSUGRA case, most of these parameter points along

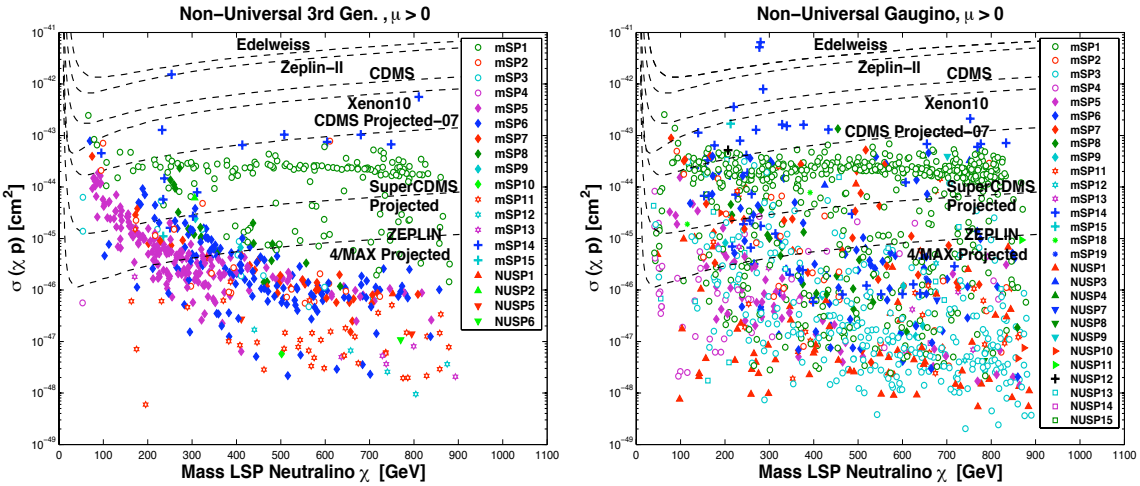

Figure 4.3: Analysis of the scalar cross section $\sigma^{\rm SI}_{\tilde{\chi}^0_1 p}$ for NUSUGRA for the cases NUq3 and NUG . The Wall consisting of a clustering of points in the Chargino Pattern mSP1 and persists up to an LSP mass of about 900 GeV with a $\sigma^{\rm SI}_{\tilde{\chi}^0_1 p}$ in the range $10^{-44\pm.5}$ cm^2 enhancing the prospects for the observation of dark matter by SuperCDMS and ZEPLIN-MAX in this region.(From [45]).

the Chargino Wall lie on the Hyperbolic Branch/Focus Point (HB/FP) region where the Higgsino components of the LSP are substantial. Thus this Chargino Wall again presents an encouraging region of the parameter space where the dark matter may become observable in improved experiments. Note that in the NU case, the Wall extends out further (as high as 900 GeV under our naturalness assumptions in the space explored).

4.3 Higgs Production and B physics

The lightness of A (and also of H and $H^{\pm}$) in the Higgs Patterns implies that the Higgs production cross sections at colliders can be enhanced, and especially this is so at large $\tan\beta$. The prospects for light SUSY Higgses have been discussed in [117, 118, 119, 120, 58, 121]. Our interest here is the 2τ mode which is a promising avenue for the discovery of the Higgs(es) at the Tevatron. Some benchmarks for the

HPs are given in Table(4.3). As mentioned already a complete set of benchmarks for all patterns arising in our analysis can be found in [60].

HPs	m_0 (GeV)	$m_{1/2}$ (GeV)	A_0 (GeV)	$\tan\beta$	NUH ($\delta_{H_u}, \delta_{H_d}$)	NUq3 ($\delta_{q3}, \delta_{tbR}$)	NUG ($\delta_{M_2}, \delta_{M_3}$)
mSP14	1036	562	500	53.5	(0,0)	(0,0)	(0,0)
mSP14	759	511	2315	31.0	(0.256,-0.499)	(0,0)	(0,0)
mSP14	1223	1200	-111	27.4	(0.557,-0.736)	(0,0)	(0,0)
mSP14	740	620	840	53.1	(0,0)	(-0.553,-0.249)	(0,0)
mSP14	1201	332	-731	55.0	(0,0)	(0,0)	(0.383,0.275)
mSP15	1113	758	1097	51.6	(0,0)	(0,0)	(0,0)
mSP15	900	519	1481	54.8	(0,0)	(0,0)	(-0.352,-0.262)
mSP15	1389	551	-167	59.2	(0,0)	(-0.041,0.916)	(0,0)
mSP16	525	450	641	56.0	(0,0)	(0,0)	(0,0)
mSP16	282	464	67	43.2	(0.912,-0.529)	(0,0)	(0,0)
NUSP12	2413	454	-2490	48.0	(0,0)	(0,0)	(-0.285,-0.848)

Table 4.3: Benchmarks for HPs for $\mu > 0$ in mSUGRA and in NUSUGRA. The 2nd and the 3rd mSP14 pattern show that the HPs can emerge for moderate values of $\tan\beta$. The Benchmarks are computed with SuSpect 2.34 . (From [45]).

The dominant modes entering our analysis arise from gluon fusion and bottom quark annihilation. (for detailed discussions on gluon fusion and bottom quark annihilation see [122, 123]). It is worth pointing out that the works of Ref. [118] have given rather robust formulas for SUSY Higgs production in the large $\tan\beta$ limit. At large $\tan\beta$ the partial decay width of the MSSM Higgses are dominantly governed by the square of the Yukawa couplings (the square being $\propto \tan^2\beta$ + a loop correction discussed below), and therefore neutral Higgs production into the heavy flavors are enhanced at large $\tan\beta$. Quite simply they find [118]

$$\sigma(gg, b\bar{b} \to A) \times [\mathcal{BR}(A \to 2\tau)] \simeq \sigma(gg, b\bar{b} \to h)_{SM} \frac{\tan^2\beta}{(1 + (\epsilon_0 + \epsilon_Y y_t^2)\tan\beta)^2 + 9}, \quad (4.7)$$

where the SM term denotes the values of the corresponding SM Higgs production cross sections at mass equal to M_A and where the ϵ corrections are loop corrections (see ex: [118]). This approximate formula hold up quite well when compared to some select cases using PYTHIA[79]. The above formula applies to the CP even Higgs H as well

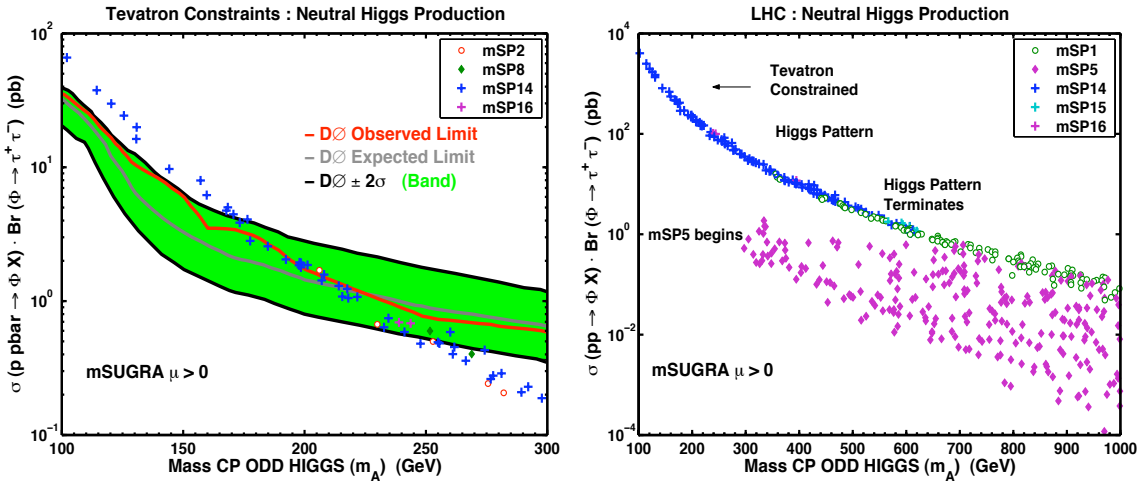

Figure 4.4: Left: Predictions for Higgs Production in the 2τ final state in mSUGRA as a function of the CP odd Higgs mass m_A for the HPs at the Tevatron. The limits from DØ are indicated [124]. Right: Predictions for in mSUGRA as a function of m_A at the LHC with CM energy of $\sqrt{s} = 14$ TeV for the HPs, the chargino pattern mSP1 and the stau pattern mSP5. The HPs are seen to give the largest cross sections. (From [45]).

leading to an enhancement of a factor of 2 of the production rates for $M_A \sim M_H > m_h$ in the large $\tan\beta$ regime. Quite interestingly the recent Tevatron data is beginning to constrain the HPs. This is exhibited in the left panel of Fig.(4.4) where the leading order cross section for the sum of neutral Higgs processes $\sigma_{\Phi\tau\tau}(p\bar{p}) = [\sigma(p\bar{p} \to \Phi)\mathcal{BR}(\Phi \to 2\tau)]$ vs the CP odd Higgs mass is plotted for CM energy of $\sqrt{s} = 1.96$ TeV at the Tevatron (the resolution criteria for addition of the cross sections we have taken is similar to the first Ref. of [119]). One finds that the predictions of $\sigma_{\Phi\tau\tau}(p\bar{p})$ from the HPs are the largest and lie in a narrow band followed by those from the Chargino Pattern mSP2. The recent data from the Tevatron is also shown[124] in Fig.(4.4). A comparison of the theory prediction with data shows that the HPs are being constrained by experiment. Exhibited in the right panel of Fig.(4.4) are predictions for the LHC. Here we find a termination of the HPs in mSUGRA at around 600 GeV in the CP odd Higgs mass under the naturalness assumptions in

our analysis (see Appendix(4.8)). Further, the Chargino pattern mSP1 also produces a large cross section, however the stau pattern mSP5 is found to have a suppressed branching fraction relative to the Higgisino like patterns over a significant region of the signature space.

$B_s \to \mu^+\mu^-$ and the Higgs Patterns: The process $B_s \to \mu^+\mu^-$ is dominated by the neutral Higgs exchange [125] and is enhanced by a leading factor of $\tan^6\beta$. It is thus reasonable to expect that the HPs will be constrained more severely than other patterns by the $B_s \to \mu^+\mu^-$ experiment, since most of the HP points usually arise from the high $\tan\beta$ region (we note, however, that the non-universalities in the Higgs sector (NUH) can also give rise to HPs for moderate values of $\tan\beta$). The analyses of [126] have given semi-analytical formulas for $\mathcal{B}r(B_s \to \mu^+\mu^-)$

$$\begin{aligned}\mathcal{B}r(B_s \to \mu^+\mu^-) &\simeq 3.5\times 10^{-5}\left[\frac{\tan\beta}{50}\right]^6\left[\frac{\tau_{B_s}}{1.5ps}\right]\left[\frac{F_{B_s}}{230\text{MeV}}\right]^2\left[\frac{|V_{ts}|}{0.040}\right]^2 \\ &\times\frac{m_t^4}{m_A^4}\frac{(16\pi^2)^2\epsilon_Y^2}{(1+(\epsilon_0+\epsilon_Y y_t^2)\tan\beta)^2(1+\epsilon_0\tan\beta)^2}. \qquad (4.8)\end{aligned}$$

In the above, enters the CKM mixing matrix element, τ_{B_s}, the mean lifetime, and F_{B_s} is the decay constant of the B_s meson. Here one can see explicitly the large $\tan\beta$ enhancements. Note, however in our analysis we use the code of [95] which actually follows the analysis of [127], however the results are generally in accord with Eq.(4.8).

That the HPs are being constrained at large $\tan\beta$ is supported by a detailed analysis which is given in Fig.(4.5) where the branching ratio $\mathcal{B}r(B_s \to \mu^+\mu^-)$ is plotted against the CP odd Higgs mass m_A. The upper left hand panel gives the analysis for the case of mSUGRA for $\mu > 0$ for the Higgs Patterns. One finds that the constraints are very effective for $\mu > 0$ (but not for $\mu < 0$) constraining a part of the parameter space of the HPs [45]. In Fig.(4.5). Again one finds that the $\mathcal{B}r(B_s \to \mu^+\mu^-)$ data constrains the parameter space of the HPs in the NUSUGRA

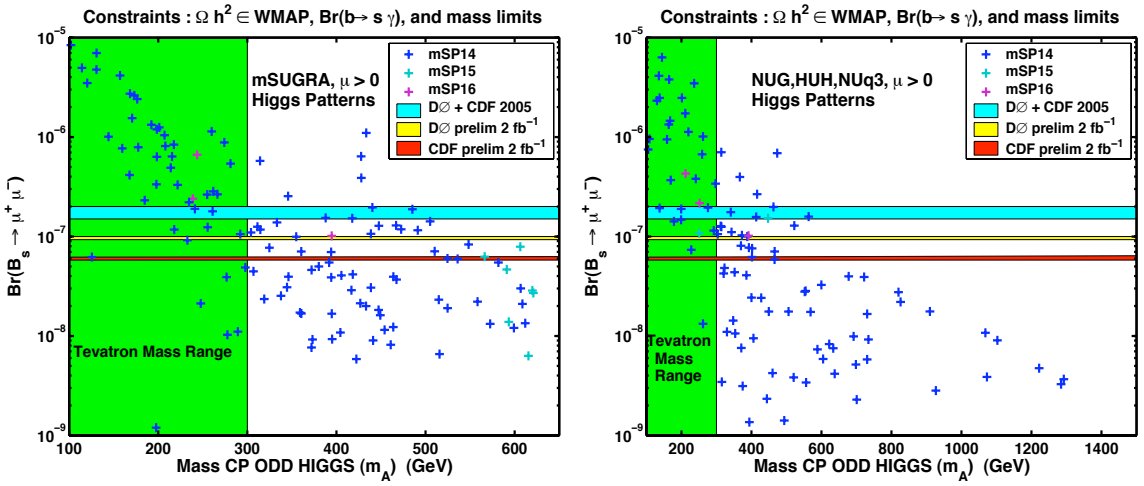

Figure 4.5: Constraints on the HPs at in mSUGRA and NUSUGRA. Limits are drawn in bands extending beyond the Tevatron mass reach (shaded green). (From [45]).

case.

What is very interesting is the fact that for the case $\mu > 0$ the $B_s \to \mu^+\mu^-$ limits, the Tevatron limits on the CP odd Higgs boson production, and the CDMS and Xenon10 limits converge on constraining the Higgs Patterns and specifically the pattern mSP14 and as well as some other patterns.

Thus the CDMS and Xenon10 constraints on the mSPs are strikingly similar to the constraints of $B_s \to \mu^+\mu^-$ from the Tevatron. We also observe that although the case $\mu < 0$ is not currently accessible to the $B_s \to \mu^+\mu^-$ constraint (and may also be beyond the ATLAS/CMS sensitivity for $B_s \to \mu^+\mu^-$), it would, however, still be accessible at least partially to dark matter experiment [45]. The sign of μ is very relevant in the analysis. This is not only because the HPs for mSUGRA case arise only for $\mu > 0$[58],[45], but also due to the fact that the recent results from the $g_\mu - 2$ experiment, where it is well known that the supersymmetric electroweak corrections to $g_\mu - 2$ can be as large or even larger than the Standard Model correction [128]. For large $\tan\beta$ the sign of the supersymmetric correction to $g_\mu - 2$ is correlated with

the sign of μ and the current data [129, 130] on $g_\mu - 2$ favors $\mu > 0$. Therefore it is of great relevance to discuss the possible physics that emerges if indeed one of these patterns is the one that may be realized in nature[45]. Finally we reiterate that the proton-neutralino cross sections act as a discriminator of the SUGRA patterns as it creates a significant dispersion among some of the patterns[45].

4.4 Light Higgs and D-Branes

The advent of D-Branes has led to a new wave of model building [39, 40, 42, 41, 43]. Several Standard Model like extensions have been constructed using intersecting D-Branes [39]. Effective actions and soft breaking in such models have been discussed [40, 41, 44] and there is some progress also on pursuing the phenomenology of intersecting D-Brane models [44, 45, 46]. Here we discuss briefly Higgses and dark matter in the context of D-Branes. We first consider the class of models studied in [40] with a toroidal orbifold compactification based on $\mathcal{T}^6/\mathbb{Z}_2 \times \mathbb{Z}_2$ where $\mathcal{T}^6$ is taken to be a product of 3 $\mathcal{T}^2$ tori. This model has a moduli sector consisting of volume moduli t_m, shape moduli u_m ($m = 1, 2, 3$) and the axion-dilaton field s. The soft breaking terms quoted in this work are [40]

$$M^2_{Q_L} = c^2\left(\frac{1}{3} - \sin^2(\theta) - 2\alpha\cos^2(\theta) + \alpha\cos^2(\theta)[1+F_2]\right) , \tag{4.9}$$

$$M^2_{\bar{U},\bar{D}} = c^2\left(\frac{1}{3} - \frac{1}{2}\cos^2(\theta) + \cos^2(\theta)[F_1(\alpha - \frac{1}{2}) + (1-\alpha)F_2]\right) , \tag{4.10}$$

$$M^2_{U,D} = c^2\left(-\frac{1}{6} + \frac{1}{2}\cos^2(\theta) + \cos^2(\theta)[-\alpha F_1 + (\alpha - \frac{1}{2})F_2]\right) , \tag{4.11}$$

$$M^2_{H_U,H_D} = c^2\left(-\frac{1}{6} + (\frac{1}{2} - \alpha)\cos^2(\theta) + \cos^2(\theta)[\alpha F_1 + (-\frac{1}{2} + 2\alpha)F_2]\right) , \tag{4.12}$$

$$M^2_{S_U,S_D} = c^2\left(-\frac{1}{6} + \left(\frac{1}{2} - \alpha'\right)\cos^2(\theta) + \cos^2(\theta)[(-\frac{1}{2} + 2\alpha')F_1 + \alpha' F_2]\right) \tag{4.13}$$

where $c = \sqrt{3} m_{3/2}[1 + V_0/(3m_{3/2}^2)]^{1/2}$ and α, α' parametrize stack angles, and where

$$\sum_{i=1}^{3} F_i = 1, \quad F_i = |\Theta_{t_i}|^2 + |\Theta_{u_i}|^2 \ , \quad i = 1, 2, 3. \tag{4.14}$$

The soft scalars terms are related via

$$M_{Q_L}^2 = M_L^2 \ , \quad M_{U,D}^2 = M_{\nu,E}^2 \ , \quad M_{\bar{U},\bar{D}}^2 = M_{\bar{\nu},\bar{E}}^2 \ , \tag{4.15}$$

with the tri-linear coupling

$$A^0 = -c \frac{e^{-\rho + \frac{D}{2}}}{\sqrt{f}} \cos(\theta)(\Theta_{t_2} e^{-i\gamma_{t_2}} + \Theta_{u_2} e^{-i\gamma_{u_2}}) \ . \tag{4.16}$$

Here, the parametrization $e^{-i\rho} = \langle \hat{\mathcal{W}} \rangle / |\langle \hat{\mathcal{W}} \rangle|$ where $\hat{\mathcal{W}}$ is related to the gravitino mass through the standard relations in the notation of [17] and the γ_{t_2,u_2} are phases that may contribute to CP violation[40]. The moduli enter through

$$D = -ln(s + \bar{s}) \ , \tag{4.17}$$

$$f = \prod_{m=1}^{3} (t_m + \bar{t}_m) \prod_{m=1}^{3} (u_m + \bar{u}_m) \ . \tag{4.18}$$

A purely dilaton dominated scenario with $\theta = \pi/2$ would not have any soft tri-linear couplings in this model. In the analysis we ignore the exotics, set $F_3 = 0, 0 \leqslant F_1 \leqslant 1$, and use the naturalness assumptions similar to the mSUGRA case with $\mu > 0$. Specifically the parameter space consists of the gravitino mass $m_{3/2}$, the gaugino mass $m_{1/2}$, the tri-linear coupling A_0, $\tan\beta$, the stack angle α ($0 \leqslant \alpha \leqslant \frac{1}{2}$), the Goldstino angle [17] θ, and the the moduli VEVs Θ_{t_i}, Θ_{u_i} ($i = 1, 2, 3$). The analysis shows that the allowed parameter space is dominated by the mSPs with only six new patterns (at isolated points) emerging. Specifically all the HPs (mSP14-mSP16)

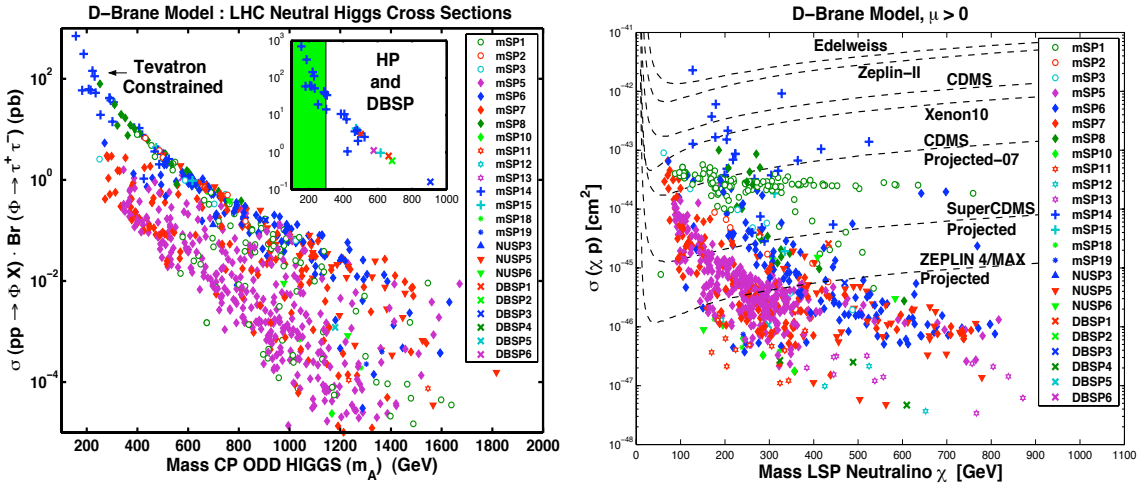

Figure 4.6: Predictions in D-Brane models for $\mu > 0$: The Higgs production cross section $\sigma_{\Phi\tau\tau}(pp)$ at the LHC as a function of the CP odd Higgs mass m_A and the dark matter direct detection signature space. (From [45]).

are seen to emerge in good abundance. Regarding the new patterns we label these patterns D-Brane SUGRA Patterns (DBSPs) since the patterns arise in the SUGRA field point limit of the D-Branes.

Specifically we find six new patterns DBSP$(1-6)$ which repeat here as follows

$$\begin{aligned} &\text{DBSP1} : \widetilde{\chi}_1^0 < \widetilde{\tau}_1 < \widetilde{\nu}_\tau < A/H \ ; \quad \text{DBSP2} : \widetilde{\chi}_1^0 < \widetilde{\tau}_1 < \widetilde{\nu}_\tau < \widetilde{l}_R \ ; \\ &\text{DBSP3} : \widetilde{\chi}_1^0 < \widetilde{\tau}_1 < \widetilde{\nu}_\tau < \widetilde{\nu}_\mu \ ; \quad\quad \text{DBSP4} : \widetilde{\chi}_1^0 < \widetilde{t}_1 < \widetilde{\tau}_1 < \widetilde{\nu}_\tau \ ; \\ &\text{DBSP5} : \widetilde{\chi}_1^0 < \widetilde{\nu}_\tau < \widetilde{\tau}_1 < \widetilde{\nu}_\mu \ ; \quad\quad \text{DBSP6} : \widetilde{\chi}_1^0 < \widetilde{\nu}_\tau < \widetilde{\tau}_1 < \widetilde{\chi}_1^\pm \ . \end{aligned} \tag{4.19}$$

DBSPs	$m_{3/2}$ (GeV)	$m_{1/2}$ (GeV)	A_0 (GeV)	$\tan\beta$	α	$\cos^2\theta$	F_1
DBSP1	3654	1018	-331	51.5	0.444	0.705	0.086
DBSP4	1962	777	5863	9.4	0.430	0.790	0.260
DBSP5	2114	718	3512	21.3	0.448	0.688	0.051

Table 4.4: Some Benchmarks for D-Brane models DBSPs. (From [45]).

The analysis of the Higgs production cross section $\sigma_{\Phi\tau\tau}(pp)$ in the D-Brane models at the LHC is given in the left panel of left panel of Fig.(4.6). The analysis shows that the HPs again dominate the Higgs production cross sections. One also finds that the $B_s \to \mu^+\mu^-$ experiment constraints the HPs in this model [45]. The scalar dark matter cross sections are given in the right panel of Fig.(4.6). Here also one finds that the Higgs Patterns typically give the largest scalar cross sections followed by the Chargino Patterns (mSP1-mSP3) and then by the Stau Patterns. Further, one finds that the Wall of Chargino Patterns persists in this case as well.

4.5 Compressed Spectra in Intersecting D-Brane Models

We consider next another class of intersecting D-Brane models motivated by the analyses of [41, 42]. The specific class of models we consider is with u moduli breaking. The model consists of a chiral particle spectrum arsing from intersecting branes with supporting gauge groups $SU(3)_C \times SU(2)_L$ and $U(1)_a$,$U(1)_c$, $U(1)_d$ and $U(1)_Y$, with charge assignments given in [44]. The anomalous $U(1) = U(1)_a + U(1)_d$ is assumed canceled by a Green-Schwarz mechanism giving a Stueckelberg mass to the U(1) gauge boson. We will have much to say about Stueckelberg masses in the coming chapters.

The Kähler metric for the twisted moduli arising from strings stretching between stacks P and Q for the BPS 1/4 sector is taken in the form similar to [42], and more specifically of the form given in [44]

$$\tilde{\mathcal{K}}_{C_{\theta_{PQ}}\bar{C}_{\theta_{PQ}}} \equiv \tilde{\mathcal{K}}_{PQ} = e^{\phi_4}\left[e^{\gamma_E\,\Sigma_{j=1}^{3}\theta^j_{PQ}}\prod_{j=1}^{3}\left[\sqrt{\Gamma(1-\theta^j_{PQ})/\Gamma(\theta^j_{PQ})}\;\;(t^j+\bar{t}^j)^{-\theta^j_{PQ}}\right]\right], \tag{4.20}$$

where $\theta^j_{PQ} = \theta^j_P - \theta^j_Q$ is the angle between branes in the j^{th} torus and ϕ_4 is the four

dimensional dilaton

$$\phi_4 = -\log(2\pi) - \frac{1}{4}\log\Big[\Re(s)\prod_{i=1}^{3}\Re(u^i)\Big] \ . \tag{4.21}$$

The gauge kinetic function is

$$f_P = k_P^{-1}\left(n_P^1 n_P^2 n_P^3 s - n_P^1 m_P^2 m_P^3 u^1 - n_P^2 m_P^1 m_P^3 u^2 - n_P^3 m_P^1 m_P^2 u^3\right) \ , \tag{4.22}$$

where the Brane integers are given in [44] and the hypercharge normalization is [131, 132, 44] $Q_Y = (1/6)Q_a - (1/2)Q_c - (1/2)Q_d$. Note k_P^{-1} falls out in the *ratio* when computing the gaugino masses. The F term is parametrized by[17]

$$F^{u^j} = 2\sqrt{3}m_{3/2}\Theta_j e^{-i\gamma_j}\Re(u^j) \ . \tag{4.23}$$

Using the parametrization for the gaugino masses in [17] we generalize the gaugino masses relations to [133]

$$\begin{aligned} M_{\tilde{g}} = M_a &= \frac{9\rho^4\sqrt{3}m_{3/2}\Theta_1 e^{-i\gamma_1}\Re(u^1)}{\Re(s)+9\rho^4\Re(u^1)} \\ M_{\tilde{W}} = M_b &= \sqrt{3}m_{3/2}\Theta_2 e^{-i\gamma_2} \\ M_{\tilde{B}} = M_{f_Y} &= \frac{3\sqrt{3}m_{3/2}\rho^2\left(12\rho^2\Theta_1 e^{-i\gamma_1}\Re(u^1)+\Theta_3 e^{-i\gamma_3}\Re(u^3)\right)}{4\Re(s)+36\rho^4\Re(u^1)+3\rho^2\Re(u^3)} \ , \end{aligned} \tag{4.24}$$

which reduces down to the expression in [44] for the unification constraints imposed and choice of ρ taken. We do, however, find a more general case of unification constraints[133], although this plays no role in the ensuing discussion.

The BPS 1/4 scalar sector masses are determined through

$$-M_{P,Q}^2 = \sum_{\{M,N\}}^{3}\bar{F}^{\bar{M}}F^N\frac{\partial}{\partial\bar{M}}\frac{\partial}{\partial N}\log(\tilde{\mathcal{K}}_{P,Q}) - \left(m_{3/2}^2+V_0\right) \ , \tag{4.25}$$

which yields after some calculation under the tuning $V_0 \to 0$ (note we keep the complex conjugation of Θ)

$$\frac{M^2_{P,Q}}{m^2_{3/2}} = \left(1 - 3\sum_{m=1}^{3}\sum_{n=1}^{3}\Theta_m\Theta^*_n e^{-i(\gamma_m-\gamma_n)}\left(\sum_{j=1}^{3}\left(\Psi^{'}(\theta^j_{P,Q})\theta^{j,m}_{P,Q}\theta^{j,\bar{n}}_{P,Q} + \Psi\left(\theta^j_{P,Q}\right)\theta^{j,m\bar{n}}_{P,Q}\right) + \frac{\delta_{m,n}}{4}\right)\right) , \tag{4.26}$$

where in the above $\Psi(\theta^j_{P,Q}) = \partial_{\theta^j_{P,Q}}(\log(\tilde{\mathcal{K}}_{PQ}/e^{\phi_4}))$ and the first term $\Psi^{'}(\theta^j_{P,Q})$ is the derivative of $\Psi(\theta^j_{P,Q})$. The terms $\theta^{j,m}_{P,Q}$ and $\theta^{j,m\bar{n}}_{P,Q}$ are derivatives with respect to the angles $\theta_{P,Q}$ (multiplied by the u moduli) and are given as in [44]. The tri-linears are assumed as

$$A_{P,Q,R} = -\sum_M F^M \frac{\partial}{\partial M}\log\left(\tilde{\mathcal{K}}_{P,Q}\tilde{\mathcal{K}}_{Q,R}\tilde{\mathcal{K}}_{R,P}\right) , \tag{4.27}$$

which on expansion becomes

$$\begin{aligned} A_{P,Q,R} &= \frac{\sqrt{3}}{2}m_{3/2}\Theta_1 e^{-i\gamma_1} + \\ &\quad -\sqrt{3}m_{3/2}\sum_{i=1}^{3}\Theta_i e^{-i\gamma_i}\left(1 + \sum_{k=1}^{3}\left(\Psi\left(\theta^k_{P,Q}\right)\theta^{k,i}_{P,Q} - \frac{1}{4}\right) + [(P,Q)\to(R,P)]\right) . \end{aligned} \tag{4.28}$$

The Kähler metric for 1/2 BPS brane configurations is given by

$$\tilde{\mathcal{K}}^{Higgs}_{PQ} = \left((s+\bar{s})(u^1+\bar{u}^1)(t^2+\bar{t}^2)(t^3+\bar{t}^3)\right)^{-1/2} , \tag{4.29}$$

which very simply gives $M^2_{H_U,H_D} = m^2_{3/2}\left(1 - \frac{3}{2}|\Theta_1|^2\right)$ again under the tuning $V_0 \to 0$. We compute the soft parameters and find agreement with those given in the appendix of [44]. Here we give the soft parameters in a useful analytic form in terms of the input which is the angle α (the free angle between the P^{th} brane and the orientifold plane of and the j^{th} torus which is assumed factorized as in the previous section) and the real parts of the u_1, t_2, t_3 moduli, and Θ_2, Θ_3 for the choice $\rho = 1$. Here we

compute the tri-linears in terms of the said parameters, and it is found that

$$A_{a,b,c} = \frac{\sqrt{3}m_{3/2}}{4\pi}\Big[-2\pi(\Theta_2+\Theta_3) + S_\alpha(\Theta_3-\Theta_2)(\Psi(-1/2-\alpha)-\Psi(1/2-\alpha)) \\ +\Theta_1(\Psi(-1/2-\alpha)+\Psi(1/2-\alpha)-2\Psi(\alpha))\Big] ,$$

$$A_{a,b,\bar{c}} = -\frac{\sqrt{3}m_{3/2}}{4\pi}\Big[2\pi(\Theta_2+\Theta_3)+2S_\alpha\Theta_1(-\Psi(1/2-\alpha)+\Psi(\alpha))\Big] , \quad (4.30)$$

with $A_{a,b,c} = A_{Q_L,H_u,U_R} = A_{L,H_u,N_R}$ and $A_{a,b,\bar{c}} = A_{Q_L,H_d,D_R} = A_{L,H_d,E_R}$. The soft scalar masses are found to be

$$\begin{aligned} M^2_{a,b} &= \frac{m^2_{3/2}}{4} - \mathcal{D}\Psi(1/2-\alpha)\frac{3m^2_{3/2}S^2_\alpha}{16\pi^2}\left(1-2\Theta_3\Theta_1+2\Theta_2\left(-\Theta_3+\Theta_1\right)\right) \quad (4.31)\\ &+ \mathcal{D}\Psi(\alpha)\frac{3m^2_{3/2}S^2_\alpha}{16\pi^2}\left(-1-2\Theta_3\Theta_1+2\Theta_2\left(\Theta_3+\Theta_1\right)\right)\\ &+ \Psi(1/2-\alpha)\frac{3m^2_{3/2}S_\alpha}{8\pi}\left(-2+C_\alpha+4\Theta_3^2-2C_\alpha\Theta_3\Theta_1+2C_\alpha\Theta_2\left(-\Theta_3+\Theta_1\right)\right)\\ &+ \Psi(\alpha)\frac{3m^2_{3/2}S_\alpha}{8\pi}\left(2-C_\alpha-4\Theta_2^2-2C_\alpha\Theta_3\Theta_1+2C_\alpha\Theta_2\left(\Theta_3+\Theta_1\right)\right) . \end{aligned}$$

For $M^2_{a,c}$ simply make the replacements in Eq.(4.31) so that $\mathcal{D}\Psi(1/2-\alpha)\to\mathcal{D}\Psi(-\alpha)$, $\mathcal{D}\Psi(\alpha)\to\mathcal{D}\Psi(1/2+\alpha)$, $\Psi(1/2-\alpha)\to\Psi(-\alpha)$, and $\Psi(\alpha)\to\Psi(1/2+\alpha)$. For $M^2_{a,\bar{c}}$ make the replacements in Eq.(4.31) so that $\mathcal{D}\Psi(1/2-\alpha)\to\mathcal{D}\Psi(-\alpha)$, $\mathcal{D}\Psi(\alpha)\to\mathcal{D}\Psi(-1/2+\alpha)$, $\Psi(1/2-\alpha)\to\Psi(-\alpha)$, and $\Psi(\alpha)\to\Psi(-1/2+\alpha)$. Here $M^2_{a,b} = m^2_{Q_L} = m^2_L$, and $M^2_{a,c} = m^2_{U_R} = m^2_{N_R}$ and $M^2_{a,\bar{c}} = m^2_{D_R} = m^2_{E_R}$. In the above we have explicitly written out the relevant factors. They enter in terms of trigonometric (the trig functions enter as a consequence of an identity between two poly-gamma functions after differentiating Ψ) and separate poly-gamma functions of the angle α and the moduli which gives:

$$\mathcal{D}\Psi(x) = \frac{\pi^2}{2}\csc^2\pi x - PG(1,x) \quad (4.32)$$

$$\Psi(\alpha) = \gamma_E - \frac{1}{2}\pi\cot\pi(\alpha) - \log[2\Re(t_2)\cdot PG(0,\alpha)] \quad (4.33)$$

$$\Psi(-\alpha) = \gamma_E - \frac{1}{2}\pi\cot\pi(-\alpha) - \log[2\Re(t_3)\cdot PG(0,-\alpha)] \quad (4.34)$$

$$\Psi(1/2-\alpha) = \gamma_E - \frac{1}{2}\pi\cot\pi(1/2-\alpha) - \log[2\Re(t_3)\cdot PG(0,1/2-\alpha)] \quad (4.35)$$

$$\Psi(1/2+\alpha) = \gamma_E - \frac{1}{2}\pi\cot\pi(1/2+\alpha) - \log[2\Re(t_2)\cdot PG(0,1/2+\alpha)] \quad (4.36)$$

$$\Psi(-1/2+\alpha) = \gamma_E - \frac{1}{2}\pi\cot\pi(-1/2+\alpha) - \log[2\Re(t_2)\cdot PG(0,-1/2+\alpha)] \quad (4.37)$$

where

$$PG(n,z) = \frac{d^n}{dz^n}\left[\frac{1}{\Gamma(z)}\frac{d\Gamma(z)}{dz}\right] , \quad (4.38)$$

$$|\Theta_1| = \sqrt{1-|\Theta_2|^2-|\Theta_3|^2} \quad \text{and} \quad S_\alpha \equiv \sin 2\pi\alpha \qquad C_\alpha \equiv \cos 2\pi\alpha \ . \quad (4.39)$$

Sparticle type	D6 Mass/GeV	mSUGRA Mass/GeV
m_h	113.9	113.6
$\widetilde{\chi}_1^0$	209.0	208.8
$\widetilde{\chi}_1^\pm$	229.1	388.6
$\widetilde{\chi}_2^0$	229.5	388.8
$\widetilde{\tau}_1$	404.2	433.3
$\widetilde{e}_R, \widetilde{\mu}_R$	464.4	637.8
$\widetilde{\tau}_1$	547.6	929.2
$\widetilde{g}$	760.4	1181.4
$m_{\max=\tilde{s},\tilde{d}_L}$	882.2	$m_{\max=\tilde{s},\tilde{d}_L}$ 1210.4

Table 4.5: Comparison of two models, an Intersecting D-Brane model (D6) and mSUGRA. Here the LSP mass and light Higgs masses are almost identical, however their is (a) a gross violation of scaling seen in the D6 model, and (b) a compressed spectra in the D6 model case. Both models sit in the same hierarchical mass pattern for the first 4 sparticles. The SUSY Higgses (not shown) for the mSUGRA model are however 100 GeV lighter ($\sim$ 500 GeV) than the D6 case. ([133].)

D6	mSUGRA
$(\tilde{B}, \tilde{W}, \tilde{H}_1, \tilde{H}_2)$	$(\tilde{B}, \tilde{W}, \tilde{H}_1, \tilde{H}_2)$
(0.985,-.133,.104,-.0399)	(0.994,-.017,.101,-.041)
$\sigma^{\rm SI}_{\tilde{\chi}^0_1 p} = 7.4 \times 10^{-9}$ pb	$\sigma^{\rm SI}_{\tilde{\chi}^0_1 p} = 1.4 \times 10^{-8}$ pb
$\Omega h^2 = 0.099$ co-annh.	$\Omega h^2 = 0.095$ $b\bar{b}, \bar{\tau}\tau$

Table 4.6: Comparison of the same two models, Intersecting D-Brane model (D6) and mSUGRA. The two models produce the correct relic density, but through very different means, the D6 model co-annihilated through both gaugino co-annhilations and slepton co-annhilations while the mSUGRA model annihilated into heavy flavors. The Wino content is much larger in the D6 model than the mSUGRA model case, and the mSUGRA model case produces a stronger spin independent cross section. ([133].)

In Table(4.5) we give a comparison of 2 model points[1]. One from the D-Brane model (which we shall call D6) and the other from mSUGRA. The features discussed below are found to be rather generic over the parameter space investigated in the D6 model. In the D6 model we find some very interesting features. First, we are comparing the two model points which sit in the same 4 particle mass hierarchy with effectively the same LSP mass and light CP even Higgs mass. We see from Table(4.5) that there is a major violation of mass scaling in D6 relative to that of the mSUGRA model (for a discussion of scaling see Chapter(6.3)). Further, the scale in the D6 model is much compressed relative to that of the mSUGRA model. Thus while the LSP masses are effectively identical, the NLSP mass in the D6 model is about 160 GeV lighter than in the mSUGRA case considered. Further, the gluino is several hundred GeV lighter in the D6 case relative to the mSUGRA case and the heaviest sparticle in the D6 cases lies lower than the mSUGRA case by approximately 300 GeV.

In Table.(4.5) we see that the D6 LSP has a relatively larger wino component, while the mSUGRA model point is more a mixed bino-Higgsino but with a stronger

[1]We note in passing that unlike in sugra models, in string models the bi-linear soft term B is determined. Since on using radiative breaking of the electroweak symmetry, B is traded with $\tan\beta$, one finds that $\tan\beta$ is no longer a free parameter as in sugra models but is determined in terms of the moduli[134]. This constraint is ignored in the analysis here.

bino component. Both models satisfy the relic density constraint but do so in very different ways, as discussed in the caption however the spin independent cross section for the mSUGRA case is about a factor of 2 larger.

The above observations leads us to some rather important conclusions: (a) Although the sparticle mass hierarchy concept is extremely useful for sorting out SUSY, there are cases where it does not provide the full picture. (b) The scaling of gaugino masses is a crucial ingredient to sorting out the underlying class of models here. (c) It is possible that with non-universalities, the spectrum of sparticles may be compressed (while still satisfying all mass limit constraints and flavor constraints). The above calls for a more vigorous study of these classes of models which give rise to non-universalities as their implications for colliders have yet to be explored in great detail[133].

4.6 The Big Picture

We now turn to the central idea. That is, the correlation of LHC signals with dark matter direct detection signals. The correlation is exhibited in Fig.(4.7). The top panel gives an analysis at $L = 10$ fb^{-1} admitting only those model points in the parameter space that generate at least 500 total SUSY events for statistical significance in the normalized channels $[2bjets + jets \geq 2]/N_{\rm SUSY}$ vs. $[1bjet + jets \geq 2]/N_{\rm SUSY}$ and average $P_T^{\rm miss}$ vs. $[0bjets + jets \geq 2]/N_{\rm SUSY}$. The middle panels are 4 mSPs in the pulled out of the left panel of Fig.(4.2) in the $\sigma^{\rm SI}_{\widetilde{\chi}^0_1 p}$ vs. LSP signature space. Finally the bottom two panels show effective mass distributions for sample benchmarks for different mSPs. One observes a large separation among many of the hierarchical patterns in the plots, as can be seen, in Fig.(4.7). The top left panel exhibits separation of CPs and HPs from SOPs and SUPs, with CPs and HPs occupying one region,

and SOPs and SUPs occupy another in this signature space except for a very small overlap. The average missing P_T for each parameter point vs. the fraction of events with $0b$ also shows a separation of the CPs and HPs from SOPs and SUPs. Further, mSP4 appears isolated in this plot. Meanwhile the central panel shows the direct detection limits and a remarkable separation of the mass patterns is achieved. The bottom panel also shows a very interesting effect. The left bottom panel shows kinematical distributions in effective mass where only trigger level cuts imposed, while the right panel has post trigger level cuts imposed and they have been imposed globally for all the models considered (see the Appendix(4.8) for these cuts). For the case when only trigger level cuts are imposed, the SOPs and CPs are highly peaked at lower values of effective mass, while the HPs and SUPs are much broader at higher effective mass. However the trigger level cuts can have an enormous effect on the observability of these signals. We see here an important point. Imposing the post trigger level cuts globally on all classes of hierarchical mass patterns may disguise the signal. Applying our post trigger level cuts kills the SOP and CP signals, while the SUPs and HPs signals remain relatively strong. This is a consequence of what was discussed in Ch.(3), namely that the missing P_T is very important in the analysis of deciphering the model (the effective mass is the missing P_T + the sum of the jet P_T). We observe these effects more generally. Namely that the effective mass and the missing P_T distributions for the SOPs and CPs are generally much narrower, while the HPs and SUPs are generally much broader. Therefore it becomes crucial for experimental groups to design their triggers around different scenarios, in particular, as we illustrated here, the triggers need to be specialized for different mass hierarchies.

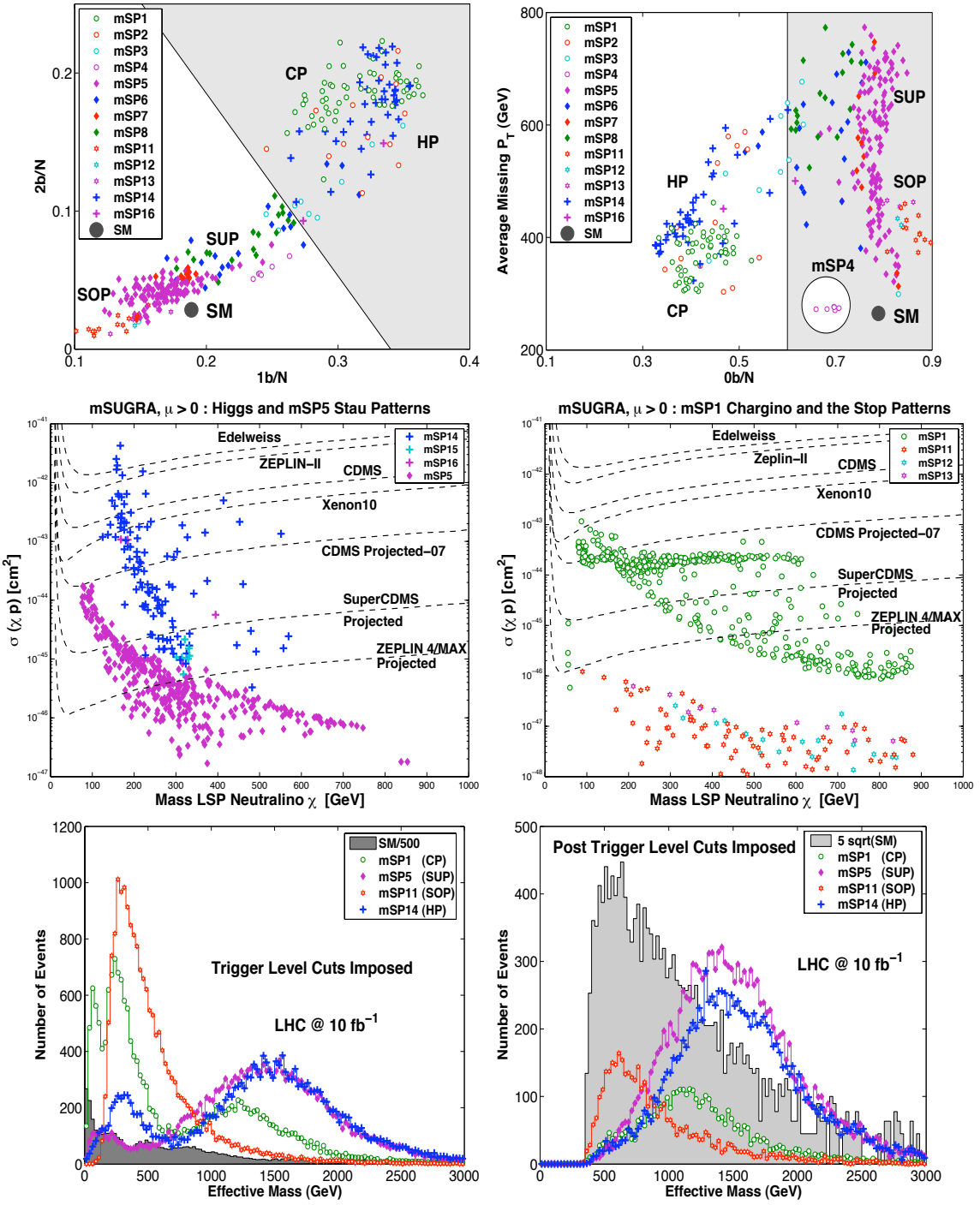

Figure 4.7: The Big Picture as discussed in the text- Bringing together direct detection, LHC event rates and kinematic signatures of new physics . The top panel is full simulation of ~ 900 model points for minimal SUGRA at the LHC with 10/fb keeping only statistically significant model points as discussed in the text. The middle panel has a larger set of data, but correspond otherwise to same set of models in the top panel where the low mass points make the cut in the top panel. The bottom panels are eff. mass dist. for 4 benchmarks with and without (the same) post trigger level cuts. From [45] and [60].

The analysis given in Fig.(4.7), is really a central result of our work [58, 45, 87]. It provides correlations amongst various sparticle mass hierarchies, not only in the space of LHC signatures but also in the signature space of direct detection. These types of correlations become very important in our quest to pin down the the underlying model in any framework. We note also, that a glance back at, for example, the left panel of Fig.(4.2), shows that while stops patterns may be discoverable at the LHC, quite remarkably they will almost certainly not be detectable in DM detection experiments.

4.7 Summary

Higgs Patterns (HPs)[58] arise in a wide range of models: in mSUGRA, in NUSUGRA and in D-Brane models [45]. The HPs are typically seen to lead to large Higgs production cross sections at the Tevatron and at the LHC, and to the largest $B_s \to \mu^+\mu^-$ branching ratios, and thus are the first to be constrained by collider experiments [45]. Further the HPs lead typically to the largest neutralino-proton cross sections and would either be the first to be observed or the first to be constrained by dark matter experiments[45]. There exists of a Chargino Wall which give a $\sigma^{\rm SI}_{\widetilde{\chi}^0_1 p}$ at the level of $\sim \mathcal{O}(10^{-44})$ cm^2 in all models considered for the LSP mass extending up to 900 GeV[45, 87]. These results heighten the possibility for the observation of dark matter in improved dark matter experiments such as SuperCDMS[99], ZEPLIN-MAX[135], and LUX[116] which are expected to reach a sensitivity of 10^{-45} cm^2 or more. We note that many of the hierarchical patterns are well separated in the $\sigma^{\rm SI}_{\widetilde{\chi}^0_1 p}$- LSP mass plots, providing important signatures along with the signatures from colliders for mapping out the sparticle parameter/signature space[58, 60, 87]. An analysis of soft breaking in D-Brane models was given and several important observations were noted regarding light Higgses, the presence of the Chargino Wall, and compresses spectra in certain classes of models based on Branes which lead to non universal soft breaking.

More generally, the notion of sparticle mass hierarchies plays a crucial role for the discovery of new physics at both the LHC and in DM experiments acting like a prism in the separating out of the sparticle landscape.

4.8 Appendix: Experimental Constraints

This appendix summarizes various aspects of the analysis [58, 45, 60, 87].

Experimental limits on the FCNC process $b \to s\gamma$ give rise to tight constraints on SUSY models. Here we have imposed the constraint from the Heavy Flavor Averaging Group (HFAG) [136] along with the BABAR, Belle and CLEO experimental results: $\mathcal{B}r(b \to s\gamma) = (355 \pm 24^{+9}_{-10} \pm 3) \times 10^{-6}$. A new estimate of $\mathcal{B}r(\bar{B} \to X_s\gamma)$ at $O(\alpha_s^2)$ gives [137] $\mathcal{B}r(b \to s\gamma) = (3.15 \pm 0.23) \times 10^{-4}$ and moves the previous SM mean value of 3.6×10^{-4} a bit lower. In the analysis we use a 3.5σ error corridor around the HFAG value. The total $\mathcal{B}r(\bar{B} \to X_s\gamma)$ including the sum of SM and SUSY contributions (for the update on SUSY contributions see [138]) are constrained by this corridor. The process $B_s \to \mu^+\mu^-$ can become significant for large $\tan\beta$ since the decay has a leading $\tan^6\beta$ dependence and thus large $\tan\beta$ may be constrained by the current limit which is $\mathcal{B}r(B_s \to \mu^+\mu^-) < 1.5 \times 10^{-7}$ (90% CL), 2.0×10^{-7} (95% CL) [139]. More recently the CDF and DØ have given limits which are about a factor of 10 more sensitive. We have included these preliminary [140] results in this analysis. Additionally, we also impose the current lower limits on the lightest CP even Higgs boson. For the Standard Model like Higgs boson this limit is ≈ 114.4 GeV [141], while a limit of 108.2 GeV at 95% CL is set on the production of an invisibly decaying Standard Model like Higgs by OPAL [141]. For the MSSM we take the constraint to be $m_h > 100$ GeV. This relaxed constraint poses little restriction on the models discussed here. We take the other sparticle mass constraints to be (1) for the lighter

chargino $m_{\widetilde{\chi}_1^\pm} > 104.5$ GeV [142] (2) for the lighter stop $m_{\widetilde{t}_1} > 101.5$ GeV, and (3) for the lighter stau $m_{\widetilde{\tau}_1} > 98.8$ GeV [143]. The mSUGRA analysis is based on a large Monte Carlo scan of the parameter space with the soft parameters in the range $0 < m_0 < 4000$ GeV, $0 < m_{1/2} < 2000$ GeV, $|A_0/m_0| < 10$, $1 < \tan\beta < 60$ and both signs of μ are analyzed. For the case of non-universalities we let each δ vary between $[-0.9, 1]$. In our analysis we use MicrOMEGAs version 2.0.7 [95] and for some calculations v2.2 have been used as a cross check. Our RGE calculator is the SuSpect 2.34 package [94] used for the analysis of sparticle masses and mixings, and we taken $m_b^{\overline{\rm MS}}(m_b) = 4.23$ GeV, $m_t(\text{pole}) = 170.9$ GeV, requiring REWSB at the SUSY scale. We have cross checked our analysis with other codes [80, 144, 145, 146, 147, 148, 149] and find no significant disagreement for the models discussed here. In addition to the above one may also consider the constraints from the anomalous magnetic moment of the muon. It is known that the supersymmetric electroweak corrections to $g_\mu - 2$ can be as large or larger than the Standard Model electroweak corrections[128]. The implications of recent experimental data has been discussed in several works (see, e.g.[153]). As in [143], here we use a rather conservative bound $-11.4 \times 10^{-10} < \delta(g_\mu - 2) < 9.4 \times 10^{-9}$.

We remark that a very unique and interesting analysis has subsequently studied mSP4 [61] in the context of helicity amplitudes. Also, recently the mSP concept has been implemented in the analyses of [150], but in the P-MSSM which finds all but one of our mSP patterns (likely that saturation not yet to be achieved in the larger pool of parameters in the P-MSSM). Also several other the patterns for the non universal cases are seen in this work. The hierarchical mass pattern approach has also been adopted in [152]. We have also uncovered the hierarchical mass pattern from a large data set from [151] and find a similar frequency of the mSPs in this data set as found in our original data set [58].

Collider Simulations for SUSY Processes[58, 45, 60, 87]

Candidate model points for the signature analysis are found after the imposition of all the constraints mentioned above. For each of these model points, a SUSY Les Houches Accord (SLHA) file [96] is interfaced to PYTHIA 6.4.11 [79] through PGS4 [97] for the computation of SUSY production cross sections and branching fractions. In this analysis, for signals, we have generated all of PYTHIA's $2 \to 2$ SUSY production modes using MSEL = 39. This choice generates 91 SUSY production modes including gaugino, squark, slepton, and SUSY Higgs pair production, while an analysis of singly produced Higgs production was also given. For further details regarding these modes, see [79]. Leading order cross sections from PYTHIA and leading order cross sections from PROSPINO 2.0 [154] were cross checked against one another for consistency over several regions of the soft parameter space. TAUOLA [155] is called by PGS4 for the calculation of tau branching fractions as controlled in the PYTHIA parameter card (.pyt) file. With PGS4 we use the Level 1 (L1) triggers designed to mimic the Compact Muon Solenoid detector (CMS) specifications [156, 110] and the LHC detector card. Muon isolation is controlled by employing the cleaning script in PGS4. We take the experimental nomenclature of lepton being defined only as electron or muon and thus distinguish electrons and muons from tau leptons. SM backgrounds have been generated with QCD multi-jet production due to light quark flavors, heavy flavor jets ($b\bar{b}$, $t\bar{t}$), Drell-Yan, single Z/W production in association with quarks and gluons ($Z+$ jets / $W+$ jets), and ZZ, WZ, WW pair production resulting in multi-leptonic backgrounds. Extraction of final state particles from the PGS4 event record is accomplished with a code SMART (= SUSY Matrix Routine) written by us [58] which provides an optimized processing of PGS4 event data files. The standard criteria for the discovery limit of new signals is that the SUSY signals should exceed either

$5\sqrt{N_{\rm SM}}$ or 10 whichever is larger, i.e., $\mathrm{N_{SUSY}} > \mathrm{Max}\left\{5\sqrt{N_{\rm SM}}, 10\right\}$ and such a criteria is imposed where relevant. We have cross checked our SM backgrounds and several other elements of our analysis with simulations done by CMS [157, 158] and the results of these checks are in good agreement as well as the total background analysis of [55] under similar cuts used there. In PGS4 jets are defined through a cluster-based algorithm which has a heavy flavor tagging efficiency based on the parametrizations of the CDF Run 2 tight/loose SECVTX tagger [159] and is a displaced (secondary) vertex b-tagging algorithm which allows detection of b quarks. The b-tagging efficiency enters as a product of two polynomials each a separate function of $|\eta(jet)|$ and $P_T(jet)$. The efficiency is maximized in the region $|\eta(jet)| < 1$ with maximal efficiency $\epsilon_b = (0.4, 0.5)$ for tight and loose tags respectively, and falls off sharply for $|\eta(jet)| > 1$ with virtually zero efficiency out near $|\eta(jet)| = 2$ and $P_T(jet) \sim 160$ GeV. It remains to be seen if the CMS and ATLAS detectors will have greater efficiency at larger P_T, and preliminary reports appear to indicate this maybe possible.

Post Trigger Level Cuts for SUSY [58, 45, 60, 87]

Our post trigger level cuts are designed to highlight the SUSY signatures with respect to the SM background over a broad set of models. We list them below: (1) In an event, we only select photons, electrons, and muons that have transverse momentum $P_T(p) > 10$ GeV and $|\eta(p)| < 2.4$, $p = (\gamma, e, \mu)$; (2) For hadronically decaying tau (jets): $P_T(\tau) > 10$ GeV and $|\eta(\tau)| < 2.0$ are selected; (3) For other hadronic jets only those satisfying $P_T(jet) > 60$ GeV and $|\eta(jet)| < 3.0$ are selected; (4) We require a large amount of missing transverse momentum, $P_T^{miss} > 200$ GeV; (5) There are at least two jets that satisfy the P_T and η cuts. Variations on these cuts are discussed in the text.

Chapter 5

The Stueckelberg Mechanism for Mass Generation

We have already discussed that realistic models of particle physics have been constructed implementing the properties of D-Branes which support chiral matter. Progress along these lines include the possibility of the replication of the chiral structure of the Standard Model (SM) in classes of intersecting D-Brane models and models for which the D-Branes sit at singularities (for a review see [43]). In these top-down approaches to building realistic models based on D-Branes the SM gauge group can be produced but one also encounters residual Abelian group factors. The extra $U(1)$s usually correspond to massive vector fields. In particular frameworks they lead to terms in the action of the form $B \wedge F$, i.e. terms of the form $\frac{1}{2}\epsilon^{\mu\nu\alpha\beta}B_{\mu\nu}F_{\alpha\beta}$ which are needed for anomaly cancellation via a [four dimensional] Green-Schwarz (GS) mechanism [160]. In other frameworks the $B \wedge F$ couplings can arise for the non-anomalous cases as well[132],[167, 169, 184],[43]. These types of couplings can give rise to Stueckelberg mass terms. For example, under the duality transformation $\partial_\mu \sigma \sim \epsilon_{\mu\nu\rho\sigma}\partial^\nu B^{\rho\sigma}$, as illustrated in [43], vector fields gain mass via the GS mechanism leading to Stueckelberg

mass terms in the Lagrangian of the form

$$\mathcal{L}_{\rm St} = -\frac{1}{2}\sum_I (\partial^\mu \sigma^I - k^{Ia} C_a^\mu)^2, \tag{5.1}$$

where the index I runs over all the 4D tensors and thus runs over each of psuedoscalars σ^I (Ramond axions) and over the killing vector coefficients k^{Ia}. Here a indexes a Brane stack with a supporting gauge group (for example: $U(N_a) = SU(N_a) \times U(1)_a$) with each Abelian vector field denoted as C_a^μ. It is then clear that the quadratic term for C_a^μ in Eq.(5.1) gives rise to mass terms for the Abelian vector fields. The orthogonality of the killing vectors dictates which Bosonic states will become massive or if they are massless. Adding a gauge fixing terms, the cross terms in Eq.(5.1) cancel i.e. the psuedoscalars and vector fields decouple. The mechanism outlined here is distinct from a Higgs mechanism for mass generation of a $U(1)$ gauge field. There is no such residual scalar present in this mechanism for mass growth.

One can see this is in a simpler way. Consider a Kalb-Ramond 3 form [161] (see also [162])

$$H_{\mu\nu\rho} = \partial_\mu B_{\nu\rho} + \partial_\nu B_{\rho\mu} + \partial_\rho B_{\mu\nu}, \tag{5.2}$$

and consider the Lagrangian

$$L_0 = -\frac{1}{4}F_{\mu\nu}F^{\mu\nu} - \frac{1}{12}H^{\mu\nu\rho}H_{\mu\nu\rho} + \frac{M}{4}\epsilon^{\mu\nu\rho\sigma}F_{\mu\nu}B_{\rho\sigma}. \tag{5.3}$$

The last term can be written in terms of a psuedoscalar [1]

$$-\frac{M}{6}\epsilon^{\mu\nu\rho\sigma}(H_{\mu\nu\rho}A_\sigma + \hat{\sigma}\partial_\mu H_{\nu\rho\sigma}). \tag{5.4}$$

[1] $\sigma \equiv M\hat{\sigma}$ (where $\hat{\sigma}$ carries no mass dimension)

An integration over $\hat{\sigma}$ gives back L_0 [132, 163]. Instead solving for $H^{\mu\nu\rho}$ yields

$$H^{\mu\nu\rho} = -M\epsilon^{\mu\nu\rho\sigma}(A_\sigma + \partial_\sigma\hat{\sigma}). \tag{5.5}$$

An integration on $H^{\mu\nu\rho}$ gives L_0 in the form

$$L_1 = -\frac{1}{4}F_{\mu\nu}F^{\mu\nu} - \frac{M^2}{2}(A_\sigma + \partial_\sigma\hat{\sigma})^2. \tag{5.6}$$

That is, we are lead to mass growth for the $U(1)$ boson A_σ through a Stueckelberg mechanism.

Thus, through a Stueckelberg mechanism [164] an Abelian gauge boson develops mass without the benefit of a Higgs mechanism [165] (for an interesting historical document regarding the Stueckelberg mechanism see [166]). The basic Lagrangian for a single Abelian group can be written similarly to the above

$$\mathcal{L}_0 = -\frac{1}{4}\mathcal{F}_{\mu\nu}\mathcal{F}^{\mu\nu} - \frac{1}{2}(mA_\mu + \partial_\mu\sigma)(mA^\mu + \partial^\mu\sigma)\ , \tag{5.7}$$

where the psuedoscalar σ undergoes an axionic shift symmetry, i.e. the Lagrangian is gauge invariant under the transformations $\delta A_\mu = \partial_\mu\lambda\ ,\quad \delta\sigma = -m\lambda$. With the gauge fixing term $\mathcal{L}_{\rm gf} = -\left(\partial_\mu A^\mu + \xi m\sigma\right)^2/2\xi$, the total Lagrangian reads

$$\mathcal{L} = -\frac{1}{4}\mathcal{F}_{\mu\nu}\mathcal{F}^{\mu\nu} - \frac{m^2}{2}A_\mu A^\mu - \frac{1}{2\xi}(\partial_\mu A^\mu)^2 - \frac{1}{2}\partial_\mu\sigma\partial^\mu\sigma - \xi\frac{m^2}{2}\sigma^2 + gA_\mu J^\mu, \tag{5.8}$$

where we have added also an interaction term which contains the coupling of A_μ with fermions via a conserved vector current, $\partial_\mu J^\mu = 0$. Here the fields σ and A_μ are decoupled and renormalizability and unitary are manifest.

5.1 The Stueckelberg Extensions of the SM and the MSSM

As mentioned in the previous section, the Stueckelberg mechanism allows for mass generation for a $U(1)$ vector field without the benefit of a Higgs mechanism. Specifically the models of Ref. [167, 168, 169], [170, 171], [172, 173, 174, 175] are based on the $U(1)_X$ Stueckelberg extensions of the Standard Model (SM), i.e., on the gauge group, $SU(3)_C \times SU(2)_L \times U(1)_Y \times U(1)_X$. This extension of the SM involves a non-trivial mixing of the $U(1)_Y$ hypercharge gauge field B^μ and the $U(1)_X$ Stueckelberg field C^μ. The Stueckelberg field C^μ has no couplings with the visible sector fields, while it may couple with a hidden sector, and thus the physical Z' gauge boson connects with the visible sector only via mixing with the gauge bosons of the physical sector. These mixings, however, must be small because of the LEP electroweak constraints[170] and consequently the couplings of the Z' boson to the visible matter fields are extra weak, leading to a very narrow Z' resonance when the decays are dominantly into visible matter. The width of such a boson could be as low as a few MeV or even lower and lie in the sub-MeV range [171]. Indeed such Stueckelberg mass mixings are generic to string and brane constructions [176, 132, 40, 177, 178], (see also [179] for a recent analysis in the context of electric/magnetic duality and generalized Chern-Simons terms). It is noted here that in the particular string scenario of [180] one finds kinetic mixing and Stueckelberg mass mixings terms of the form constructed in [174]. This leads to rather different phenomenology from earlier work which considered kinetic mixing [181, 182]. In what follows we discuss several aspects of the Stueckelberg Extensions of the Standard Model and the MSSM [167, 168]. Recent reviews on the above subject may be found in [183, 184].

Chapter 6

StMSSM : and the XWIMP Stino

Here we investigate a new type of dark matter with couplings to ordinary matter naturally suppressed by at least 1 order of magnitude compared to weak interactions. The eXtra-weakly interacting massive particles of this type, XWIMPs, can satisfy the WMAP relic density constraints due to co-annihilation if their masses are close to that of the lightest state of the MSSM. Considered is an extended minimal supergravity model consistent with the WMAP3 constraints on XWIMPs. As an example, for an explicit model we show that such a form of dark matter can arise in certain Z' extensions of the MSSM. Specifically we consider an Abelian extension with spontaneous gauge symmetry breaking via Fayet-Iliopoulos D-terms in the hidden sector. In a certain limit the model reduces to the Stueckelberg extension of the MSSM.

6.1 The Connector Sector

An interesting possibility arises in that dark matter can originate from a hidden sector. As already discussed, in SUGRA unified models and in string and in brane models, a hidden sector exists which contains fields which are singlets of the Standard Model

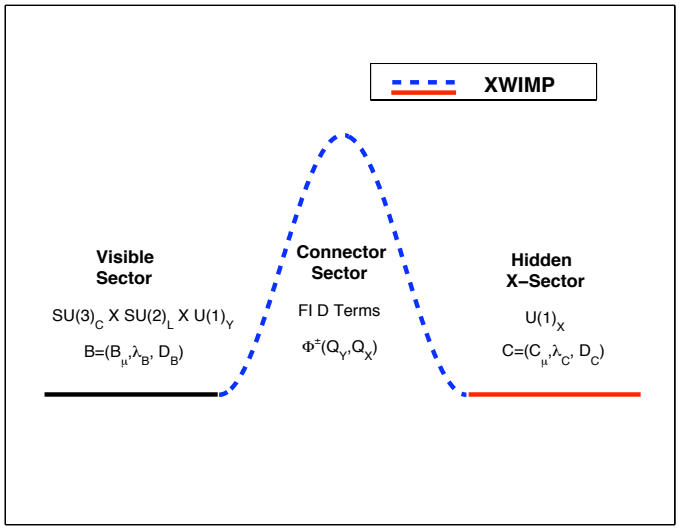

Figure 6.1: The generation of the extra-weakly interacting massive particles. An XWIMP is a linear combination of fields in the hidden sector and in the connector sector, and its interactions with the MSSM particles are suppressed. We note this figure appears in [172].

gauge group. As such, it is then interesting to investigate if the hidden sector can provide us with the relevant candidate for dark matter which produces relic density within the WMAP bounds.

Suppose there is dark matter whose interactions with quarks and leptons are weaker than weak, or extra-weak. How can such dark matter arise? Such extra-weak dark matter can arise when one has two sectors: a physical sector where MSSM fields reside and a hidden sector. The hidden sector fields do not carry MSSM quantum numbers and the physical sector fields do not carry the quantum numbers of fields in the hidden sector. Thus the sectors do not have a direct communication. If, however, one introduces a connector sector which carries dual quantum numbers and interacts with the physical sector fields as well as with the hidden sector fields then the sectors can communicate [172]. The basic elements of the models we discuss are exhibited in Fig.(6.1) and involve three sectors: (*i*) a visible sector where the fields of the SM or the MSSM reside, (*ii*) a hidden sector which is neutral under the SM gauge group, and (*iii*) a third sector [185] which transforms non-trivially under the SM and the

hidden sector gauge symmetry. Aside from gravity, the fields of the visible sector and the hidden sector communicate only via this third sector which we therefore call the "connector sector". Interactions with hidden particles can of course modify predictions of the SM and are thus highly constrained by the precision data from the LEP and the Tevatron experiments (see [170]).

In the following, we construct explicit simple models where the gauge group in the hidden sector is just an Abelian $U(1)_X$ with spontaneous breaking and a massive Z' gauge boson. Such Abelian extensions of the MSSM occur in a wide class of models including grand unified models, string and brane models. The explicit elements of our first example are as follows:

1. The visible sector contains gauge, matter and Higgs superfields of the MSSM charged under the gauge group $SU(3)_C \times SU(2)_L \times U(1)_Y$, but neutral under $U(1)_X$.

2. The hidden sector contains the gauge superfield for $U(1)_X$, the components of which are neutral under the Standard Model gauge group.

3. The connector sector contains chiral fields $\phi^{\pm}$ with charges $\pm Q_X$ under $U(1)_X$ and $\pm Y_\phi$ under $U(1)_Y$. They thus carry *dual* quantum numbers. The fields in the visible and in the hidden sectors can communicate only via couplings with these connector fields.

Spontaneous breaking of the $U(1)_X$ generates a mixing between the hidden and the visible fields. We will implement this breaking via Fayet-Iliopoulos D-terms (see the second Ref of [1]). The parameters that measure the mixing are highly suppressed because of the precision constraints on the electroweak predictions. Their smallness is responsible for the extra-weak interactions of the hidden and the connector fields with the fields in the MSSM.

6.2 Extra-weak Dark Matter in Z' Models

To start with, we introduce a class of extensions of the MSSM where a natural mixing of the neutral MSSM fields with fields from the hidden sector appears via an off-diagonal mass matrices. We also discuss other possibilities to facilitate a mixing of a very similar type.

6.2.1 Broken $U(1)_X$ with Fayet-Iliopoulos Terms

A $U(1)_X$ extension of the MSSM with a Fayet-Iliopoulos (FI) D-term can lead in a natural manner to extra-weakly interacting dark matter constrained by LEP and Tevatron data. The features of our model were already explained in the previous section. The full gauge symmetry of the model is $SU(3)_C \times SU(2)_L \times U(1)_Y \times U(1)_X$. It differs from previous formulations in that a FI D-term breaks the extra $U(1)$ gauge symmetry instead of an F-term. The Abelian vector fields consist of the $U(1)_Y$ vector multiplet (B_μ, λ_B, D_B) and the $U(1)_X$ vector multiplet (C_μ, λ_C, D_C) with gauge kinetic Lagrangian given by

$$\mathcal{L}_{\rm gkin} = -\frac{1}{4}B_{\mu\nu}B^{\mu\nu} - i\lambda_B\sigma^\mu\partial_\mu\bar{\lambda}_B + \frac{1}{2}D_B^2 - \frac{1}{4}C_{\mu\nu}C^{\mu\nu} - i\lambda_C\sigma^\mu\partial_\mu\bar{\lambda}_C + \frac{1}{2}D_C^2 \ . \quad (6.1)$$

The superfields $\Phi^\pm$ with components $(\phi^\pm, f^\pm, F^\pm)$ are described by

$$\begin{aligned}\mathcal{L}_\Phi &= -|D_\mu\phi^+|^2 - if^+\sigma^\mu D_\mu\bar{f}^+ - \sqrt{2}\left(ig_X Q_X\phi^+\bar{f}^+\bar{\lambda}_C + ig_Y Y_\phi\phi^+\bar{f}^+\bar{\lambda}_B + \text{h.c.}\right) \\ &\quad + g_X D_C(\bar{\phi}^+ Q_X\phi^+) + g_Y D_B(\bar{\phi}^+ Y_\phi\phi^+) + \{\Phi^+ \to \Phi^-\} \ , \end{aligned} \quad (6.2)$$

where we do not add any chiral matter in the superpotential and thus $F^{\pm}$ vanishes (this is unlike [186],[187]). The covariant derivatives of the scalars are

$$D_\mu \phi^{\pm} = (\partial_\mu \pm i g_X Q_X C_\mu \pm i g_Y Y_\phi B_\mu)\phi^{\pm} \ . \tag{6.3}$$

Next we add to the mix the FI terms $\mathcal{L}_{\rm FI} = \xi_X D_C + \xi_Y D_B$. Elimination of the D terms gives us the scalar potential[1]

$$V_{\rm FID} = \frac{g_X^2}{2}\Big(Q_X|\phi^+|^2 - Q_X|\phi^-|^2 + \xi_X\Big)^2 + \frac{g_Y^2}{2}\Big(Y_\phi|\phi^+|^2 - Y_\phi|\phi^-|^2 + \xi_Y\Big)^2 \ . \tag{6.4}$$

Minimization of the potential leads to a solution

$$\langle\phi^+\rangle = 0 \ , \quad \langle\phi^-\rangle = \sqrt{\frac{g_X^2\xi_X Q_X + g_Y^2\xi_Y Y_\phi}{g_X^2 Q_X^2 + g_Y^2 Y_\phi^2}} \ . \tag{6.5}$$

We consider the bosonic sector first. We couple the mixed $U(1)_Y \times U(1)_X$ system to the MSSM. We will assume this breaking takes place at a higher scale before the on set of the electroweak symmetry breaking where the MSSM Higgses acquire a VEV. Thus spontaneous breaking of the electroweak symmetry gives rise to the mixing of the neutral gauge fields $(C^\mu, B^\mu, A^{3\mu})$, with $A^{\mu a}$ $(a = 1, 2, 3)$ for the $SU(2)_L$ gauge fields. In this basis the mass matrix in the neutral sector is of the form

$$\begin{bmatrix} M_1^2 & M_1 M_2 & 0 \\ M_1 M_2 & M_2^2 + \frac{1}{4}v^2 g_Y^2 & -\frac{1}{4}v^2 g_2 g_Y \\ 0 & -\frac{1}{4}v^2 g_2 g_Y & \frac{1}{4}v^2 g_2^2 \end{bmatrix} \ . \tag{6.6}$$

[1] Factors of g_i^{-2} have been absorbed into the FID terms.

The parameters M_1, M_2 are defined so that

$$M_1 = \sqrt{2} g_X Q_X \langle \phi^- \rangle \ , \quad M_2 = \sqrt{2} g_Y Y_\phi \langle \phi^- \rangle . \tag{6.7}$$

There is a single massless mode, the photon, and two massive modes the Z and Z'. Since $\langle \phi^+ \rangle = 0$, the superfield components of Φ^+ does not enter in the mixings in the mass matrix for the fields in the hidden sector and the fields in the visible sector, and we do not consider it further. We note in passing that were the spontaneous breaking of the $U(1)_X$ symmetry and of the $SU(2) \times U(1)_Y$ symmetry to take place at the same scale, one would carry out the minimization of the potential involving $\phi^\pm$ and the Higgs fields simultaneously. However, such an analysis does not substantially alter the conclusions of the analysis of this section since the additional corrections from such a minimization are typically small.

We discuss now the effects of mixing of the hidden sector fields and of the connector fields with the fields of the visible sector. In the scalar sector the CP-even component of the complex scalar ϕ^- mixes with the two CP-even Higgs fields of MSSM producing a 3×3 mass matrix similar to the analysis given in Ref. [168, 169]. In the neutral fermionic sector there are two additional mass eigenstates beyond the four neutral fermionic states in the MSSM, $\lambda_Y, \lambda_3, \tilde{H}_1, \tilde{H}_2$. One can reorganize the Weyl spinors in terms of four-component Majorana spinors χ_S (out of f^-) and λ_X (out of λ_C) in a standard way. The 6×6 neutralino mass matrix in the basis

$((\chi_S, \lambda_X); (\lambda_Y, \lambda_3, \tilde{H}_1, \tilde{H}_2))$ reads

$$\begin{bmatrix} 0 & M_1 & M_2 & 0 & 0 & 0 \\ M_1 & \tilde{m}_X & 0 & 0 & 0 & 0 \\ M_2 & 0 & \tilde{m}_1 & 0 & -c_\beta s_W M_0 & s_\beta s_W M_0 \\ 0 & 0 & 0 & \tilde{m}_2 & c_\beta c_W M_0 & -s_\beta c_W M_0 \\ 0 & 0 & -c_\beta s_W M_0 & c_\beta c_W M_0 & 0 & -\mu \\ 0 & 0 & s_\beta s_W M_0 & -s_\beta c_W M_0 & -\mu & 0 \end{bmatrix} . \tag{6.8}$$

Here $\tilde{m}_X$ arises from the soft mass term $-\frac{1}{2}\tilde{m}_X \bar{\lambda}_X \lambda_X$, M_0 is the Z boson mass at the tree level, $c_W = \cos\theta_W$, $s_W = \sin\theta_W$ with θ_W the weak angle, similarly $c_\beta = \cos\beta$, $s_\beta = \sin\beta$, with $\tan\beta = \langle H_2\rangle / \langle H_1\rangle$, and finally μ is the Higgs mixing parameter of the MSSM. The mass eigenstates of the system are defined as the following six Majorana states: $((\xi_1^0, \xi_2^0); (\chi_1^0, \chi_2^0, \chi_3^0, \chi_4^0))$ where χ_a^0 $(a = 1, 2, 3, 4)$ are essentially the four neutralino states of the MSSM and ξ_α^0, $(\alpha = 1, 2)$ are the two additional states composed mostly of the new neutral fermions.

We will discuss in a moment that the current electroweak data puts a stringent bound on $\epsilon = M_2/M_1$ such that $|\epsilon| \ll 1$ [170]. In this limit the masses of ξ_1^0, ξ_2^0 are

$$m_{\xi_1^0} \simeq \sqrt{M_1^2 + \frac{1}{4}\tilde{m}_X^2} - \frac{1}{2}\tilde{m}_X, \quad m_{\xi_2^0} \simeq \sqrt{M_1^2 + \frac{1}{4}\tilde{m}_X^2} + \frac{1}{2}\tilde{m}_X \ . \tag{6.9}$$

For the case when the lightest of the MSSM neutralinos $\chi^0 \equiv \chi_1^0$ is also lighter than $\xi^0 \equiv \xi_1^0$ nothing much changes compared to the pure MSSM. The LSP of the MSSM will still be the LSP of the full system, and the dark matter candidate will be essentially the same as in the MSSM with minor modifications. However, a very different scenario emerges if ξ^0 is lighter than χ^0 and becomes the LSP. The upper bound on ϵ translates to a suppression of the couplings of ξ^0 to MSSM fields relative

to the couplings of χ^0 by a factor of ϵ. Roughly speaking one can treat ξ^0 as a standard LSP χ^0 but with couplings appropriately suppressed by at least an order of magnitude. This is why we call ξ^0 extra-weakly interacting, an XWIMP (it has also been referred to as a Stino).

6.2.2 Stueckelberg Reduction of the $U(1)_X$ Extension

In a certain limit the model of the previous subsection reduces to the Stueckelberg extension of MSSM proposed in [168, 169]. To achieve the reduction we assume as is conventional in the analysis of MSSM that ξ_Y is negligible. We consider now the limit $\langle\phi^-\rangle \to \infty$, $g_X Q_X \to 0$, and $g_Y Y_\phi \to 0$, with M_1 and M_2 fixed. This leads to

$$\frac{1}{2}|D_\mu \phi^-|^2 = \frac{1}{2}(M_1 C_\mu + M_2 B_\mu + \partial_\mu a)^2 + \frac{1}{2}(\partial_\mu \rho)^2 \ , \tag{6.10}$$

where $\phi^- = \rho + ia$. The Lagrangian can be written $\mathcal{L}_\Phi = \mathcal{L}_{\rm St} + \mathcal{L}_{\Phi^+}$, where Φ^+ is now completely decoupled from the vector multiplet and $\mathcal{L}_{\rm St}$ can be written

$$\begin{aligned} \mathcal{L}_{\rm St} &= -\frac{1}{2}(M_1 C_\mu + M_2 B_\mu + \partial_\mu a)^2 - \frac{1}{2}(\partial_\mu \rho)^2 - i\chi\sigma^\mu \partial_\mu \bar{\chi} \\ &\quad + \rho(M_1 D_C + M_2 D_B) + [\chi(M_1 \lambda_C + M_2 \lambda_B) + h.c.] \ . \end{aligned} \tag{6.11}$$

This arises from the following density in superfield notation up to arbitrary phases

$$\mathcal{L}_{\rm St} = \int d^2\theta d^2\bar{\theta} \ (M_1 C + M_2 B + S + \bar{S})^2 \ , \tag{6.12}$$

where C and B are gauge supermultiplets and S a chiral supermultiplet. With the above one then has exactly the Stueckelberg extension of the MSSM [168]. To obtain the supersymmetric Stueckelberg extension we consider the Stueckelberg chiral multiplet $S = (\rho + i\sigma, \chi, F_S)$ along with the vector superfield multiplets for the $U(1)_Y$

denoted by $B = (B_\mu, \lambda_B, D_B)$ and for the $U(1)_X$ denoted by $C = (C_\mu, \lambda_C, D_C)$. Under $U(1)_Y$ and $U(1)_X$ the supersymmetrized gauge transformations are then given by: $\delta_Y(C, B, S) = (0, \Lambda_Y + \bar{\Lambda}_Y, -M_2\Lambda_Y)$ and $\delta_X(C, B, S) = (\Lambda_X + \bar{\Lambda}_X, 0, -M_1\Lambda_X)$. Expanding the fields in the component form, in the Wess-Zumino gauge, we have for the vector superfield(s), denoted here each by $V = (C, B)$,

$$V = -\theta\sigma^\mu\bar{\theta}V_\mu + i\theta\theta\bar{\theta}\bar{\lambda}_V - i\bar{\theta}\bar{\theta}\theta\lambda_V + \frac{1}{2}\theta\theta\bar{\theta}\bar{\theta}D_V \ . \tag{6.13}$$

The superfield S in component notation is given by

$$\begin{aligned} S &= \frac{1}{2}(\rho + i\sigma) + \theta\chi + i\theta\sigma^\mu\bar{\theta}\frac{1}{2}(\partial_\mu\rho + i\partial_\mu\sigma) \\ &\quad + \theta\theta F_S + \frac{i}{2}\theta\theta\bar{\theta}\bar{\sigma}^\mu\partial_\mu\chi + \frac{1}{8}\theta\theta\bar{\theta}\bar{\theta}(\Box\rho + i\Box\sigma) \ , \end{aligned} \tag{6.14}$$

and in the above, the superfield S contains a scalar ρ and an axionic pseudo-scalar σ. With the addition of the soft mass term $-\frac{1}{2}\tilde{m}_X\bar{\lambda}_X\lambda_X$, this system when coupled to the MSSM leads us to the same mass matrix as in Eq.(6.8) as in [169].

6.2.3 Electroweak Constraints on Mixing Parameters

To determine the allowed corridors in ϵ and M_1, we follow a similar approach as in the analysis of Refs. [188, 189] used in constraining the size of extra dimensions. We begin by recalling that in the on-shell scheme the W boson mass including loop corrections is given by [190]

$$M_W^2 = \frac{\pi\alpha}{\sqrt{2}G_F\sin^2\theta_W(1 - \Delta r)}, \tag{6.15}$$

where the Fermi constant G_F and the fine structure constant α (at $Q^2 = 0$) are known to a high degree of accuracy. The quantity Δr is the radiative correction and

is determined so that $\Delta r = 0.0363 \pm 0.0019$ [191], where the uncertainty comes from error in the top mass and from the error in $\alpha(M_Z^2)$. Now since in the on-shell scheme $\sin^2\theta_W = (1 - M_W^2/M_Z^2)$ one may use Eq. (6.15) and the current experimental value of $M_W = 80.425 \pm 0.034$ GeV [191] to make a prediction of M_Z. Such a prediction within SM is in excellent agreement with the current experimental value of $M_Z = 91.1876 \pm 0.0021$ GeV. Thus the above analysis requires that the effects of the Stueckelberg extension on the Z mass must be such that they lie in the error corridor of the SM prediction. We now calculate the error δM_Z in the SM prediction of M_Z in order to limit ϵ. From Eq. (6.15) we find that $\delta \equiv \delta M_Z/M_Z|_{SM}$ is given by

$$\delta = \sqrt{\left(\frac{1 - 2\sin^2\theta_W}{\cos^3\theta_W}\frac{\delta M_W}{M_Z}\right)^2 + \frac{\tan^4\theta_W(\delta\Delta r)^2}{4(1-\Delta r)^2}}. \tag{6.16}$$

The Stueckelberg correction to the Z mass in the region $M_1^2 \gg M_Z^2$ is given by $|\Delta M_Z/M_Z| \sim \frac{1}{2}\sin^2\theta_W(1-M_Z^2/M_1^2)^{-1}\epsilon^2$. Equating this shift to the result of Eq.(6.16) one finds an upper bound on ϵ relevant for TeV scale physics

$$|\epsilon| \lesssim 0.061\sqrt{1-(M_Z/M_1)^2}. \tag{6.17}$$

We note this constraint was first derived in [170] and a very similar constraint appears in the analysis of Ref. [192]. A more detailed analysis of electroweak constraints due to the presence of the heavy vector boson will be presented in Ch.(9).

6.2.4 Abelian Extension with Off-Diagonal Kinetic Terms

There is a well known example of an Abelian extension of the SM with a mixing between the visible and the hidden sector arising from an off-diagonal kinetic mixings with two U(1)s [181]. The hidden sector in this model has been dubbed the shadow

sector, the extra gauge factor denoted $U(1)_S$. Specifically we couple this type of kinetic mixing to the SM and obtain for the action $\mathcal{L} = \mathcal{L}_{\rm SM} + \Delta\mathcal{L}$, where

$$\Delta\mathcal{L} = -\frac{1}{4}C^{\mu\nu}C_{\mu\nu} - \frac{\delta}{2}B^{\mu\nu}C_{\mu\nu} - |D_\mu\phi|^2 - V(\phi,\phi_{\rm SM}) \ . \tag{6.18}$$

Here C^μ is gauge field for the $U(1)_S$, ϕ is the Higgs charged under $U(1)_S$ giving mass to C^μ, and $\phi_{\rm SM}$ is the Standard Model Higgs. The kinetic terms of Eq.(6.18) can be diagonalized by the transformation

$$\begin{pmatrix} B^\mu \\ C^\mu \end{pmatrix} = \begin{pmatrix} 1 & -s_\delta \\ 0 & c_\delta \end{pmatrix} \begin{pmatrix} B^{\mu'} \\ C^{\mu'} \end{pmatrix} \ , \tag{6.19}$$

where $c_\delta = 1/(1-\delta^2)^{1/2}$, $s_\delta = \delta/(1-\delta^2)^{1/2}$. As in the analysis of Refs. [167, 169, 170, 171] the mixing parameter δ is small [181, 193, 192]. After spontaneous breaking this type of model also leads to a massless photon, and two massive vector boson modes.

To supersymmetrize the model we write the Lagrangian for the extended theory $\mathcal{L} = \mathcal{L}_{\rm MSSM} + \Delta\mathcal{L}$. In the pure gauge sector of the theory one has

$$\begin{aligned} \Delta\mathcal{L}_{\rm gkin} &= -\frac{1}{4}C^{\mu\nu}C_{\mu\nu} - i\lambda_C\sigma^\mu\partial_\mu\bar{\lambda}_C + \frac{1}{2}D_C^2 \\ &\quad -\frac{\delta}{2}C^{\mu\nu}B_{\mu\nu} - i\delta(\lambda_C\sigma^\mu\partial_\mu\bar{\lambda}_B + \lambda_B\sigma^\mu\partial_\mu\bar{\lambda}_C) + \delta D_B D_C \ . \end{aligned} \tag{6.20}$$

One can give a mass to the C_μ by a Stueckelberg mechanism without mixing with the hypercharge as in the analysis of Ref.[168]. Thus we add a term

$$\Delta\mathcal{L}_{\rm St} = \int d\theta^2 d\bar{\theta}^2 (MC + S + \bar{S})^2 \ , \tag{6.21}$$

where C is the gauge multiplet for the extra $U(1)_S$ and S a chiral superfield. Everything works very much the same way as in the standard Stueckelberg extension. After spontaneous breaking of the electroweak symmetry the neutralino mass matrix in the basis $((\psi_S, \lambda'_X); (\lambda'_Y, \lambda_3, \tilde{H}_1, \tilde{H}_2))$, obtained after rotating the Majorana fermions by the use of (6.19), is

$$\begin{bmatrix} 0 & Mc_\delta & 0 & 0 & 0 & 0 \\ Mc_\delta & \tilde{m}_X c_\delta^2 + \tilde{m}_1 s_\delta^2 & -\tilde{m}_1 s_\delta & 0 & s_\delta c_\beta s_W M_0 & -s_\delta s_\beta s_W M_0 \\ 0 & -\tilde{m}_1 s_\delta & \tilde{m}_1 & 0 & -c_\beta s_W M_0 & s_\beta s_W M_0 \\ 0 & 0 & 0 & \tilde{m}_2 & c_\beta c_W M_0 & -s_\beta c_W M_0 \\ 0 & s_\delta c_\beta s_W M_0 & -c_\beta s_W M_0 & c_\beta c_W M_0 & 0 & -\mu \\ 0 & -s_\delta s_\beta s_W M_0 & s_\beta s_W M_0 & -s_\beta c_W M_0 & -\mu & 0 \end{bmatrix} . \tag{6.22}$$

The structure of the neutralino mass matrix in Eq.(6.22) is significantly different from that of Eq.(6.8). Similar to the analysis of already given, in the limit $s_\delta \to 0$ the states ψ_S and λ'_X decouple from the rest of the neutralinos. As before we label these two ξ_1^0, ξ_2^0 with masses given by

$$m_{\xi_1^0} \simeq \sqrt{M^2 + \frac{1}{4}\tilde{m}_X^2} - \frac{1}{2}\tilde{m}_X \ , \quad m_{\xi_2^0} \simeq \sqrt{M^2 + \frac{1}{4}\tilde{m}_X^2} + \frac{1}{2}\tilde{m}_X \ . \tag{6.23}$$

Diagonalizing Eq.(6.22) one obtains six mass eigenstates $((\xi_1^0, \xi_2^0); (\chi_1^0, \chi_2^0, \chi_4^0, \chi_4^0))$. The situation is very similar to the models discussed in previous subsections with off-diagonal mass matrix. Thus we can summarize that the supersymmetrized model with kinetic energy mixing can also lead to an XWIMP that becomes the XLSP with extra-weak coupling to the Standard Model.

One can use a unified notation labeling the eXtra-weakly interacting particle as an arbitrary XWIMP denoting any class of model with these characteristics. The

small mixing parameter will be called ϵ in any case and the analysis of relic density given below applies to all such models with XWIMPs.

6.3 Dark Matter from XWIMPs: Relic Density and WMAP Data

Since the interactions of XWIMPs with matter are extra-weak the annihilation of XWIMPs in general is much less efficient in the early universe. Thus it requires some care to ascertain if a reduction of the primordial density is possible in sufficient amounts to satisfy the current relic density constraints. However, the condition of thermal equilibrium are still satisfied for XWIMPs as long as their interactions are only suppressed by few orders of magnitude, say one or two. This requires that interaction rate Γ is greater than the expansion rate of the universe, $\Gamma \geq H$ with $H = T^2/M_{\rm Pl}$. For the system at hand, consisting of weakly and extra-weakly interacting massive particles (WIMPS and XWIMPs) the condition of thermal equilibrium is indeed satisfied. The XWIMPs will only slightly earlier fall out of equilibrium but both types of species will be produced thermally. This is in contrast to models where the couplings of dark matter candidates are only of gravitational strength or suppressed in similar ways.

While the annihilation of XWIMPs alone cannot be sufficient to deplete their density efficiently such reductions may be possible with co-annihilation [194]. In general, co-annihilation could involve all the neutralinos as well as squarks and sleptons in processes of the type

$$\chi_i^0 + \chi_j^0 \quad \rightarrow \quad f\bar{f}, WW, ZZ, Wh, \cdots \quad , \tag{6.24}$$

where $\chi_i^0 = (\xi_\alpha^0, \chi_a^0)$. Here we explain how this can potentially lead to sufficient annihilation of XWIMPs.

Relic Density Analysis for XWIMPs

The naive expectation is that XWIMPs would not be able to annihilate in sufficient numbers to satisfy the current relic density constraints. An exception to this expectation is the situation of co-annihilation [194] that can drastically change the picture. It can contribute in a very significant way to the annihilation process. Let us consider the co-annihilation of a XWIMP ξ^0 and a WIMP χ^0 via the following set of processes

$$\xi^0 + \xi^0 \ \ \rightarrow X \ , \quad \xi^0 + \chi^0 \rightarrow X' \ , \quad \chi^0 + \chi^0 \ \ \rightarrow X'' \tag{6.25}$$

where $\{X\}$ etc denote the Standard Model final states. The effective cross section in this case is [172]

$$\sigma_{\text{eff}} = \sigma_{\chi^0\chi^0} \frac{1}{(1+Q)^2} (Q + \frac{\sigma_{\xi^0\chi^0}}{\sigma_{\chi^0\chi^0}})^2 \ , \tag{6.26}$$

where

$$Q = \frac{g_{\chi^0}}{g_{\xi^0}} (1+\Delta)^{\frac{3}{2}} e^{-x_f \Delta} \ . \tag{6.27}$$

Here g is the degeneracy for the corresponding particle and $\Delta = (m_{\chi^0} - m_{\xi^0})/m_{\xi^0}$. For the case at hand, the ratio $\sigma_{\xi^0\chi^0}/\sigma_{\chi^0\chi^0} \sim \mathcal{O}(\epsilon^2) \ll 1$. Thus if the mass gap between ξ^0 and χ^0 is large so that $x_f\Delta \gg 1$, then σ_{eff} is much smaller than the typical WIMP cross-section and the XWIMPs cannot annihilate in an efficient manner to satisfy the relic density constraints.

If the mass gap between the XWIMP and WIMP is small and the XWIMP is still lighter than the WIMP we have the case of co-annihilation. Let us look at a

parameter choice with $Q \sim O(1)$ and $Q \gg \sigma_{\xi^0\chi^0}/\sigma_{\chi^0\chi^0}$. We can write $\sigma_{\rm eff}$ in the form [172] $\sigma_{\rm eff} \simeq \sigma_{\chi^0\chi^0}(Q/(1+Q))^2$ which is easily extended under the same approximations including co-annihilations involving additional MSSM channels. The relation becomes modified so that $\sigma_{\chi^0\chi^0}$ is replaced by $\sigma_{\rm eff}(MSSM)$ and Q is defined so that $Q = \sum_{i=2}^{N} Q_i$ where $Q_i = (g_i/g_1)(1+\Delta_i)^{3/2} e^{-x_f \Delta_i}$. When $Q \sim \mathcal{O}(1)$ the XWIMP relic density is just a modification of the WIMP relic density modified only by the multiplicative factor $(Q/(1+Q))^2$. It is then possible to satisfy the relic density constraints much in the same way as one does for the LSP of MSSM[2]. Nevertheless, the couplings of ξ^0 with quarks and leptons are suppressed by a factor of ϵ. Thus cross-sections for the direct detection of dark matter will be suppressed by powers of the mixing parameter, making the direct detection of the extra-weak dark matter more difficult. However, ξ^0 will do as well as χ^0 for the seeding of the galaxies.

WMAP Constraints on XWIMPs

The specific framework we consider is a Abelian extension of mSUGRA with a $U(1)_X$. This means, in the MSSM we use the mSUGRA framework with the minimal set of characteristic parameters for the soft breaking and the co-annihilation parameters Δ as determined by $Q_{\rm eff}$. This is our extended mSUGRA model. We now discuss the details of the analysis. In Fig.(6.3) we display the relic density constraints on the XWIMPs in the $m_0 - m_{1/2}$ plane for the case $\tan\beta = 50$ consistent with all experimental constraints. The black region satisfies the relic density constraints which lie within 1σ corridor of the central value , while the shaded (colored) regions are eliminated due to other constraints. The other constraints arise mainly from the lower limit on the chargino mass and the $b \to s\gamma$ branching ratio. The bound on the Higgs mass is also shown but only a small additional region of the parameter space is eliminated. The analysis shows that the relic density is satisfied in both a low m_0 region,

[2]We note in passing that Ref. [195] subsequently found quite a similar result.

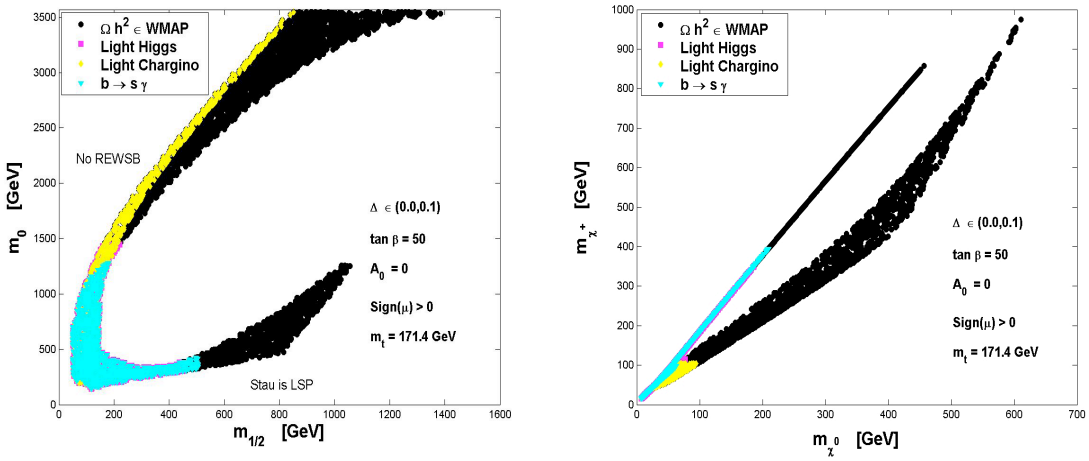

Figure 6.2: The allowed parameter space (black) in the $m_0 - m_{1/2}$ plane, under the 1σ WMAP3 constraint in extended mSUGRA for the case $A_0 = 0$, $\tan\beta = 50$, sign$(\mu > 0)$, $m_t = 171.4$ GeV, $m_{1/2} \in (0, 1.5)$TeV and $m_0 \in (0, 3.5)$TeV, and Δ in the range (0.0, 0.1). The figure to the right exhibits the breakdown of scaling and its breakdown as discussed in the text. (From [172].)

where one has typically co-annihilation between the lightest neutralino of the MSSM and the stau, and a high m_0 region, which is characteristically the hyperbolic branch (HB) of radiative breaking of the electroweak symmetry as discussed earlier, where the LSP and the next to lowest supersymmetric particle (NLSP) become degenerate and are mostly Higgsino like. We also show the parameter space in the $m_{\chi^+} - m_{\chi^0}$ plane. These plots display the regions where scaling holds or breaks down which are also good indicators of the gaugino vs. Higgsino composition of χ^0 (the LSP of the MSSM). Thus in the $m_{\chi^+} - m_{\chi^0}$ plot, the model points on the straight line boundary satisfy the scaling phenomenon, where $m_{\chi^0} \simeq 0.5 m_{1/2}$. Here m_{χ^0} is mostly a Bino. More generally, scaling [196] gives $m_{\tilde{g}} : m_{\chi_1^+} : m_{\chi^0} \simeq (6-7) : 2 : 1$. On the other hand, when scaling is violated one has a large Higgsino component, and this indeed typically arises from the HB. In Fig.(6.3) we exhibit the allowed parameter space in the $m_{\tilde{g}} - m_{\chi^+}$ plane. On the lower straight line along the diagonal χ^0 is bino-like and the scaling relation $m_{\tilde{g}} : m_{\chi^0} = (6-7) : 1$ is satisfied. Above this region χ^0 has a

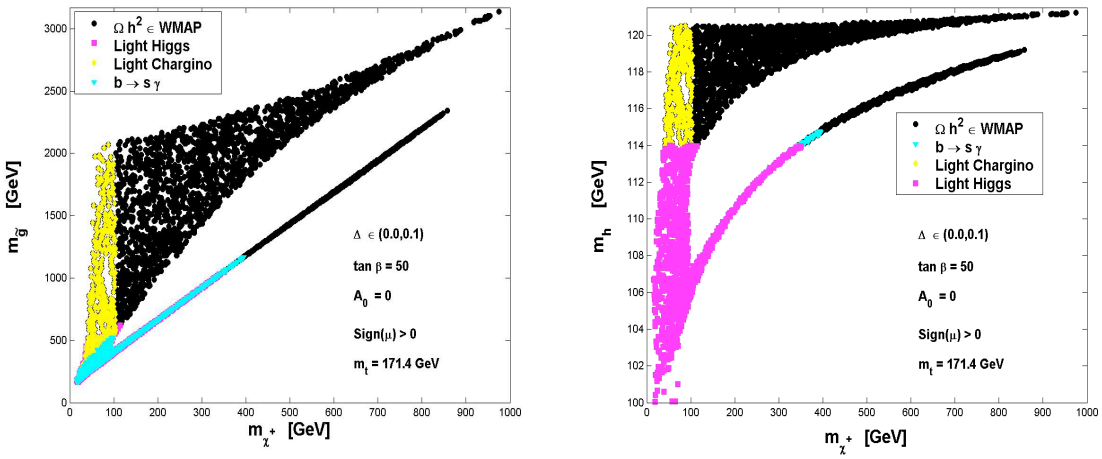

Figure 6.3: Left Panel:Violation of scaling in the gluino chargino plane, Right Panel: the Higgs Boson Branches. (From [172].)

significant Higgsino component, and scaling is violated. The analysis shows that the permissible mass range for the gluino $\widetilde{g}$ is rather wide, while for the Higgs there is a narrow window. Typically, its mass has to lie within the corridor from the lower limit of 114 GeV (when this limit is imposed) up to about 125 GeV and there are 2 distinct branches for the light CP even Higgs. A similar situation has been seen in mSUGRA in [143].

In the calculation of the relic density, we find in general good agreement between DarkSUSY and `micrOMEGAS` (up to about 15%) for values of $\tan\beta$ in the range $(10-40)$. The main result is that the WMAP3 constraints are satisfied by XWIMPs for a wide range of $\tan\beta$, even though the allowed parameter space consistent with all constraints does depend on the value of $\tan\beta$ and more so, sensitively on the value of the top mass. We add a comment regarding the impact of experimental error bars on the top mass under the constraints of the electroweak symmetry breaking. The region in the parameter space of mSUGRA consistent with electroweak symmetry breaking depends very sensitively on the mass of the top quark, a phenomena which has been known for some time and which affects the relic density [197]. We emphasize

that the sensitivity of the relic density arises as the sparticle spectrum in SUGRA unified models, where the sparticle spectrum arises as a consequence of REWSB, is very sensitive to the top mass. This can be seen, for example, in the first paper of Ref.[197] where it is shown that the stop mass can turn tachyonic with variations in the top mass under constraints of REWSB. However, in MSSM scenarios where one can fix the sparticle spectrum and vary the top mass, the relic density is not sensitive to variations in the top mass. In contrast, in the current analysis the sensitivities to the top mass arise since we are using the framework of SUGRA unification where the spectrum is computed via REWSB. The recent more accurate determinations of the top mass have now very much reduced the error. Interestingly, one finds that even a 1σ variation with reduced error bars generates very significant changes in the relic density. Specifically, a lower top mass implies a larger portion in parameter space consistent with the constraints. For further details see [172].

6.4 Summary

We have introduced a new dark matter candidate whose interactions with Standard Model matter are extra-weak, weaker than weak interactions by at least one order of magnitude. Extra-weakly interacting particles can arise in a wide range of models, Z' extensions of the MSSM with extended Higgs sectors, in the Stueckelberg extension, in extensions of the MSSM with off-diagonal gauge boson kinetic terms, and possibly many other realization of small mixing between visible and hidden sector fields. The new XWIMPs are good candidates for dark matter if they become the LSP of the full system, in spite of the extra-weak interactions with the MSSM, as they can satisfy the relic density constraints consistent with the WMAP data via co-annihilation. A direct observation of XWIMPs in dark matter detectors will be more difficult. However, indirect tests of the model are possible and should be investigated.

Chapter 7

Fermilab Probes of a Narrow Z'

We begin by discussing the Stueckelberg extension of the Standard Model [167] based on the gauge group $SU(3)_C \times SU(2)_L \times U(1)_Y \times U(1)_X$. The effective Lagrangian arises from coupling the Stueckelberg sector to the SM, i.e., $\mathcal{L}_{\rm StSM} = \mathcal{L}_{\rm St} + \mathcal{L}_{\rm SM}$, where

$$\mathcal{L}_{\rm St} = -\frac{1}{4} C_{\mu\nu} C^{\mu\nu} + g_X C_\mu J_X^\mu - \frac{1}{2}(\partial_\mu \sigma + M_1 C_\mu + M_2 B_\mu)^2 \ . \tag{7.1}$$

In the above, J_X^μ is a conserved vector current, C^μ is a Stueckelberg field and B_μ is the hypercharge vector boson. It is easily checked that the above Lagrangian is invariant under the following transformations : $\delta_Y(C_\mu, B_\mu, \sigma) = (0, \partial_\mu \lambda_Y, -M_2 \lambda_Y)$ and $\delta_X(C_\mu, B_\mu, \sigma) = (\partial_\mu \lambda_X, 0, -M_1 \lambda_X)$. The two Abelian gauge bosons can be decoupled from σ by the addition of gauge fixing terms as before. Additionally, of course, one has to add the standard gauge fixing terms for the SM gauge bosons to decouple from the Higgs. After electroweak symmetry breaking the mass terms for the neutral

vector bosons take the form

$$\mathcal{L}_{\rm Mass} = -\frac{1}{2}\mathcal{V}_\mu^T M_{\rm St}^2 \mathcal{V}^\mu, \qquad M_{\rm St}^2 = \begin{pmatrix} M_1^2 & M_1 M_2 & 0 \\ M_1 M_2 & M_2^2 + \frac{1}{4}v^2 g_Y^2 & -\frac{1}{4}v^2 g_2 g_Y \\ 0 & -\frac{1}{4}v^2 g_2 g_Y & \frac{1}{4}v^2 g_2^2 \end{pmatrix}, \quad (7.2)$$

where $\mathcal{V}_\mu^T = (C_\mu, B_\mu, A_\mu^3)$, v is the VEV of the Higgs field, g_2 is the bare $SU(2)$ gauge coupling and g_Y is the bare $U(1)_Y$ gauge coupling. Note this mass matrix is precisely that of Eq.(6.6). The mass squared matrix, being real and symmetric, can be diagonalized by an orthogonal transformation $\mathcal{V}_\mu = R\mathcal{E}_\mu$. with $\mathcal{E}_\mu^T = (Z'_\mu, Z_\mu, A_\mu^\gamma)$ so that $R^T M_{\rm St}^2 R = M_{\rm St-diag}^2$. The zero eigen-mode is manifest and is to be associated with the massless photon state. In the above model, the photon field is a linear combination of the set of three fields $(C^\mu, B^\mu, A^{3\mu})$. In the limit $\epsilon \equiv M_2 \ll M_1 \to 0$, the Stueckelberg sector decouples from the Standard Model and the tree level expressions for the Standard Model Z boson mass is recovered, while the Z' mass limits to M_1 which is the overall scale of new physics in the StSM. The orthogonal matrix R is easily formed from the eigen-vectors associated with the diagonalization. A convenient parametrization is

$$R = \begin{pmatrix} c_\psi c_\phi - s_\theta s_\phi s_\psi & s_\psi c_\phi + s_\theta s_\phi c_\psi & -c_\theta s_\phi \\ c_\psi s_\phi + s_\theta c_\phi s_\psi & s_\psi s_\phi - s_\theta c_\phi c_\psi & c_\theta c_\phi \\ -c_\theta s_\psi & c_\theta c_\psi & s_\theta \end{pmatrix}, \quad (7.3)$$

where the angles are defined so that

$$\tan\theta = \frac{\gamma}{g_2}, \qquad \tan\phi = \epsilon, \qquad \tan 2\psi = \frac{2\sin\theta M_0^2 \epsilon}{M_1^2 - M_0^2 + (M_1^2 + M_0^2 - M_W^2)\epsilon^2}, \quad (7.4)$$

and $M_0 = M_Z(\epsilon = 0) = v\sqrt{g_2^2 + \gamma^2}/2$, $M_W = g_2 v/2$, and $g_Y = \gamma\sqrt{1+\epsilon^2}$, $\gamma \equiv g_Y^{SM}$. The diagonalization leads to the following relation for the electronic charge

$$e = \frac{g_2 g_Y \cos\phi}{\sqrt{g_2^2 + g_Y^2 \cos^2\phi}} = \frac{g_2\gamma}{\sqrt{g_2^2+\gamma^2}}. \tag{7.5}$$

The neutral current interaction with the visible sector fermions is given by

$$\mathcal{L}_{NC} = -\frac{1}{i}\sum_f [\bar{f}_L \gamma^\mu D_\mu f_L + (L \to R)], \tag{7.6}$$

where D_μ is the covariant derivative with respect to $SU(2)_L \times U(1)_Y \times U(1)_X$ however we assume that the visible sector matter, i.e., quarks, leptons and the Higgs, are not charged under $U(1)_X$. Thus the charges of $U(1)_X$ sector satisfy $Q_X|SM>= 0$. The The neutral current interaction leads to

$$\mathcal{L}_{NC} = \frac{\sqrt{g_2^2+\gamma^2}}{2}\bar{f}\gamma^\mu\left[(v_f' - \gamma_5 a_f')Z_\mu' + (v_f - \gamma_5 a_f)Z_\mu\right] f + e\bar{f}\gamma^\mu Q_f A_\mu f, \tag{7.7}$$

where as usual $Q = T_{L,R}^3 + Y_{L,R}/2$, $T_R^3 = 0$. Expressing the tree level interaction in terms of the reduced vector and axial vector couplings we obtain

$$\begin{aligned}
v_f &= \cos\psi\left[(1 - \epsilon\sin\theta\tan\psi)\,T_f^3 - 2\sin^2\theta\,(1 - \epsilon\csc\theta\tan\psi)\,Q_f\right], && (7.8)\\
a_f &= \cos\psi\,[1 - \epsilon\sin\theta\tan\psi]\,T_f^3, && (7.9)\\
v_f' &= -\cos\psi\left[(\tan\psi + \epsilon\sin\theta)\,T_f^3 - 2\sin^2\theta\,(\epsilon\csc\theta + \tan\psi)\,Q_f\right], && (7.10)\\
a_f' &= -\cos\psi\,[\tan\psi + \epsilon\sin\theta]\,T_f^3. && (7.11)
\end{aligned}$$

Note that the decoupling limit is $\epsilon \to 0$ and thus $\cos\psi \to 1, \sin\psi \to 0$ and one obtains the SM expressions for the vector and axial vector couplings.

The partial decay widths of the StSM Z' into SM fermion matter are given by

$$\Gamma(Z' \to f\bar{f}) = \frac{N_f \beta_f}{24\pi} M_{Z'} \Big[\left([C_{f_L}^{Z'}]^2 + [C_{f_R}^{Z'}]^2 \right) \left(1 - \frac{m_f^2}{M_{Z'}^2} \right) + 6\, [C_{f_L}^{Z'}]\, [C_{f_R}^{Z'}] \frac{m_f^2}{M_{Z'}^2} \Big] \quad (7.12)$$

where $\beta_f = (1 - 4m_f^2/M_{Z'}^2)^{1/2}$ and where $v'_f(a'_f) = [C_{f_L}^{Z'} + (-)C_{f_R}^{Z'}]/\sqrt{g_2^2 + \gamma^2}$ and analogously for the Z couplings. The Z' can also decay into hidden matter couplings through J_X. We will first explore the implications of heavy matter in the hidden sector, where the Z prime does not decay to the exotics. We will revisit this issue and explore its implications in Chapter(9.1). Additionally for $M_{Z'} > 2M_W$, the Z' can decay into W^+W^- which is determined by the triple gauge boson vertex,

$$\mathcal{L}_{Z'WW} = i g_2 R_{31} \left[W^+_{\mu\nu} W^{-\mu} Z'^{\nu} + W^-_{\mu\nu} W^{+\nu} Z'^{\mu} + W^{+\mu} W^{-\nu} Z'_{\mu\nu} \right]. \quad (7.13)$$

The W^+W^- decay width is then given by

$$\Gamma(Z' \to W^+W^-) = \theta(M_{Z'} - 2M_W) \frac{g_2^2 R_{31}^2}{192\pi} M_{Z'} \frac{M_{Z'}^4}{M_W^4} \left[1 - 4\frac{M_W^2}{M_{Z'}^2} \right]^{\frac{3}{2}} \times \left[1 + 20\frac{M_W^2}{M_{Z'}^2} + 12\frac{M_W^4}{M_{Z'}^4} \right]. \quad (7.14)$$

The W^+W^- decay mode is suppressed by the small factor R_{31}, the element of the rotation matrix which indicates the mixing between Z' and A^3 gauge bosons. Therefore, the partial width $\Gamma(Z' \to W^+W^-)$ is typically small relative to $\Gamma(Z' \to \sum_i f_i \bar{f}_i)$. To get a feel for the size of the total decay width of Z′ into the visible sector quarks and leptons one may see

$$\Gamma(Z' \to \sum_i f_i \bar{f}_i) \simeq M_{Z'} g_Y^2 \epsilon^2 \times \begin{cases} \frac{103}{288\pi} & \text{for } M_{Z'} < 2m_t \\ \frac{5}{12\pi} & \text{for } M_{Z'} > 2m_t \end{cases}. \quad (7.15)$$

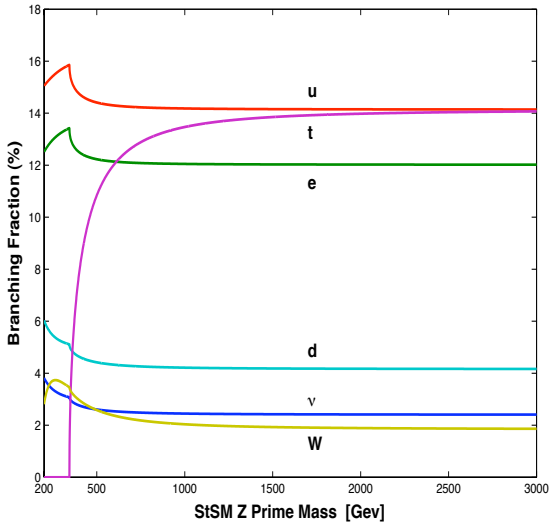

Figure 7.1: The StSM Z' branching ratios into $f\bar{f}$ and W^+W^- final states as a function of the Z' mass with $f = u, t, e, d, \nu$ with $\epsilon = 0.06$. Besides the exceptionally narrow total decay width, the large branching ratio of the StSM Z' into charged leptons further distinguishes this model from other Z' models. [167, 169, 170, 171].

It has already been discussed in the previous chapter that ϵ is severely limited by electroweak constraints which leads to a Stueckelberg Z' resonance with a very narrow decay width. We will carry out a more precise fit to Electroweak data shortly. Thus the Z' decay width lies in the ≤ 100 MeV range with $M_{Z'}$ lying in the several hundred GeV to 1 TeV range. In Fig. (7.1) it is shown that the Z' decays into quarks and leptons will dominate the total Z' decay width, as the W^+W^- decay mode is roughly the same size as one species of $\nu\bar{\nu}$ mode. One may note that the branching ratio of Z' into the charged leptons is relatively large compared to what one has in conventional models. This is due to the StSM Z' couplings being dominated by the hypercharge of the particle in the final state. Thus, the isospin singlet l_R which has a hypercharge $Y = -2$ contributes a significant amount which makes the charged lepton contribution comparable to the up quark contribution overcoming the color factor. The above also indicates that this Z' model can be efficiently tested in an e^+e^- collider with polarized

beams where one could check on the l_R vs l_L couplings. Other examples are provided by the extension $SU(2)_L \times SU(2)_R \times U(1)_{B-L}$ Left-Right (LR) model [198] to give the gauge group $SU(2)_L \times SU(2)_R \times U(1)_{B-L} \times U(1)_X$ (StLR)[170],[171].

7.1 Prospects for the Discovery of a Stueckelberg Z' At Fermilab

7.1.1 Drell-Yan Cross Section for $p\bar{p} \to Z' \to l^+l^-$

Next we discuss the production of the narrow Z' by the Drell-Yan process. For the hadronic process $A + B \to V + X$, and the partonic sub-process $q\bar{q} \to V \to l^+l^-$, the di-lepton doubly differential cross section to next to leading order (NLO) is given by

$$\frac{d^2\sigma_{AB}}{dM^2dz} = K\frac{1}{s}\sum_q \left[\frac{d\sigma^{SM}_{q\bar{q}}}{dz} + \frac{d\sigma^{St-SM}_{q\bar{q}}}{dz} + \frac{d\sigma^{St}_{q\bar{q}}}{dz}\right]\mathcal{W}_{\{AB(q\bar{q})\}}(s, M^2). \tag{7.16}$$

$$\begin{aligned}\mathcal{W}_{\{AB(q\bar{q})\}}(\tau) &= \int_0^1\int_0^1 dxdy\delta(\tau - xy)\mathcal{P}_{\{AB(q\bar{q})\}}(x, y),\\ \mathcal{P}_{\{AB(q\bar{q})\}}(x, y) &= f_{q,A}(x)f_{\bar{q},B}(y) + f_{\bar{q},A}(x)f_{q,B}(y).\end{aligned} \tag{7.17}$$

Here the dimensionless variable $\tau = M^2/s$ relates the invariant mass M of the final state lepton pair to the center of mass energy $\sqrt{s}$ of the colliding hadrons and $z = \cos\theta^*$, where θ^* is the angle between an initial state parton and the final state lepton in the C-M frame of the lepton anti-lepton pair. The term $d\sigma^{SM}/dz$ is the Standard Model contribution, $d\sigma^{St}/dz$ is the contribution from the Stueckelberg sector, and $d\sigma^{St-SM}/dz$ is the interference term between the Standard Model and the Stueckelberg sectors. The parton distribution functions (PDFs) which we denote by

$f_{q,A}(x)$ give the probability that a parton of type q has a fraction x of the total hadron four momentum. The dependence of $f_{q,A}(x)$ on the mass factorization scale $Q = M$ is implicit. For the case of the LHC (discussed in the next chapter) $A = B = p$, and one must note that quite generally that $f_{q,A} = f_{\bar{q},\bar{A}}$ and $f_{\bar{q},A} = f_{q,\bar{A}}$. The Drell-Yan K factor is as discussed in detail in Refs. [199, 200, 201]. The invariant di-lepton differential cross section is at NLO

$$\frac{d\sigma_{AB}}{dM} = K\frac{2M}{s}\sum_{q}\sigma_{q\bar{q}}\left(M^2\right)\mathcal{W}_{\{AB(q\bar{q})\}}(\tau), \tag{7.18}$$

where the partonic cross section, $\sigma_{q\bar{q}}$, is defined by integrating the term in square brackets of Eq. (7.16) over the variable z and is computed in Ref. [169]. While $d\sigma/dM$ is sensitive to the interference term, the integral over dM is not. The full partonic cross section through the $\sigma(Z, Z', \gamma)$ in the massless quark limit is

$$\begin{aligned} 3N_c\sigma_{q\bar{q}} \;=\; & \frac{4\pi\alpha^2 Q_q^2}{M^2} - 2\sqrt{2}\alpha Q_q\frac{G_F M_Z^2(M^2-M_Z^2)v_e v_q}{((M^2-M_Z^2)^2+\Gamma_Z^2 M_Z^2)} + \frac{G_F^2 M_Z^4 M^2(v_e^2+a_e^2)(v_q^2+a_q^2)}{2\pi((M^2-M_Z^2)^2+\Gamma_Z^2 M_Z^2)} \\ & -2\sqrt{2}\alpha Q_q\frac{G_F M_Z^2(M^2-M_{Z'}^2)v'_e v'_q}{((M^2-M_{Z'}^2)^2+\Gamma_{Z'}^2 M_{Z'}^2)} + \frac{G_F^2 M_Z^4 M^2(v_e'^2+a_e'^2)(v_q'^2+a_q'^2)}{2\pi((M^2-M_{Z'}^2)^2+\Gamma_{Z'}^2 M_{Z'}^2)} \\ & +\frac{G_F^2 M_Z^4 M^2(M^2-M_Z^2)(M^2-M_{Z'}^2)(v_q v'_q+a_q a'_q)(v_e v'_e+a_e a'_e)}{\pi((M^2-M_Z^2)^2+\Gamma_Z^2 M_Z^2)((M^2-M_{Z'}^2)^2+\Gamma_{Z'}^2 M_{Z'}^2)}\,. \end{aligned} \tag{7.19}$$

In Fig.(7.2) we give an analysis of the Drell-Yan cross section for the process $p\bar{p} \to Z' \to l^+l^-$ as a function of $M_{Z'}$. The analysis is done at $\sqrt{s} = 1.96$ TeV, using the CTEQ5L [202] PDFs with a flat K factor of 1.3 for the appropriate comparisons with other models and with the CDF [203] and DØ [204] combined data in the di-lepton channel. Remarkably one finds that the Stueckelberg Z' for the case $\epsilon \approx 0.06$ is constrained up to about 375 GeV with the current data (at 95% C.L.) using the $e^+e^- + \gamma\gamma$ channel. This lower limit decreases as ϵ decreases but the current data still constrain the model up to $\epsilon \approx 0.035$. This result is in contrast to the LR, E_6, and

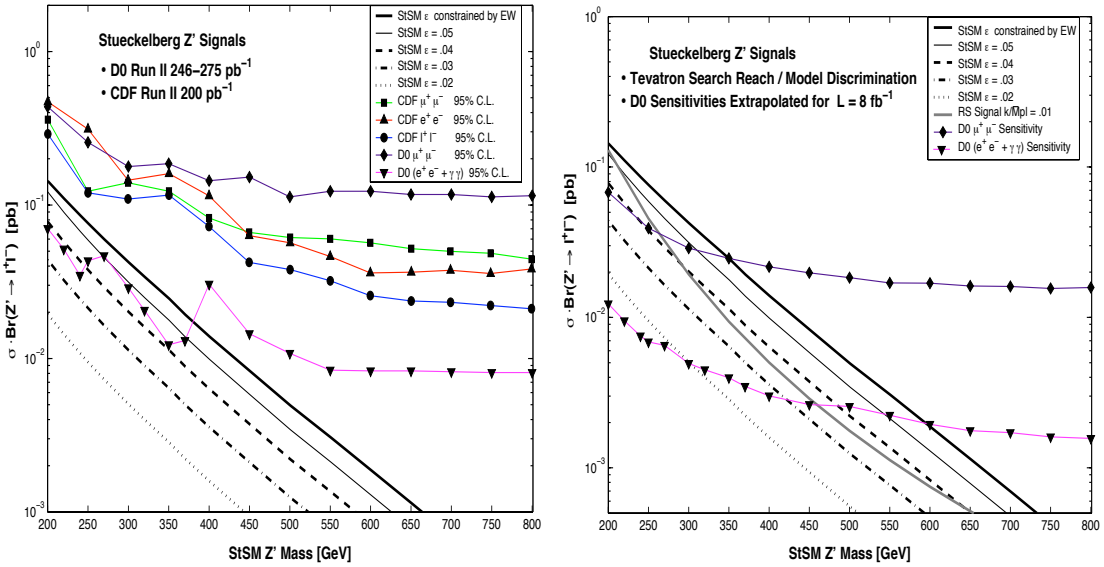

Figure 7.2: (Left): Constraint on the Z' signal in the StSM using the CDF [203] and DØ [204] data (see Fig.(9.3) for an updated comparison of the 2 modes). The data puts a lower limit of about 250 GeV on $M_{Z'}$ for $\epsilon \approx 0.035$ and 375 GeV for $\epsilon \approx 0.06$. (Right): Z' signal in StSM with 8 fb^{-1} of data using an extrapolation of the sensitivity of the DØ [204] detector for the $\mu^+\mu^-$ and $e^+e^- + \gamma\gamma$ modes. The data will put a lower limit of about 600 (300) GeV on $M_{Z'}$ mass for $\epsilon = 0.06(0.02)$. Also plotted for comparison is $\sigma \cdot Br(G \to l^+l^-)$ for the RS case. (From [170].)

to the little Higgs models and other models of wider resonances [205] where the Z' boson has already been eliminated up to $(610-815)$ GeV with the CDF [203] and DØ [204] data. Applying this constraint in this channel is a stronger constraint to place on the model then just using the e^+e^- channel, however probing narrow resonances using both channels are indeed complimentary [206]. We will see shortly that the the stronger constraint imposed is consistent with the more recent e^+e^- limits.

We also give an analysis of the discovery limit for the Stueckelberg Z' with an integrated luminosity of 8 fb^{-1}. Here we have extrapolated the experimental sensitivity curves for the $\mu^+\mu^-$ and for the more sensitive $e^+e^- + \gamma\gamma$ channel downwards by a factor of $1/\sqrt{N}$ where N is the ratio of the expected integrated luminosity to the current integrated luminosity. The analysis shows that a Stueckelberg Z' can be

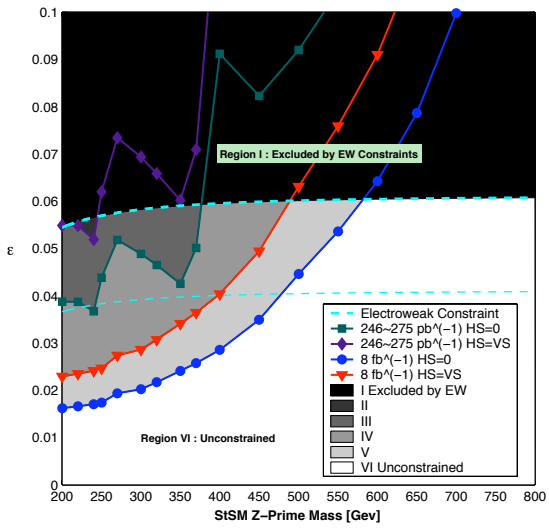

Figure 7.3: (Left) Constraint plots in the $\epsilon - M_{Z'}$ plane utilizing the data from [204] $e^+e^- + \gamma\gamma$ mode with (a) the 246-275 pb^{-1} of data, and (b) 8 fb^{-1} of data where an extrapolation of the sensitivity curve is used. The upper dashed curve is the maximum value of ϵ allowed by Eq. (6) and the lower dashed curve corresponds to $|\Delta\text{Pull}| < 1$. Cases with (without) a hidden sector are shown. Regions II, III, IV, and V are constrained by the conditions given at their respective boundaries. (From [170].)

discovered up to a mass of about 600 GeV and if no effect is seen one can put a lower limit on the Z' mass at about 600 GeV. In Fig.(7.3) we give the constraint plot in the $\epsilon - M_{Z'}$ plane. An analysis including hidden sector with $\Gamma_{\rm HS} = \Gamma_{\rm VS}$ is also exhibited. The constraint plots show that even the hidden sector is beginning to be constrained and these constraints will become even more severe with future data. It is interesting to note that there is a region of the parameter space where a Stueckelberg Z' boson may be mistaken for a narrow resonance of a Randall-Sundrum (RS)[207] warped geometry [1] (the RS model will be discussed in more detail in the next chapter). The overlap of $\sigma \cdot Br(Z' \to l^+l^-)$ and $\sigma \cdot Br(G \to l^+l^-)$ for the RS graviton is shown in Fig.(7.2) for the case $k/\overline{M}_{\rm Pl} = 0.01$ where $\overline{M}_{\rm Pl} = M_{\rm Pl}/\sqrt{8\pi}$ is the reduced Planck mass. However, the constraints from precision electroweak data actually eliminate the

[1] This is now known as RS-1 in the literature.

RS graviton in this case [208, 204]. Thus if a resonance effect is seen in the di-lepton mass range of up to about 600 GeV in the CDF and D0 data at the predicted level, the Stueckelberg Z' would be a prime candidate since the RS graviton possibility is absent in this case.

7.1.2 Further Constraints from CDF and DØ Data

The $C_u - C_d$ parametrization was defined in Ref. [201] and it allows one to use experimental limits set on the di-lepton final state production cross section without making reference to the PDFs; the couplings of a particular model are needed only, if the experimental limits are known. The relation between C_u and C_d is

$$\frac{C_u}{C_d} = \frac{(v_u'^2 + a_u'^2)}{(v_d'^2 + a_d'^2)} \sim \frac{\mathrm{Br}(Z' \to u\bar{u})}{\mathrm{Br}(Z' \to d\bar{d})}. \tag{7.20}$$

where

$$C_q = 2g_M^2 Br(Z' \to l^+ l^-)(a_q'^2 + v_q'^2), \quad q = u, d \tag{7.21}$$

and where $g_M^2 = \sqrt{2} G_F M_Z^2$. Although $C_{(u,d)}$ are functions of ϵ for the StSM, the ratio (in the massless quark limit) is in fact independent of ϵ. In Fig.(7.4) the $C_{u,d}$ plane is shown. For the StSM, in the $C_u - C_d$ plane the values of C_u and C_d lie inside a band. The band structure for StSM arises since the ratio C_u/C_d as given by Eq. (7.20) lies in the range $2.49 \sim 3.37$ for $M_{Z'}$ lying in the range $200 \sim 900$ GeV. Similarly, the C_u and C_d predicted in the $q + xu$ model [201] also lie in a band, while the C_u and C_d for the $B - xL$ model [201] live on a line. In Fig. (7.4) we give a numerical evaluation of the C_u and C_d using the recent CDF data of 819 pb^{-1} in the di-lepton channel [209]. The light straight line corresponds to C_u and C_d in the $B - xL$ model where $C_u = C_d$ (see [201]). The area between the two black straight lines is the region where the $q + xu$ model lies and where $(3 - 2\sqrt{2})C_d < C_u < (3 + 2\sqrt{2})C_d$. The

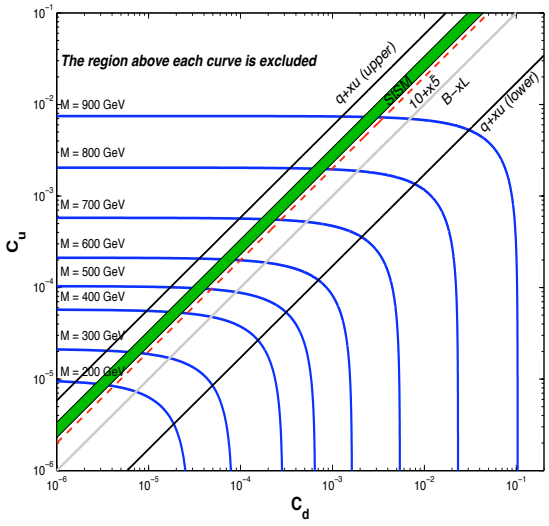

Figure 7.4: Constrained regions in the $C_u - C_d$ plane from the current 95% C.L. limit for $\sigma \cdot \mathrm{Br}(Z' \to l^+l^-)$ given in [209] at 819 pb^{-1} for different Z' masses, labeled as M in the figure. The shaded green band is the region where the StSM model lies and where $2.49C_d < C_u < 3.37C_d$. Note, no constraint on ϵ has been applied here, the LEP comstraint is a stronger constraint than the Tevatron Data at larger Z prime mass (see Fig.(7.3)). (From [171].)

$10 + x\bar{5}$ model is constrained below the dashed red line which corresponds $C_u = 2C_d$. These constraints given in the $C_{u,d}$ plane are consistent with the constraints derived using a smaller data sample of approximately 275 pb^{-1} which, however, uses the more sensitive DØ mode [204] already discussed. In addition to the above, one also has constraints on the parameter space from the non-observation of the Z' from the CDF and DØ data [209, 204, 203, 210]. These constraints were shown to limit values of $(\epsilon, M_{Z'})$ in [170], and discussed here, while still allowing for the possibility of a narrow StSM Z' which could even lie relatively close to the Z-pole. The constraints provided at large mass in Fig.(7.4), for the StSM, correspond to ϵ values already eliminated by LEP constraints (see Fig.(7.3)).

The type of Z' boson that arises from the mixing of the Standard Model with the Stueckelberg sector is very different from the Z' bosons that normally arise in grand

unified models and in previous stringy models such or in the early analyses of Kaluza-Klein excitations of the Z with compactifications of large extra dimensions. The distinguishing features are that the decay width in the present case is exceptionally narrow with width ≤ 100 MeV for $M_{Z'} \leq 1$ TeV as well as its hypercharged enhanced couplings leading to a rather distinct set of branching fractions when compared to the classic Z prime models. The branchings are indeed highly leptonic due to the hypercharge enhanced couplings.

Recently the CDF and DØ collaborations have published new data sets with as much as 2.5 fb^{-1} [211] of data, which is about a factor of 6 larger than when the analysis on narrow resonances at the Tevatron was given [170] showing that a Z prime from the Stueckelberg extensions [167, 170] produces a viable candidate for Z prime resonance at the 200 GeV range (240 GeV?). Now, given that the experiments at Fermilab will most likely not see a Z prime signal for any model with a Z prime mass beyond around 800 GeV, it becomes imperative to study models which accommodate narrow resonances at mass scales where the Tevatron is more sensitive. Similar phenomena regarding narrow resonances, such as that which has been discussed here, are seen in other classes of models such as those based on universal extra dimensions [212], models with a shadow sector [193, 192], and in the models considered in Ref. [213]. Other recent interesting classes of Z prime models include [214],[215],[216]. While E6 or a LR model may be realized in nature, the Z primes produced in these models which are currently discussed in the experimental works will likely not be seen at Fermilab.

Chapter 8

Narrow Resonances at the LHC

Analyzed here is the capability of the LHC to detect narrow resonances using high luminosities and techniques for discriminating among models are given. The analysis is carried out with focus on Stueckelberg extension of the Standard Model (StSM) which naturally leads to a very narrow Z' resonance. Comparison is made to another class of models based on the warped geometry which also lead to a narrow resonance via a massive graviton (G). Methods of distinguishing the StSM Z' from the massive graviton at the LHC are analyzed using the di-lepton final state in the Drell-Yan process $pp \to Z' \to l^+l^-$ and $pp \to G \to l^+l^-$. It is shown that the signature spaces in the $\sigma_{pp} \cdot Br(l^+l^-)$-resonance mass plane for the Z prime and for the massive graviton are distinct. Angular distributions in the di-lepton C-M system are also analyzed. It is shown that these distributions lie high above the background and are distinguishable from each other. A remarkable result that emerges from the analysis is the observation that the StSM model with Z' widths even in the MeV and sub-MeV range for Z' masses extending in the TeV region can produce detectable cross section signals in the di-lepton channel in the Drell-Yan process with luminosities accessible at the LHC. Here the result is derived within the specific StSM class of

models, however, the capability of the LHC to probe models with narrow resonances in this range may hold more generally.

8.1 LHC Observables and Constraints on the StSM Parameter Space

A relevant quantity that may be measured at the LHC is $\sigma_{pp} \cdot Br(X \to l^+l^-) \equiv \sigma \cdot Br(X \to l^+l^-)$ in the process $pp \to X \to l^+l^-$ where X is a neutral resonant state produced in pp collisions which can decay into a lepton pair. Here we give a theoretical analysis of this quantity for the case when $X = Z'$, and in the next section we will consider the case when $X = G$, the spin 2 graviton of a warped geometry. In the analysis of $\sigma \cdot Br(Z' \to l^+l^-)$ we will discuss two regions: a low mass region with the di-lepton invariant mass $M_{l\bar{l}}$ up to 800 GeV and a high mass region with $M_{l\bar{l}}$ extending from 800 GeV up to the maximum relevant mass reach of the LHC. The reason for this ordering is as follows: the region with $M_{l\bar{l}}$ up to 800 GeV has already begun to be explored at the Tevatron using up to about 2 fb^{-1} of data, and the CDF and DØ data puts constraints on ϵ as a function of the di-lepton invariant mass. Thus in the analysis of the low mass $M_{l\bar{l}}$ region at the LHC we can incorporate these constraints. However, one has no direct constraints in the di-lepton invariant mass region above 800 GeV, which explains the separate analyses of $\sigma \cdot Br(Z' \to l^+l^-)$ for the low and high mass regions.

We begin with an analysis of $\sigma \cdot Br(Z' \to l^+l^-)$ in the low mass region where we use the constraints on $(\epsilon, M_{Z'})$ as obtained in Ref. [170] using the cross section limits from [204]. The results are displayed in Fig. (8.1). As expected one finds that the current data on $\sigma \cdot Br(Z' \to l^+l^-)$ constrains only the mass region of Z' for values $M_{Z'} \lesssim 350$ GeV. We note that for ϵ as high as $\approx .04$ one may have an StSM Z' as

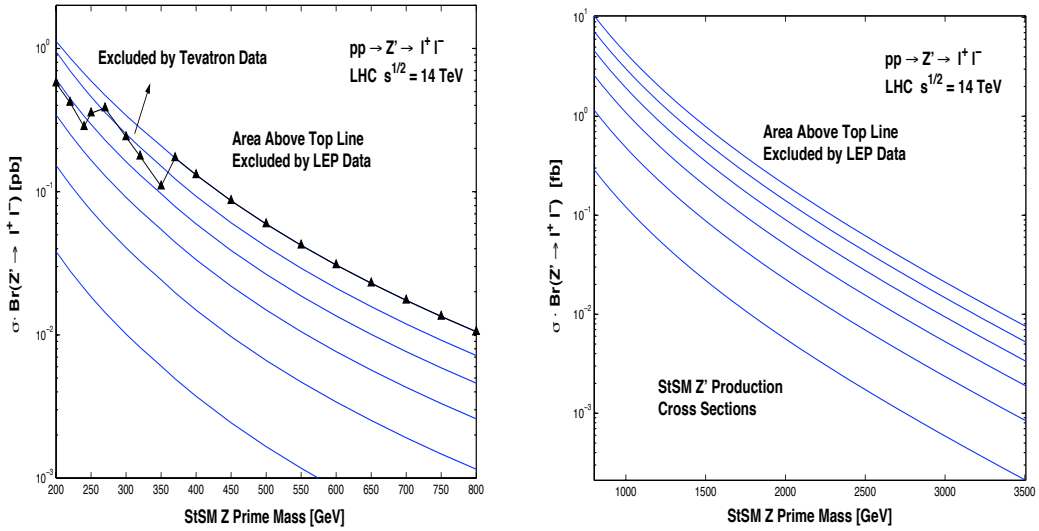

Figure 8.1: (a) The production cross section $\sigma \cdot Br(Z' \to l^+l^-)$ [pb] in the StSM at the LHC in the low mass region with the inclusion of the LEP and Tevatron constraints. The curves in descending order correspond to values of ϵ from .06 to .01 in steps of .01. (b) The production cross section $\sigma \cdot Br(Z' \to l^+l^-)$ [fb] for the StSM at the LHC in the Z' high mass region up to Z' mass of ≈ 3.5 TeV. The curves correspond to values of ϵ ranging from .06 to .01 in descending order in steps of .01. The StSM production cross sections sit several orders of magnitude below those of other Z' models. (From [171].)

low as 175 GeV, while with a Z' mass of 250 GeV, ϵ may be as high as $\approx .035$ within the current experimental limits. Next we discuss the high mass region for the StSM Z'. As discussed above the high mass region of StSM Z' remains unconstrained by the CDF and DØ data, and thus in this region only the LEP electroweak constraints apply. The analysis of Fig. (8.1) gives a plot of $\sigma \cdot Br(Z' \to l^+l^-)$ as a function of $M_{Z'}$ in the high mass region for values of ϵ ranging from .01 to .06 in ascending order in steps of .01. From Fig. (8.1) and from the analysis of Refs. [217, 218] for other Z' models one infers that the production cross section for StSM Z' lies orders of magnitude below those for the Z' production in E6 models and other Z' models. The size of $\sigma \cdot Br(Z' \to l^+l^-)$ thus provides a clear signature which differentiates the StSM Z' model from other Z' models.

8.1.1 Signal to Background Ratio

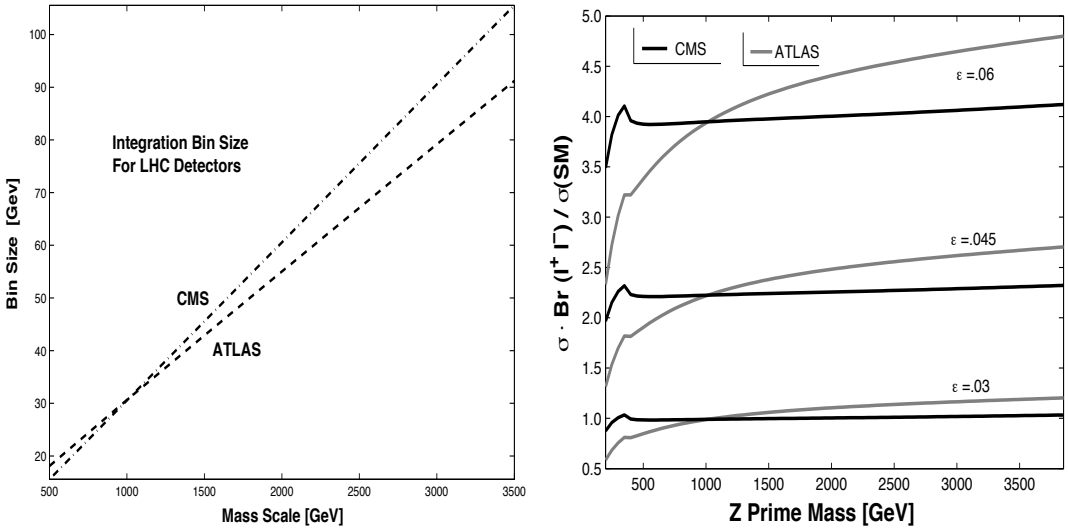

Figure 8.2: (a)The mass window or bin size as a function of the mass scale for the ATLAS and CMS detectors. (b) The ratio $\sigma \cdot Br(Z' \to l^+l^-)_{StSM}/\sigma_{SM}(Z, \gamma \to l^+l^-)$ including the $\gamma - Z$ interference term in the SM as a function of the Z' mass for the ATLAS and CMS detectors assuming for values of ϵ in the range .03-.06. The signal to background ratio is larger for the CMS detector at low mass scales while it is larger for the ATLAS detector at large mass scales with a cross over occurring at around 1 TeV. (From [171].)

The di-lepton channel will be analyzed at the LHC in the ATLAS [219] and CMS [220] detectors, and as is discussed below, both detectors have the ability to probe the narrow StSM Z' boson. Experimentally, the discovery of a narrow resonance depends to a significant degree on the bin size for data collection with the chance of detection increasing with a decreasing bin size. This is so because the integral over the bin is effectively independent of the bin size for the signal (assuming the narrow resonance falls within the bin). However, this integral is essentially linearly dependent on the bin size for the SM background. In this particular analysis of the SM background we have included the Z, γ, and $\gamma - Z$ interference terms in the Drell-Yan analysis, but have not included the backgrounds from other sources such as from $t\bar{t}, b\bar{b}, WW, WZ, ZZ$ etc. However, these backgrounds are known to be at best a few percent of the Drell-

Yan background [221] in the channel of interest under standard cuts for this mode. Regarding the bin size, it depends on the energy resolution σ_E/E of the calorimeter. For an electromagnetic calorimeter the energy resolution is typically parametrized by $\sigma_E/E = a/\sqrt{E} \oplus b \oplus c/E$ where addition in quadrature is implied[222]. The term proportional to $1/\sqrt{E}$ is the so called stochastic term and arises from statistic related fluctuations. The term b is due to detector non-uniformity and calibration errors, and the term c is due mostly to noise. For the ATLAS detector (liquid Ar/Pb) the energy resolution is parametrized by [222] $\sigma_E = 10\%/\sqrt{E} \oplus .4\% \oplus .3/E$ and for the CMS detector ($PbWO_4$) it is parametrized by $\sigma_E = 3\%/\sqrt{E} \oplus .5\% \oplus .2/E$ where E is in units of GeV. From the above we find the following relations for the bin size B (taken to be $6\sigma_E$) at the mass scale M (M is measured in units of TeV) [171] [1]

$$\begin{aligned} \mathrm{B_{ATLAS}} &= 24(.625M + M^2 + .0056)^{1/2}\mathrm{GeV} \\ \mathrm{B_{CMS}} &= 30(.036M + M^2 + .0016)^{1/2}\mathrm{GeV}. \end{aligned} \tag{8.1}$$

For $M > 3$ TeV, the M^2 term dominates in Eq.(8.1) and the bin size goes linearly in M, so $\mathrm{B_{ATLAS}} \sim 24M$ GeV and $\mathrm{B_{CMS}} \sim 30M$ GeV for large M. A plot of bin sizes as a function of the mass scale is given in Fig.(8.2) for the two LHC detectors. One finds that at low mass scales the CMS has a somewhat better energy resolution and thus a somewhat smaller bin sizes and at large mass scales ATLAS has a somewhat better energy resolution and thus a somewhat smaller bin size with a cross over at $M \sim 1$ TeV. However, on the whole the energy resolution and the bin size of the two detectors are comparable within about 10%. For the StSM Z' the analysis of Fig. (8.2) shows that the signal to background is greater than unity in significant parts of the parameter space, and in some cases greater than 4, thus illustrating that the

[1] We note in passing that this formula appeared later in Ref. [223]

LHC has the ability to detect a strong signal for a StSM Z'.

8.1.2 How Narrow a Width Can LHC Probe?

In Fig. (8.3) we give the discovery reach for finding the StSM Z' for different decay widths as a function of the Z' mass, with various values of ϵ for integrated luminosities in the range 10 fb^{-1} to 1000 fb^{-1}. The criterion used for the discovery limit in the analysis given here is an assumption that $5\sqrt{N_{SM}}$ events or 10 events, whichever is larger, constitutes a signal where N_{SM} is the SM background, and we have scaled the bin size with $M_{Z'}$ appropriate for the ATLAS detector with a conservative lower limit of 20 GeV below 0.5 TeV. In this part of the analysis we have assumed that detector effects can lead to signal and background losses of 50 percent (see Section (8.2.2)). If better efficiency and acceptance cuts are available, the discovery reach of the LHC for finding a Z' will be even higher than what we have displayed. With an assumption of efficiencies as stated above, here one finds that the LHC can probe a 100 MeV Z' up to about 2.75 TeV and a 10 MeV width up to a Z' mass of about 1.5 TeV. A more detailed exhibition of the capability of the LHC to probe the StSM Z' model is given in the right panel of Fig. (8.3). Here one finds that the StSM model with a Z' width even in the MeV and sub-MeV range will produce a detectable signal in the di-lepton channel in the Drell-Yan process with luminosities accessible at the LHC. While the analysis above is for the specific StSM model, the general features of this analysis may hold for a wider class of models which support narrow resonances.

In terms of ϵ, with 100 fb^{-1} of integrated luminosity, one can explore a Z' up to about 2 TeV with $\epsilon = 0.06$, and this limit can be pushed to ≈ 3 TeV with 1000 fb^{-1} of integrated luminosity. Further, one finds that for 1000 fb^{-1} of integrated luminosity, one can explore a Z' up to about 2 TeV for ϵ as low as $\lesssim 0.02$ [171].

In Fig. (8.4) we give a comparison of the LHC's ability to probe the narrow StSM

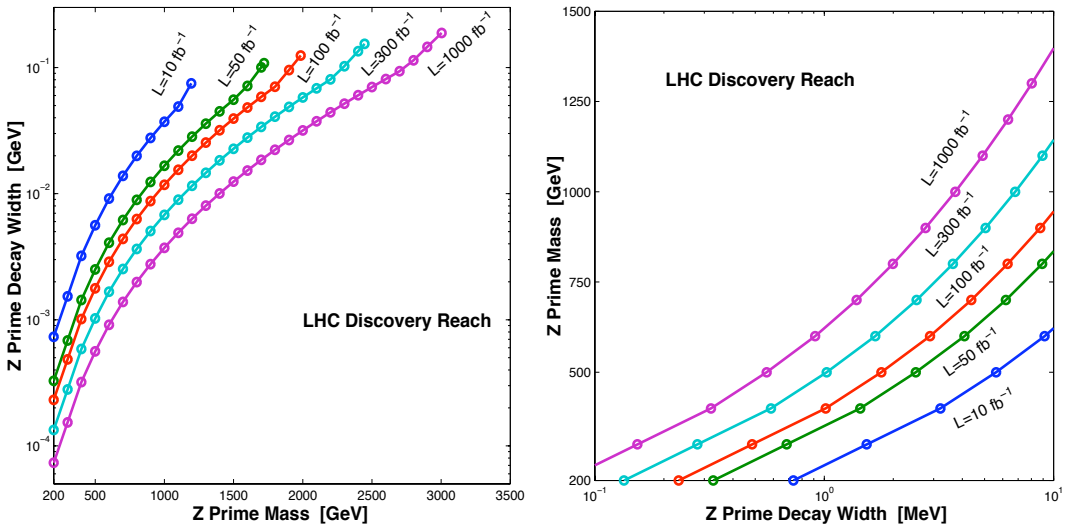

Figure 8.3: (Left) Discovery limits of Z' translated into the decay width of the Z' in StSM with the discovery limit defined by $5\sqrt{N_{SM}}$ or by 10 events, whichever is larger. The inflections, or kinks, in the plots are precisely the points of transitions between the two criteria. Regions to the left and above each curve can be probed by the LHC at a given luminosity. The top point on each curve corresponds to $\epsilon = .061$. The analysis is done for the ATLAS detector but similar results hold for the CMS detector. (Right) A plot of the discovery reach of the LHC for small StSM Z' widths. The allowed regions are to the right and below each curve for a given luminosity. (From [171].)

Z' relative to other Z' models [224, 225] to address the question of how the StSM Z' "stacks up" to these models. In order to make the appropriate comparisons of the discovery limits for the StSM with the other Z prime models we do not impose detector cuts on the StSM Z' limits displayed in Fig. (8.4), since such cuts were not imposed for the discovery limits of other Z' models shown in Fig. (8.4). The analysis of Fig. (8.4) shows that the StSM Z', even with its exceptionally narrow width, may be probed on scales comparable with models that have resonance widths of the order of several GeV or higher.

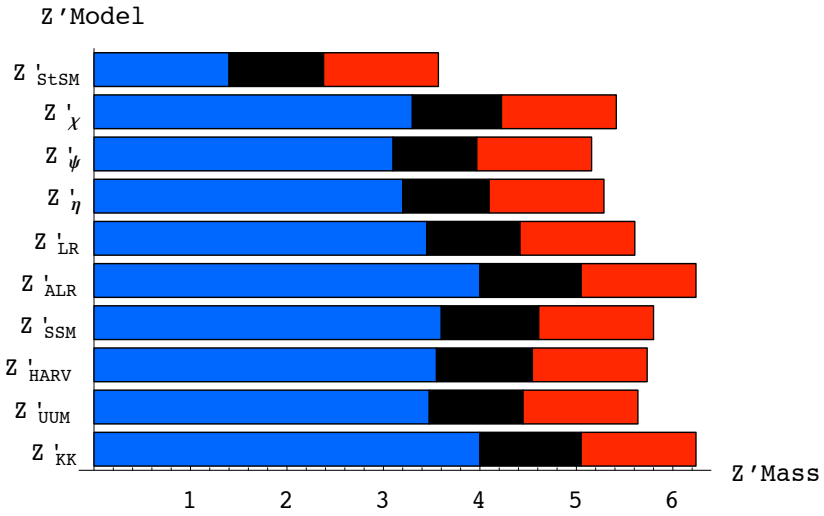

Figure 8.4: The discovery reach for Z' in StSM (without detector cuts) and several other Z' models at the LHC. The length of the bars indicate integrated luminosities of 10 fb^{-1} (blue), 100 fb^{-1} (black), and 1000 fb^{-1} (red) using 10 events as the criterion for discovery [224, 225]. The analysis indicates that the Z' of StSM can be probed up to ≈ 3.5 TeV at the LHC with 1000 fb^{-1} of integrated luminosity. With inclusion of detector cuts the discovery reach of the LHC for the StSM Z' comes down to about 3 TeV.(From [171].)

8.2 StSM and Massive Graviton at the LHC

As discussed above one finds that the Stueckelberg Z' boson is a very narrow resonance which sets it apart from other Z' models. However, there is another class of models, i.e., models based on warped geometry [207, 226] (labeled RS models), which can mimic the Stueckelberg Z' in a certain part of the parameter space as far as the narrowness of the resonance is concerned. It was shown in the analysis of Ref. [170] that the signature spaces for these two models lie close to each other in certain regions of their respective parameter spaces, but the models are still distinguishable in the di-lepton mass region accessible at the Tevatron. Here we extend the analysis of their relative signatures to the LHC energies. The geometry of RS models is a slice of AdS_5 described by the metric $ds^2 = exp(-2kr_c|\phi|)\eta_{\mu\nu}dx^\mu dx^\nu - r_c^2 d\phi^2$, $0 \leq \phi \leq \pi$,

where r_c is the radius of the extra dimension and k is the curvature of AdS_5, which is taken to be the order of the Planck scale. We work in the regime where the SM particles are confined to the TeV scale Brane, while gravity is propagating in the bulk [207, 208]. The effective scale that enters in the electroweak region is the scale $\Lambda_\pi = \overline{M}_{\rm Pl} exp(-kr_c\pi)$, and for reasons of naturalness it is typically constrained by the condition $\Lambda_\pi < 10$ TeV. Values of $k/\overline{M}_{\rm Pl}$ over a wide range $10^{-5} - .1$ have been considered in the literature [227]. However, the range below .01 appears to be eliminated from the electroweak constraints. In this analysis we consider the lightest massive graviton mode .

8.2.1 Massive Graviton of Warped Geometry

We consider the process $pp \to G \to f\bar{f}$ for the first massive graviton mode in the RS model. The partonic production cross section for this mode receives contributions both from quarks and gluons, and is given by [228, 229, 230, 231, 232]

$$\frac{d\sigma^G_{q\bar{q}}}{dz} + \frac{d\sigma^G_{gg}}{dz} = \frac{1}{2}\frac{\kappa^4 M^6}{320\pi^2}\left[\Delta_{q\bar{q}}(z) + \Delta_{gg}(z)\right]\frac{1}{(M^2 - M_G^2)^2 + M^2\Gamma_G^2}. \tag{8.2}$$

The total decay width that enters above is given by the sum of the partial widths which are [228, 233, 230]

$$\Gamma(G \to V\bar{V}) = \delta\frac{\kappa^2 M_G^3}{80\pi}(1 - 4\delta_V)^{1/2}\left(\frac{13}{12} + \frac{14}{3}\delta_V + 4\delta_V^2\right)\theta(M_G - 2M_V) \tag{8.3}$$

$$\Gamma(G \to f\bar{f}) = N_f^c\frac{\kappa^2 M_G^3}{320\pi}(1 - 4\delta_f)^{3/2}(1 + \frac{8}{3}\delta_f)\theta(M_G - 2m_f) \tag{8.4}$$

$$\Gamma(G \to gg) = \frac{\kappa^2 M_G^3}{20\pi} \tag{8.5}$$

$$\Gamma(G \to \gamma\gamma) = \frac{\kappa^2 M_G^3}{160\pi}. \tag{8.6}$$

Here $\delta_f = m_f^2/M_G^2$, $\delta_V = M_V^2/M_G^2$, and $\delta = (1/2, 1)$ for $(V = W, Z)$. For the first massive mode, κ is given by [233, 230, 231]

$$\kappa = \sqrt{2}\frac{x_1}{m_G}\frac{k}{\overline{M}_{Pl}} \tag{8.7}$$

where $x_1 = 3.8317$ is the first root of the Bessel function of order 1, and $\overline{M}_{Pl}$ is the reduced Planck mass in four dimensions ($\overline{M}_{\rm Pl} = M_{\rm Pl}/\sqrt{8\pi}$). The leading order angular dependence is given in terms of [230, 231, 232]

$$\Delta_{q\bar{q}}(z) = \frac{\pi}{8N_c}\frac{5}{8}(1 - 3z^2 + 4z^4), \qquad \Delta_{gg}(z) = \frac{\pi}{2(N_c^2 - 1)}\frac{5}{8}(1 - z^4). \tag{8.8}$$

In the narrow width approximation we have to NLO

$$\begin{aligned}\frac{d\sigma_{pp}^G}{dz} &= K^G(M_G^2)\frac{1}{2s}\frac{\kappa^4 M_G^6}{320\pi^2}\frac{\pi}{M_G\Gamma_G} \times \\ &\left[\sum_q \Delta_{q\bar{q}}(z)\mathcal{W}_{\{pp(q\bar{q})\}}(s, M_G^2) + \Delta_{gg}(z)\mathcal{W}_{\{pp(gg)\}}(s, M_G^2)\right]\end{aligned} \tag{8.9}$$

where $\mathcal{W}_{pp(q\bar{q})}$ is defined in Section 6 and $\mathcal{W}_{pp(gg)}$ is defined by

$$\mathcal{W}_{\{pp(gg)\}}(\tau) = \int_0^1 \int_0^1 dxdy\delta(\tau - xy) f_{g,p}(x) f_{g,p}(y), \tag{8.10}$$

and the more strongly mass dependant RS K factor ($K^G = K^G(M_G^2)$) is discussed in detail in Refs. [232]. The production cross section including the quark and gluon contributions is in the narrow width approximation given by

$$\begin{aligned}\sigma \cdot Br(G \to l^+l^-) = K^G(M_G^2)\frac{1}{s}\frac{\kappa^4 M_G^6}{15360}\frac{1}{M_G\Gamma_G}\sum_q \mathcal{W}_{\{pp(q\bar{q})\}}(s, M_G^2) \\ + K^G(M_G^2)\frac{1}{s}\frac{\kappa^4 M_G^6}{10240}\frac{1}{M_G\Gamma_G}\mathcal{W}_{\{pp(gg)\}}(s, M_G^2).\end{aligned} \tag{8.11}$$

8.2.2 Signature Spaces of StSM Z' and of the Graviton

A relative comparison of the StSM and of the RS model is given in Table (8.1) where the decay width of the Stueckelberg Z' boson for the case $\epsilon = 0.06$ is given as a function of the Z' mass in the range (1000-3000) GeV, and the corresponding $\sigma \cdot Br(G \to l^+l^-)$ is exhibited. Also shown are the decay widths for an RS graviton in the same mass range for $k/\overline{M}_{\rm Pl} = 0.01$.

$(M_{Z'}, M_G)$	$\Gamma_{Z'}$ (GeV)	Γ_G (GeV)	$\sigma_{Z'} \cdot Br$ (fb)	$\sigma_G \cdot Br$ (fb)
1000	0.058	0.141	4.29	9.98
1250	0.073	0.176	1.72	3.11
1500	0.087	0.212	0.779	1.15
1750	0.102	0.247	0.384	0.475
2000	0.117	0.283	0.200	0.215
2250	0.131	0.318	0.109	0.104
2500	0.146	0.354	0.061	0.053
2750	0.160	0.389	0.035	0.028
3000	0.175	0.425	0.021	0.015

Table 8.1: A comparison of the narrow resonance widths and $\sigma \cdot Br(l^+l^-)$ in StSM for $\epsilon = .06$ and in the RS warped geometry with $k/\overline{M}_{\rm Pl} = .01$ as a function of the resonance mass in GeV. (From [171].)

Quite remarkably, the spin 1 Z' of the StSM and the spin 2 massive graviton of the RS model have nearly identical signatures in terms of the decay widths and the production cross sections around a resonance mass of 2 TeV (with or without out detector cuts). In Table (8.2) we give an analysis of the number of events that can be observed in the ATLAS detector with 100 fb^{-1} of integrated luminosity. One finds that for high masses the number of events that one expects to see at the LHC for the StSM Z', with $\epsilon = 0.06$, are similar to the number of events one expects for the RS model for $k/\overline{M}_{\rm Pl} = 0.01$. For the case of the RS model, simulations conducted by Ref. [233] show that overall detector losses range from (27-38) percent between (500-2200) GeV, and we have extrapolated these cuts to the 3 TeV mass region. For the case of

$(M_{Z'}, M_G)$	Bin (GeV)	N_{SM}	$N_S = (N_{St}, N_{RS})$	N_S^{min}
1000	30.65	54.45	(214.33,716.96)	36.90
1250	36.79	20.95	(85.90,216.96)	22.89
1500	42.89	9.22	(38.94,77.73)	15.18
1750	48.96	4.44	(19.18,31.30)	10.53
2000	55.02	2.27	(10.01,13.72)	10
2250	61.07	1.22	(5.46,6.41)	10
2500	67.11	0.68	(3.07,3.15)	10
2750	73.14	0.39	(1.77,1.60)	10
3000	79.17	0.22	(1.04,0.84)	10

Table 8.2: A comparison of the signal events with integrated luminosity of $\mathcal{L} = 100$ fb^{-1} in the StSM for the case $\epsilon = .06$ with the signal in the RS warped geometry for $k/\overline{M}_{Pl} = .01$ including ATLAS detector effects as a function of the resonance mass in GeV. Acceptance(A) and efficiency(ε) for the RS case is as in Ref. [233], while for the StSM we use the spin 1 detector losses given in Ref. [234] ≈ 50 % as discussed in the text. For $X = (Z', G)$ of Table(8.1), $N_S = (\sigma \cdot Br)\varepsilon AL$, $N_B = N_{SM}$ (background integrated over the bin), $N_S^{min} = 5\sqrt{N_B}$ or 10, whichever is larger. The minimum signal cross section is $(\sigma \cdot Br)^{\min} = (\varepsilon AL)^{-1} N_S^{min}$ for each model.(From [171].)

Z', which has a different angular dependency than the graviton due to spin, we have assumed a uniform 50 percent loss of events at in the range of Z' mass investigated. This reduction factor is consistent with the reduction factor used by Ref. [234], and is similar to the reduction factor used by other groups [235]. For the SM background, denoted as $N_B = N_{SM}$, the same detector loss is assumed, and it can be seen in Table (8.2) that this simulation is in good agreement with the analysis of Ref. [233]. Of course a slightly more realistic analysis of the number of events that may be observed requires simulating detector efficiencies more accurately [236, 237, 238, 221, 234].

In Fig. (8.5) (left panel) we give a comparison of the signature spaces for the decay of the StSM Z' and of the RS graviton in the warped geometry model using the decay width-resonance mass plane. The allowed regions (shaded) for the two models are exhibited, where the unshaded regions correspond to constrained regions of the parameter spaces of the two models. One finds that although there is a region

of the parameter space of the RS model where the decay widths can be narrow, the region of potential overlap with the StSM is avoided if one includes the constrains of the oblique parameters [239, 240]. Fig. (8.5) (right panel) gives a more direct method for differentiating the two classes of models. Here one has plots of $\sigma \cdot Br(Z' \to l^+l^-)$ and $\sigma \cdot Br(G \to l^+l^-)$ as a function of the resonance mass. One finds that the allowed regions of the signature space of the two models consistent with the parameter space constraints provides a clear differentiation between these two classes of models. Thus Fig. (8.5) provides an important tool for establishing the nature of the resonance once a narrow resonance is discovered. For example, the $\sigma \cdot Br(Z' \to l^+l^-)$ is an order of magnitude or more smaller than $\sigma \cdot Br(G \to l^+l^-)$ over most of the di-lepton invariant mass that will be probed by the Drell-Yan process at the LHC.

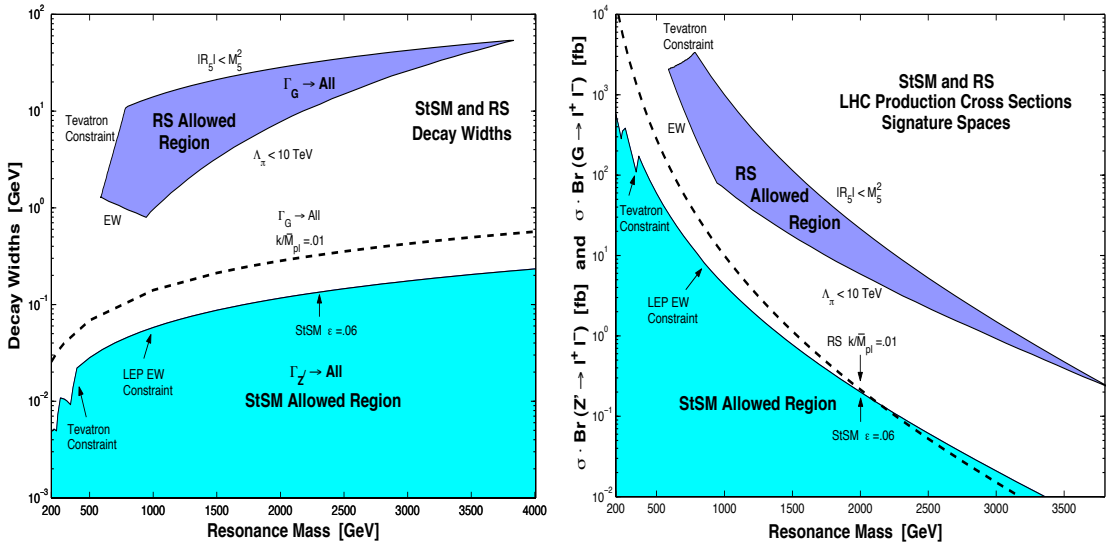

Figure 8.5: A comparison of the allowed region in resonance decay width - resonance mass plane and in the $\sigma \cdot Br(l^+l^-)$ plane for the (Z') in the StSM and the first graviton mode (G) in the RS model. The dashed line is for the RS case with $k/\overline{M}_{Pl} = .01$. The allowed (shaded) regions are constructed by utilizing the constrained parameter spaces of StSM [170] and the RS model [208, 241, 204].(From [171].)

8.2.3 Angular Distributions from $pp \to (Z', G) \to l^+l^-$

Angular distributions in the C-M frame of the final di-lepton state give clear signatures of the spin of the produced particle in the Drell-Yan process (for recent works see, for example, Refs.[242, 243]). Thus angular distributions are a powerful tool in distinguishing the StSM Z', a spin 1 particle, from the massive graviton of warped geometry, a spin 2 particle. The CDF group has already carried out angular distribution analyses [210] using the cumulative data at the Tevatron and more detailed analyses are likely to follow. Similar analyses at the LHC would allow one to investigate the spin of an observed resonance with much more data. In the following we give a relative comparison of the angular distributions arising from the StSM Z' and from the massive graviton of warped geometry. The comparison of the angular distribution in the di-lepton channel arising from the StSM Z' and the massive graviton of warped geometry is given in Fig.(8.6) for a resonance mass of 2 TeV, the mass region where an overlap between the two models can occur if the constraints on the RS model are relaxed. The left graph in Fig. (8.6) gives the angular distributions arising for the Z' exchange but without the Standard Model background, i.e., what is plotted is the pure signal. Also plotted is the pure signal from the graviton exchange which consists of contributions from the quarks and the gluons which are separately exhibited. In the right panel of Fig. (8.6) the angular distributions arising for the StSM Z' and for the massive graviton exchanges including the Standard Model background are exhibited. The analysis shows that the signal plus the background lies significantly higher than the SM background, and further the sum of the Z' signal and the SM background is easily distinguishable from the sum of the massive graviton signal and the SM background. The angular distributions for the graviton exchange are sensitively dependent on the graviton mass, mainly due to the sensitivity of the PDF [202] for the gluon on the mass scale. Thus the angular distributions for the graviton will

change with the mass scale and change significantly. However, the angular distributions for the Z' and for the graviton will continue to be identifiably distinct and allow one to distinguish between these two classes of narrow resonance models.

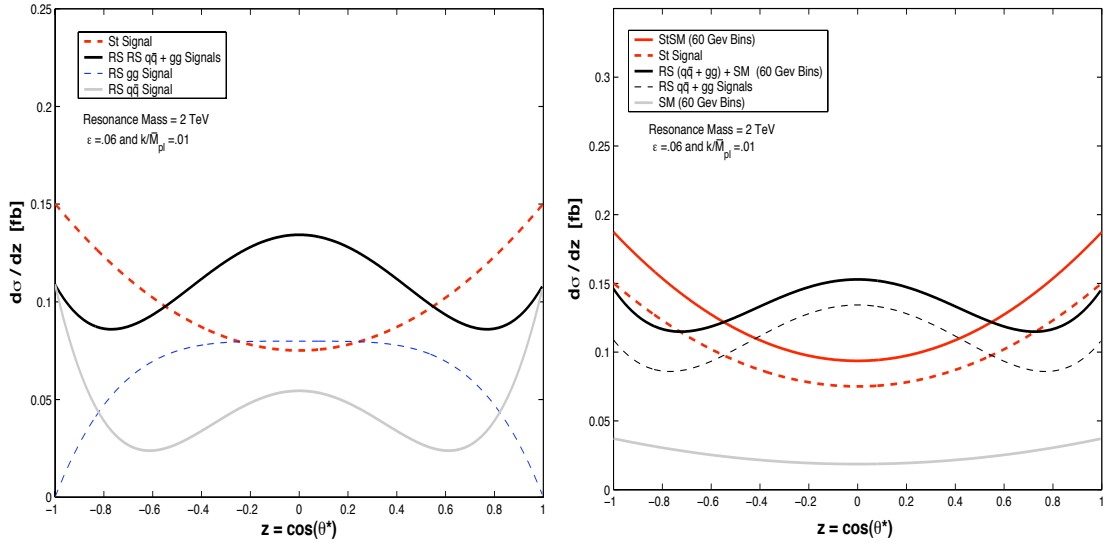

Figure 8.6: An exhibition of the angular distribution $d\sigma(pp \to Z' \to l^+l^-)/dz$ for the StSM model and $d\sigma(pp \to G \to l^+l^-)/dz$ for the RS model in the di-lepton center of mass system. For the StSM, ϵ is taken at .06 and G is the first resonant mode of the RS model, with $(k/\overline{M}_{\rm Pl}) = .01$ and the resonance mass is 2 TeV in each case. For the RS model the parameter choice requires relaxing the oblique constraints and the constraint on Λ_π.(From [171].)

8.3 Summary

Here we have carried out an investigation of narrow resonances with specific focus on two classes of models which have recently emerged where narrow resonances arise quite naturally. The first of these are the $U(1)_X$ extensions of the Standard Model gauge group where the extra gauge boson becomes massive via the Stueckelberg mechanism. A narrow Z' naturally arises in these models. The second class of models are those based on warped geometry which give rise to a narrow graviton resonance for $k/\overline{M}_{\rm Pl} \sim .01$. Here we investigated the capability of the LHC to

discover narrow resonances specifically belonging to these classes of models and to discriminate between them by examining their signature spaces. The analysis using the di-lepton production in the Drell-Yan process via the Z' boson shows that one will be able to explore a narrow Z' resonance of Stueckelberg origin up to about 2 TeV with 100 fb^{-1} of integrated luminosity and further up to 2.5 TeV with 300 fb^{-1} of integrated luminosity. With 1000 fb^{-1} of integrated luminosity one could even explore a Stueckelberg Z' beyond 3 TeV.

We carried out a similar analysis for the di-lepton production in the warped geometry RS model which also has the potential of supporting a narrow resonance. It is then interesting to ask how a Stueckelberg type narrow resonance could be distinguished from a narrow massive graviton of warped geometry. Indeed there is a range of the parameter space where an overlap exists between the two models with the width of the massive graviton of the warped geometry being similar to the width of the Z' arising from the Stueckelberg model. We have shown that one of the clear distinguishing features between them is $\sigma \cdot Br(l^+l^-)$ for di-lepton production in the Drell-Yan process which proceeds through the interaction $pp \to Z' \to l^+l^-$ for the Stueckelberg model and via $pp \to G \to l^+l^-$ for the case of the RS model. The analysis of Fig. (8.5) shows that for any resonance mass the signature spaces of the StSM and of the RS model are distinct and one can discriminate between them using the $\sigma \cdot Br(l^+l^-)$ criterion. In addition, the angular distributions in the di-lepton center of mass system provide a clear discrimination between the two models. Here one finds that the angular distributions from the StSM Z' and from the massive graviton lie well above the Standard Model background and further are distinctly dissimilar.

Some general features of the searches for narrow resonances were also discussed. The bin size used in data collection has a direct bearing on the signal to background ratio. The analysis presented here reveals the remarkable phenomenon that the mod-

els considered here can be tested even when the resonance widths are small and the resonance masses are large. Specifically one finds that the StSM model can produce observable cross section signals with a Z' width lying in the MeV or even in the sub-MeV range while the Z' mass may be in hundreds of GeV to TeV range. While the result is presented for the specific case of StSM Z' model, similar considerations may apply to a wider class of models which support a narrow resonance. The evidence for a narrow resonance will be an important hint for an altogether new type of physics beyond the Standard Model and possibly a hint of a string origin [171].

Chapter 9

Dark Matter from the Hidden Sector

The main focus of this Chapter is an extension of the class of models considered in Refs. [167, 168, 169, 170, 171] by including kinetic mixing between the two Abelian $U(1)$ gauge fields [174]. Specifically we consider the extended electroweak sector with the gauge groups $SU(2)_L \times U(1)_Y \times U(1)_X$ where the Stueckelberg mechanism along with the spontaneous breaking in the Higgs sector generates the vector boson mass, and a mixing in the gauge kinetic energy of the $U(1)_X \times U(1)_Y$ sector is included. Inclusion of the kinetic mixing in the Stueckelberg extension enhances significantly the parameter space where new physics can exist consistent with the stringent LEP, Tevatron, and WMAP constraints. This parameter space includes the possibility of a narrow Z' resonance very distinct from the Z' of the conventional models. We also show that in precisely the same region of the parameter space where the relic density constraints are satisfied [174], the recent PAMELA and ATIC anomalies can be fit due to an enhancement in the halo cross section from the Breit-Wigner pole [175].

9.1 Kinetic and Stueckelberg Mass Mixings

In this section we discuss the $U(1)_X$ Stueckelberg extension of the Standard Model (SM) with gauge kinetic mixing (StkSM)[174]. In the gauge vector boson sector, the effective Lagrangian is given by [174]

$$\begin{aligned}\mathcal{L}_{\rm StkSM} &= \mathcal{L}_{\rm SM} + \Delta\mathcal{L}, \\ \Delta\mathcal{L} &\ni -\frac{1}{4}C_{\mu\nu}C^{\mu\nu} - \frac{\delta}{2}C_{\mu\nu}B^{\mu\nu} - \frac{1}{2}(\partial_\mu\sigma + M_1 C_\mu + M_2 B_\mu)^2 + g_X J_X^\mu C_\mu.\end{aligned}$$

Thus there is more generally both mass mixing (M_1, M_2) of the $U(1)$ vector fields and and kinetic mixing δ of the field strength tensors. The Lagrangian is invariant under the $U(1)_X \times U(1)_Y$ gauge transformations

$$\begin{aligned}&\delta B_\mu = \partial_\mu \lambda_X,\ \delta C_\mu = 0,\quad \delta\sigma = -M_2\lambda_X \\ &\delta B_\mu = 0,\ \delta C_\mu = \partial_\mu\lambda_Y,\ \delta\sigma = -M_1\lambda_Y.\end{aligned} \tag{9.1}$$

Consider first the kinetic part of the Lagrangian coupled to the SM. One has in the neutral sector

$$\mathcal{L}_\delta = -\frac{1}{4}C_{\mu\nu}C^{\mu\nu} - \frac{1}{4}B_{\mu\nu}B^{\mu\nu} - \frac{\delta}{2}B^{\mu\nu}C^{\mu\nu} - \frac{1}{4}A^3_{\mu\nu}A^{3\mu\nu} = -\frac{1}{4}\mathcal{V}^T_{\mu\nu}\tilde{\mathcal{K}}\mathcal{V}^{\mu\nu} \tag{9.2}$$

where $\mathcal{V}^T_{\mu\nu} = (C, B, A^3)_{\mu\nu}$ and where the matrix $\tilde{\mathcal{K}}$ is given by

$$\tilde{\mathcal{K}} = \begin{bmatrix} 1 & \delta & 0 \\ \delta & 1 & 0 \\ 0 & 0 & 1 \end{bmatrix}, \tag{9.3}$$

Now to diagonalize the kinetic term one can introduce the matrix (which I will call $\mathcal{KO}$)

$$\mathcal{KO} = \begin{bmatrix} 1 & -S_\delta & 0 \\ 0 & C_\delta & 0 \\ 0 & 0 & 1 \end{bmatrix}, \qquad S_\delta = \delta/\sqrt{1-\delta^2} = \delta C_\delta \ . \tag{9.4}$$

Under the transformation $\mathcal{V}_{\mu\nu} = \mathcal{KO}\mathcal{E}'_{\mu\nu}$ one observes that $(\mathcal{KO})^T\tilde{\mathcal{K}}(\mathcal{KO}) = 1_{3\times 3}$. Adding the Stueckelberg mass mixing term, and after a rotation $\mathcal{R}^T\mathcal{R} = 1$, with $\mathcal{E}'_\mu = \mathcal{R}\mathcal{E}_\mu$ (and for the field strength tensor which remains diagonal on the orthogonal transformation $\mathcal{R}$) we obtain

$$\mathcal{L}_{\rm Mass} = -\frac{1}{2}\mathcal{E}^T(\mathcal{KOR})^T M^2_{\rm St}(\mathcal{KOR})\mathcal{E}, \quad \text{with } \ \mathcal{E}^T = (Z', Z, A_\gamma) \ . \tag{9.5}$$

The mass squared matrix is

$$\mathcal{M}^2 = (\mathcal{KO})^T M^2_{\rm St}\mathcal{KO} = \begin{pmatrix} M_1^2 & M_1^2\bar{\epsilon} & 0 \\ M_1^2\bar{\epsilon} & M_1^2\bar{\epsilon}^2 + \frac{v^2}{4}\gamma^2(1+\bar{\epsilon}^2) & -\frac{v^2}{4}g_2\gamma\sqrt{1+\bar{\epsilon}^2} \\ 0 & -\frac{v^2}{4}g_2\gamma\sqrt{1+\bar{\epsilon}^2} & \frac{v^2}{4}g_2^2 \end{pmatrix}. \tag{9.6}$$

This is precisely the St mass matrix previously studied, with the mass and kinetic mixings entering through the single parameter

$$\bar{\epsilon} = \frac{\epsilon - \delta}{\sqrt{1-\delta^2}} \ . \tag{9.7}$$

That is, the above is the same matrix as $M^2_{\rm St}$ with ϵ replaced by $\bar{\epsilon}$. However the coupling g_Y which appears in the covariant derivative is now given by $g_Y = \gamma\sqrt{(1-\delta^2)(1+\bar{\epsilon}^2)}$, where as before g_Y is subject to the constraint $1/e^2 = 1/g_2^2 + 1/\gamma^2$. The interactions in the diagonal basis are transformed through the same product $\mathcal{B} = \mathcal{KOR}$. Remarkably, the interactions of the Z and Z' with the visible sector matter fields depend

on $\bar{\epsilon}$ and not another combination depending on δ. However the HS interactions do depend sensitively on δ through the transformation of C_μ as we will discuss shortly. It is useful before proceeding further to discuss the origin of milli charges in the Stueckelberg models vs models which just kinetic mixing and 2 massless modes.

9.2 On the Origin of Milli-Charged Matter

In this subsection we illustrate the mechanism which generates the milli-charge in the context of this work. We start with the kinetic mixing model [181] with two gauge fields $A_{1\mu}, A_{2\mu}$ corresponding to the gauge groups $U(1)$ and $U(1)'$. We consider the following simple Lagrangian $\mathcal{L} = \mathcal{L}_0 + \mathcal{L}_1$ where

$$\mathcal{L}_0 \;=\; -\frac{1}{4}F_{1\mu\nu}F_1^{\mu\nu} - \frac{1}{4}F_{2\mu\nu}F_2^{\mu\nu} - \frac{\delta}{2}F_{1\mu\nu}F_2^{\mu\nu}, \qquad \mathcal{L}_1 = J'_\mu A_1^\mu + J_\mu A_2^\mu. \tag{9.8}$$

To put the kinetic energy term in its canonical form, one may use the transformation

$$\begin{bmatrix} A_1^\mu \\ A_2^\mu \end{bmatrix} \to K_0 \begin{bmatrix} A'^\mu \\ A^\mu \end{bmatrix}, \quad K_0 = \begin{bmatrix} \frac{1}{\sqrt{1-\delta^2}} & 0 \\ \frac{-\delta}{\sqrt{1-\delta^2}} & 1 \end{bmatrix}. \tag{9.9}$$

However, the transformation that canonically diagonalizes the kinetic energy is not unique. Thus, for example, $K = K_0 R_2$ instead of K_0 would do as well where R_2 is an orthogonal matrix

$$R_2 = \begin{bmatrix} \cos\theta & -\sin\theta \\ \sin\theta & \cos\theta \end{bmatrix}. \tag{9.10}$$

Here $\mathcal{L}_1$ is given by

$$\mathcal{L}_1 = A'^\mu \left[c_\theta C_\delta J'_\mu + (s_\theta - c_\theta S_\delta)\, J_\mu\right] + A^\mu \left[-s_\theta C_\delta J'_\mu + (c_\theta + s_\theta S_\delta)\, J_\mu\right]. \tag{9.11}$$

In this case we see that each of the massless states interacts with the sources J and J'. However, one may choose θ to get asymmetric solutions. For instance for the case $\theta = \arctan\left[\delta/\sqrt{1-\delta^2}\right]$ one has

$$\mathcal{L}_1 = A^\mu \left[\frac{1}{\sqrt{1-\delta^2}} J_\mu - \frac{\delta}{\sqrt{1-\delta^2}} J'_\mu\right] + A'^\mu J'_\mu. \tag{9.12}$$

In this case while A' interacts only with the source J', A interacts with both J and J', with the coupling to the source J' proportional to the kinetic mixing parameter δ. We identify A with the physical photon field, J with the physical source arising from quarks and leptons, while A' is the orthogonal massless state, and J' is the source in the hidden sector. Here the coupling of the photon with the hidden sector is proportional to δ and thus the hidden sector is milli-charged if δ is small.

Next we consider a model with kinetic mixing where a Stueckelberg mechanism generates a mass term of the type considered in Eq. (9.1)

$$\mathcal{L}_{\rm Mass} = -\frac{1}{2} M_1^2 A_{1\mu} A_1^\mu - \frac{1}{2} M_2^2 A_{2\mu} A_2^\mu - M_1 M_2 A_{1\mu} A_2^\mu. \tag{9.13}$$

In this case diagonalizaton of the mass matrix fixes θ so that

$$\theta = \arctan\left[\frac{\epsilon\sqrt{1-\delta^2}}{1-\delta\epsilon}\right], \tag{9.14}$$

and the interaction Lagrangian is given by

$$\begin{aligned} \mathcal{L}_1 &= \frac{1}{\sqrt{1-2\delta\epsilon+\epsilon^2}} \left(\frac{\epsilon-\delta}{\sqrt{1-\delta^2}} J_\mu + \frac{1-\delta\epsilon}{\sqrt{1-\delta^2}} J'_\mu\right) A_M^\mu \\ &+ \frac{1}{\sqrt{1-2\delta\epsilon+\epsilon^2}} \left(J_\mu - \epsilon J'_\mu\right) A_\gamma^\mu. \end{aligned} \tag{9.15}$$

Here for the case $\epsilon = 0$ one finds that the massless state, the photon A_γ^μ, no longer

couples with the hidden sector, while the massive mode A^{μ}_{M} couples with both the visible sector via J and with the hidden sector via J'. We conclude, therefore, that in the absence of the Stueckelberg mass mixing, for the case when only one mode is massless, there are no milli-charged particles coupled to the photon field. Thus the milli-charged couplings to the photon appear in this case only when the Stueckelberg mixing parameter ϵ is introduced. Therefore for the case when only one mode is massless the kinetic mixing by itself does not allow milli-charged couplings to the photon but the Stueckelberg mass mixing model does.

9.3 Constraints from Electroweak Data

We discuss now the constraints on the StkSM model of Sec.(9.1) with both mass mixing and kinetic mixing from the precision electroweak data. We start by assuming that the hidden sector does not contain matter, and the case when matter is included in the hidden sector is discussed in Sec.(9.4). To obtain the allowed range of ϵ and δ, we follow the same approach as in Ref. [188, 170, 171], that is, the first constraint comes from the comparison of the one sigma error in the prediction of the Z boson mass in the Standard Model and a comparison of this result with experiment leads to an error corridor, $\delta M_Z \sim 37$ MeV, where one can accommodate new physics. However, the more stringent constraint comes from fits to the high precision LEP data on the branching ratios of the Z decay and from the various asymmetries at the Z pole, when one demands that the χ^2 fits of StkSM are within 1% of that of the Standard Model. We will refer to this as the LEPI 1% constraint in the rest of the analysis. To investigate these implications on the precisely determined observables in the electroweak sector, we follow closely the analysis of the LEP Working Group [191] (see also Refs. [200, 244]), except that we will use the vector (v_f) and the axial vector

(a_f) couplings for the fermions in the StSM. The couplings of the Z to the fermions in the StkSM are elevated from the tree level expressions of Eqs.(7.8, 7.9) (with $\epsilon \to \bar{\epsilon}$) to $a_f \to \sqrt{\rho_f} a_f$, and $v_f \to \sqrt{\rho_f} v_f$, which contains Q_f which is modified to $Q_f \to \kappa_f Q_f$. Here ρ_f and κ_f (in general complex valued quantities) contain radiative corrections from propagator self energies and flavor specific vertex corrections and are as defined in Refs. [245, 191]. The decay of the Z boson into lepton anti-lepton and quark anti-quark pairs (excluding the top) in the on-shell renormalization scheme is given by [200, 245]

$$\begin{aligned}
\Gamma(Z \to f\bar{f}) &= N_f^c \mathcal{R}_f \Gamma_o \sqrt{1-4\mu_f^2}\left[|v_f|^2(1+2\mu_f^2) + |a_f|^2(1-4\mu_f^2)\right], && (9.16)\\
\mathcal{R}_f &= \left(1+\delta_f^{QED}\right)\left(1+\frac{N_f^c-1}{2}\delta_f^{QCD}\right), && (9.17)\\
\delta_f^{QED} &= \frac{3\alpha}{4\pi}Q_f^2, && (9.18)\\
\delta_f^{QCD} &= \frac{\alpha_s}{\pi} + 1.409\left(\frac{\alpha_s}{\pi}\right)^2 - 12.77\left(\frac{\alpha_s}{\pi}\right)^3 - Q_f^2\frac{\alpha\alpha_s}{4\pi^2}. && (9.19)
\end{aligned}$$

Here α and α_s are taken at the M_Z scale, while $N_f^c = (1,3)$ for leptons and quarks. In the above, $\Gamma_o = G_F M_Z^3/6\sqrt{2}\pi$, and $\mu_f = m_f/M_Z$. The total decay width (Γ_Z) of the Z into quarks and leptons, in the visible sector, is just the sum over all the final states. We also investigate the effects of mixing with the Stueckelberg sector on the following Z pole observables

$$\begin{aligned}
R_l &= \frac{\Gamma(had)}{\Gamma(l^+l^-)}, \qquad R_q = \frac{\Gamma(q\bar{q})}{\Gamma(had)} && (9.20)\\
\sigma_{had} &= \frac{12\pi\Gamma(e^+e^-)\Gamma(had)}{M_Z^2\Gamma_Z^2}, && (9.21)\\
A_f &= \frac{2v_f a_f}{v_f^2+a_f^2}, \qquad A_{FB}^{(0,f)} = \frac{3}{4}A_e A_f. && (9.22)
\end{aligned}$$

Table 9.1: Fits to 19 Z pole observables. Column 2 is given by the PDG [222], while the data in column 3 is from the SM Fit of the LEP EWWG [191]. The column labeled St Fit is an analysis for the input $\epsilon = 0.06$, $\delta = 0.03$, and $M_1 = 200$ GeV. In the last column PULL is defined by $(\text{Experiment} - \text{FIT})/\Delta$, and $\chi^2 = \sum \text{PULL}^2$. (From [174], see also [170, 171].)

Quantity	Experiment $\pm\Delta$	LEP FIT	St FIT	LEP PULL	St PULL
Γ_Z [GeV]	2.4952 ± 0.0023	2.4956	2.4956	-0.17	-0.17
σ_{had} [nb]	41.541 ± 0.037	41.476	41.469	1.76	1.95
R_e	20.804 ± 0.050	20.744	20.750	1.20	1.08
R_μ	20.785 ± 0.033	20.745	20.750	1.21	1.06
R_τ	20.764 ± 0.045	20.792	20.796	-0.62	-0.71
R_b	0.21643 ± 0.00072	0.21583	0.21576	0.83	0.93
R_c	0.1686 ± 0.0047	0.17225	0.17111	-0.78	-0.53
$A_{FB}^{(0,e)}$	0.0145 ± 0.0025	0.01627	0.01633	-0.71	-0.73
$A_{FB}^{(0,\mu)}$	0.0169 ± 0.0013	0.01627	0.01633	0.48	0.44
$A_{FB}^{(0,\tau)}$	0.0188 ± 0.0017	0.01627	0.01633	1.49	1.45
$A_{FB}^{(0,b)}$	0.0991 ± 0.0016	0.10324	0.10344	-2.59	-2.71
$A_{FB}^{(0,c)}$	0.0708 ± 0.0035	0.07378	0.07394	-0.85	-0.90
$A_{FB}^{(0,s)}$	0.098 ± 0.011	0.10335	0.10355	-0.49	-0.50
A_e	0.1515 ± 0.0019	0.1473	0.1476	2.21	2.05
A_μ	0.142 ± 0.015	0.1473	0.1476	-0.35	-0.37
A_τ	0.143 ± 0.004	0.1473	0.1476	-1.08	-1.15
A_b	0.923 ± 0.020	0.93462	0.93464	-0.58	-0.58
A_c	0.671 ± 0.027	0.66798	0.66812	0.11	0.11
A_s	0.895 ± 0.091	0.93569	0.93571	-0.45	-0.45
				χ^2 =25.0	χ^2 =25.2

Using the above we have carried out a fit in the electroweak sector on the quantities sensitive to mixing with the Stueckelberg sector. A summary of the analysis is presented in Table(9.1) for a specific point in the Stueckelberg parameter space with $\epsilon = .06$, $\delta = .03$, and $M_{Z'} \approx M_1 = 200$ GeV. In the analysis we have taken into account the constraint between g_Y and g_Y^{SM} and the inclusion of this constraint improves the electroweak fits over that of previous analyses for the case $\delta = 0$ [170, 171]. Thus the analysis of Table(9.1) shows that in the StkSM one finds χ^2 fits which are at the same level as in the SM. An analysis of χ^2 in the LEPI fits in the $\epsilon - \delta$ parameter space is given in Fig.(9.1). Specifically Fig.(9.1) shows that a large region of the pa-

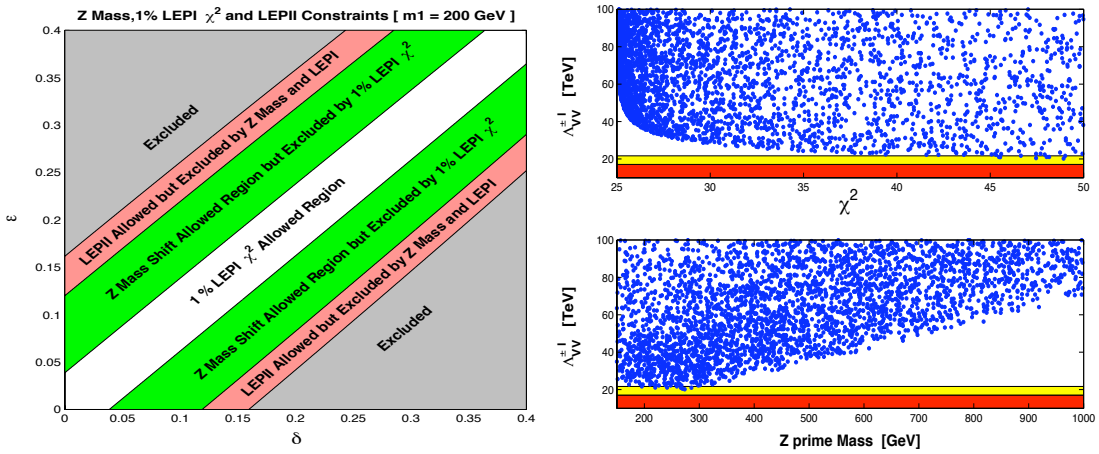

Figure 9.1: Left: An analysis of χ^2 in StkSM model in the $\epsilon - \delta$ plane. The center white region is where χ^2 of the StkSM model is within 1% of the SM fits. Along the line $\epsilon = \delta$ the Z' decouples and the model gives the same χ^2 fit to data as in the SM Right: The plots give an analysis of the LEPII constraint. The upper plot, which has a Z' mass range of $.2 - 1$ TeV, shows the relevant LEPII contact interaction parameter $\Lambda^{\pm l}_{VV}$ as a function of χ^2 for the 19 observable of Table(9.1), where a $\chi^2 \sim 25$ is the SM fit as given in Table(9.1), and where the (yellow,red) shaded regions correspond to $\Lambda^{\pm l}_{VV} = (21.7,\ 17.1)$ TeV [246]. The lower plot for χ^2 in the range (25-50) gives $\Lambda^{\pm l}_{VV}$ as a function of the Z prime mass. (From [174].)

rameter space can satisfy the LEPI 1% constraint. A striking aspect of the analysis of Fig.(9.1) is that this constraint is satisfied even though ϵ and δ can get significantly large, as long as $(\epsilon - \delta)$ is small. The physics of this apparent from the form of $\bar{\epsilon}$, which governs the fit, as in the absence of matter in the hidden sector, there is only one effective parameter, $\bar{\epsilon}$, that enters the analysis of electroweak physics. We discuss next the LEPII constraints. These constraints are typically characterized by the parameter of contact interaction Λ, and the LEPII group finds that $\Lambda_{VV} > (21.7, 17.1)$ TeV [246] to be the most constraining. The StkSM model predicts the theoretical value of Λ_{VV} through the following formula

$$\Lambda_{VV} = \frac{M_{Z'}}{M_Z}\sqrt{\frac{4\pi}{\sqrt{2}G_F v_e'^2}}. \tag{9.23}$$

A numerical analysis of the LEPII constraints is given in Fig.(9.1). The analysis of Fig.(9.1) exhibits that the LEPI 1% constraint is more stringent than the LEPII constraint, and thus the LEPII constraint is automatically satisfied once the LEPI 1% constraint is satisfied. This result is supported by the analysis of Fig.(9.1) which shows that the value of Λ_{VV} predicted by the model in the parameter space consistent with the LEPI 1% constraint is significantly larger than the lower limit of the LEPII constraint. The blue points that enter the shaded regions are eliminated by the LEPII constraint. However, these points also correspond to large χ^2 fits to the LEPI analysis and are eliminated by LEPI 1% constraint as well. Thus, for a narrow Z', the LEPI 1% constraint is stronger than the LEPII constraint.

9.4 Milli-charged DM from the Hidden Sector

In the previous section we did not include matter in the hidden sector which is defined as matter which is neutral under the SM gauge group but carries $U(1)_X$ quantum numbers and thus couples only to C_μ. The kinetic and mass mixings in the $U(1)_X \times U(1)_Y$ sectors typically generate milli-charges for such matter. The conditions for the origin of milli-charges arising from such mixings were discussed in Sec.(9.2), where simple examples were worked out to explain how such charges appear [1]. Here we consider the milli-charged matter in the hidden sector within the context of the Stueckelberg extension of the SM with both mass and kinetic mixing. If milli-charged matter exists then both the Z and the Z' can decay into it if kinematically allowed to do so. For the mass scales we investigate the milli-charge particle has a mass larger than $M_Z/2$. In this case all of the electroweak constraints discussed in the previous

[1] For a recent sample of experimental constraints on milli-charged dark matter see [247],[173] and figure 1 of [248]; it suffices to point out, that consistent with the above works, our dark matter candidate avoids constraints on milli-charged dark matter as its couplings are extra weak and its mass is rather large in the several hundred GeV range.

sections are unaffected. Further, the Z prime can decay into the milli-charged matter if the mass of the hidden matter is less than $M_{Z'}/2$. Such decays increase the Z' width and thus decrease the branching ratios of the Z' decay into the visible sector which depletes the di-lepton signal in the Drell-Yan process. A relatively strong di-lepton signal manifests in the analysis of Refs. [169, 170, 171] where the Z' decays into the hidden sector were taken to be comparable to the Z' decays into the visible sector, i.e., $\Gamma_{Z'}^{\rm hid} \sim \Gamma_{Z'}^{\rm vis}$. This constraint then leads to a sharp Z' resonance as discussed in detail already.

The recent work of Ref. [173] has carried out an explicit analysis of putting a pair of Dirac fermions in the hidden sector, and made the interesting observation that for values $g_X Q_X \leq O(1)$ the decay width of Z' into the hidden sector Dirac fermions (χ) can be of GeV size, and consequently the hidden matter can annihilate in sufficient amounts to satisfy relic density constraints. We have carried out a similar analysis using the thermal averaging procedure in the computation of the relic density. Our conclusions are in agreement with the analysis of Ref. [173] in the region of the parameter space investigated in Ref. [173] when no kinetic mixing is assumed in the absence of thermal averaging. In our work we take the kinetic mixing into account in the analysis of the relic density. We also make a further observation that there exists a significant region of the parameter space where it is possible to satisfy the relic density constraints and still have a narrow Z' resonance which can be detected at the Tevatron and at the LHC using the di-lepton signal via a Drell-Yan process.

We give now further details of our relic density analysis. The interaction between the fermions of the SM and 3 Bosons are

$$\mathcal{L}_{\rm int}^{\rm VS} = \bar{f}\gamma^\mu \left[(C_{f_L}^{Z'} P_L + C_{f_R}^{Z'} P_R) Z'_\mu + \left(C_{f_L}^{Z} P_L + C_{f_R}^{Z} P_R \right) Z_\mu + e Q_f A_\mu \right] f, \quad (9.24)$$

where as before $Q = T^3_{L,R} + Y_{L,R}/2$, $T^3_R = 0$, with $P_{L,R} = \frac{1}{2}(1 \mp \gamma^5)$. For the Visible Sector (VS) we have ($Z_1 = Z'$ and $Z_2 = Z$ and $\mathcal{R}$ diagonalizes $\mathcal{M}^2$)

$$C^{Z_i}_{f_L} = T_{3L}\left[g_2\mathcal{R}_{3i} - \gamma\sqrt{1+\bar{\epsilon}^2}\mathcal{R}_{2i}\right], \qquad C^{Z}_{f_R} = Q\gamma\sqrt{1+\bar{\epsilon}^2}\mathcal{R}_{2i}. \tag{9.25}$$

For the Hidden Sector (HS) we have

$$\mathcal{L}^{\rm HS}_{\rm int} = \bar{\chi}\gamma^\mu\left[C^{Z'}_\chi Z'_\mu + C^Z_\chi Z_\mu + C^\gamma_\chi A^\gamma_\mu\right]\chi. \tag{9.26}$$

The rotation matrix which diagonalizes $\mathcal{M}^2$ depends on one combination of ϵ and δ through $\bar{\epsilon}$. One can use the parametrization of Eq.(7.3),that is, the rotation matrix $R_{ij}(\epsilon, M_1) \to \mathcal{R}_{i,j}(\bar{\epsilon})$, where we remind that $\bar{\epsilon} = (\epsilon - \delta)(1-\delta^2)^{-1/2}$ with $\epsilon = M_2/M_1$. For the HS we have

$$\begin{aligned}
C^\gamma_\chi &= g_X Q_X\Big[-c_\theta s_\phi - S_\delta c_\theta c_\phi\Big] \\
C^Z_\chi &= g_X Q_X\Big[s_\psi c_\phi + s_\theta s_\phi c_\psi - S_\delta(s_\psi s_\phi - s_\theta c_\phi c_\psi)\Big] \\
C^{Z'}_\chi &= g_X Q_X\Big[c_\psi c_\phi - s_\theta s_\phi s_\psi - S_\delta(c_\psi s_\phi + s_\theta c_\phi s_\psi)\Big],
\end{aligned} \tag{9.27}$$

with $S_\delta = \delta/\sqrt{1-\delta^2}$ and the angles are a function of $\bar{\epsilon}$. The action given in [167, 168, 169] leads to an integrated cross section[173],

$$\sigma_{f\bar{f}} \simeq \frac{N_f s}{32\pi}\frac{\beta_f}{\beta_\chi}[(|\xi_L|^2 + |\xi_R|^2)\cdot F_1 + Re(\xi^*_L\xi_R)\cdot F_2], \tag{9.28}$$

where $F_1 = 1 + \beta^2_\chi\beta^2_f/3 + 4M^2_\chi s^{-1}\left(1 - 2m^2_f/s\right)$, and $F_2 = 8m^2_f s^{-1}\left(1 + 2M^2_\chi/s\right)$. Here $\beta_{f,\chi} = (1 - 4m^2_{f,\chi}/s)^{1/2}$, $s = 4m^2_\chi/(1 - v^2/4)$ and $\xi_{L,R}$ include the poles

$$\xi_{L,R} = \frac{C^\gamma_\chi eQ}{s} + \frac{C^Z_\chi C^Z_{f_{L,R}}}{s - M^2_Z + i\Gamma_Z M_Z} + \frac{C^{Z'}_\chi C^{Z'}_{f_{L,R}}}{s - M^2_{Z'} + i\Gamma_{Z'}M_{Z'}}.$$

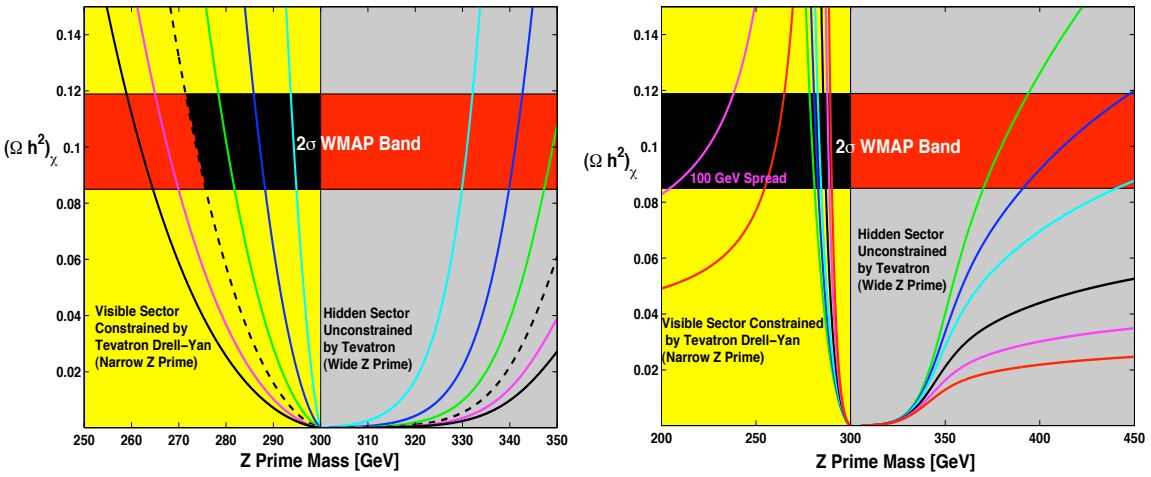

Figure 9.2: An analysis of the relic density of milli-charged particles arising in the StSM and StkSM for $M_\chi = 150$ GeV. (From [174].)

The relic density may now be computed following the techniques outlined in [174]. The analysis of the relic density as a function of $M_{Z'}$ for the case $M_\chi = 150$ GeV, and ϵ in the range $(0.01 - 0.06)$, $g_X = g_Y^{SM}$ and $Q_X = 1$ can be seen in Fig.(9.2)(left panel). Here one finds that the relic density is satisfied on two branches, one for $M_{Z'} > 2M_\chi$, and the other for $M_{Z'} < 2M_\chi$. The (yellow, grey) regions ($M_{Z'} < 2M_\chi$, $M_{Z'} > 2M_\chi$) correspond to a (narrow, broad) Z' resonance, and the WMAP-3 relic density constraints are satisfied for both a broad Z' resonance and a narrow Z' resonance as exhibited by the 2σ WMAP-3 red and black bands. The region of narrow Z' resonance is constrained by the LEP and Tevatron data. The region in the 2σ WMAP-3 band can be probed via a di-lepton signal. The red band to the left is excluded by the CDF 95% C.L. [249] data while the black band is consistent or on the edge thereof, with all constraints which can produce an observable di-lepton signal. In Fig.(9.2)(right panel) an analysis is given of the relic density of milli-charged particles for the case when kinetic mixing is included in the Stueckelberg Z' model. The analysis is done for $M_\chi = 150$ GeV, $\bar{\epsilon} = .04$, and $\delta = (.05, .075, .10, .15, .20, .25)$, where the values are in descending order for $M_{Z'} > 300$ GeV. The red and black bands are the WMAP-3

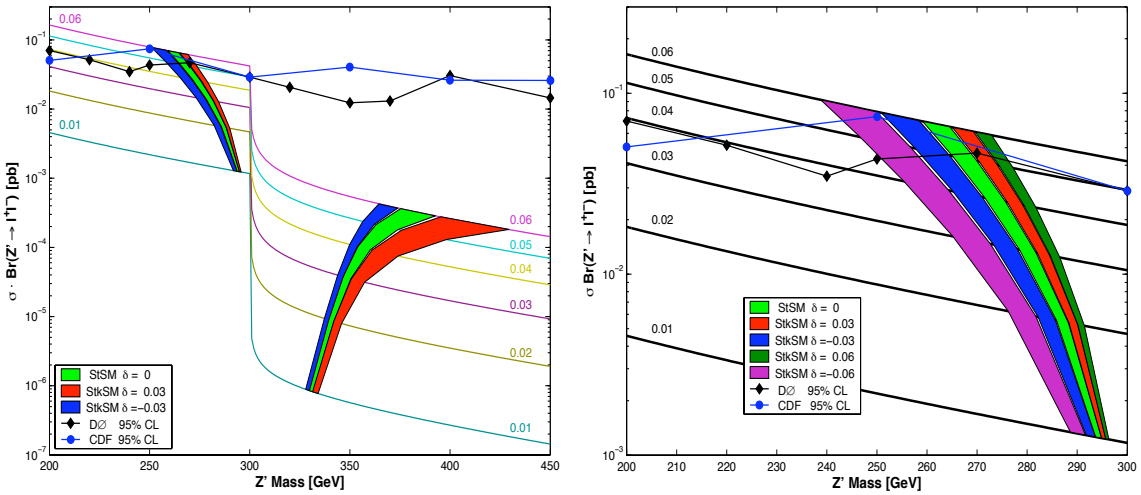

Figure 9.3: $\sigma \cdot Br(Z' \to l^+l^-)$ at the Tevatron consistent with the WMAP-3 relic density constraint (shaded regions) as a function of $M_{Z'}$ for $M_\chi = 150$ GeV. (From [174].)

constraints where the black band also produces an observable di-lepton signal. The analysis shows that for $\bar{\epsilon}$ fixed, increasing δ increases the parameter space where the WMAP-3 relic density constraint is satisfied, while allowing for a detectable Z prime signal. Thus An analysis of the di-lepton signal for this case is also given in shows that the Drell-Yan signal $p\bar{p} \to Z' \to e^+e^-$ is enormously enhanced for $M_{Z'} < 2M_\chi$. Thus we have a region here of the parameter space where one will have a sharp resonance giving a visible di-lepton signal while at the same time producing milli-charge dark matter consistent with WMAP-3. Specifically, Fig.(9.3)(left panel) exhibits the di-lepton signal $\sigma \cdot Br(Z' \to l^+l^-)$ at the Tevatron consistent with the WMAP-3 relic density constraint as a function of $M_{Z'}$ when $2M_\chi = 300$ GeV. The curves in ascending order are for values of $\bar{\epsilon}$ in the range $(0.01 - 0.06)$ in steps of 0.01. The di-lepton signal has a dramatic fall as $M_{Z'}$ crosses the point $2M_\chi = 300$ GeV where the Z' decay into the hidden sector fermions is kinematically allowed, widening enormously the Z' decay width. The green shaded regions are where the WMAP-3 relic density constraints are satisfied for the case when there is no kinetic mixing. Red and blue regions are for the case when kinetic mixing is included. The DØ data set [204] and

CDF [249] data sets are shown. Note that the two constraints are roughly equivalent in terms of limiting the parameter space and are therefore indeed complimentary as discussed previously. Fig.(9.3)(right panel) shows the region with a detectable di-lepton signal at the Tevatron is exhibited but additional δ values are included in the analysis. The plots show that the region allowed by WMAP-3 constraints moves to the right for positive δ and to the left for negative δ. The inclusion of kinetic mixing is seen to enlarge the parameter space where the relic density constraints are satisfied and where an observable di-lepton signal at the Tevatron can occur.

An interesting issue concerns the question regarding how small $\bar{\epsilon}$ can be for WMAP-3 relic density constraints to be satisfied. In the analysis of [174] satisfaction of the relic density in for the case $\bar{\epsilon} = 10^{-4}$ was found and even smaller $\bar{\epsilon}$ were found admissible, however this requires extreme fine tuning to satisfy the relic density constraint. Further, while the di-lepton signal at the Tevatron in this case will be suppressed, it could still be visible at the LHC with sufficient luminosity.

Finally, we note that within the context of the Stueckelberg model it is possible to place indirect limits on the milli-charge coupling of hidden sector fermion with the photon from the Tevatron data. An analysis of the limits on the Stueckelberg mixing parameter ϵ was presented in [170] for the case $\delta = 0$. For this case, the milli-charge Q_{milli}, where $Q_{milli}e$ is the coupling of the photon with the hidden sector fermions is determined to be: $Q_{milli} \approx \epsilon$. Thus one may directly translate the limits obtained in [170] to limits on the milli-charged coupling of the hidden fermion with the photon. In the context of the present analysis, the cross-section predictions given here, (as for example, in Fig.(9.3)) with their overlapping WMAP-3 bands, shows this explicitly.

9.5 PAMELA/ATIC & Breit-Wigner Enhancement

In the previous section we discussed how the Stueckelberg model satisfies the WMAP data in the vicinity of the Z prime pole [174]. Here we show that in the same region of parameter space where the relic density is satisifed, the presence of the pole i.e. the Breit-Wigner, leads to the so-called Breit-Wigner Enhancement[251] of the Halo cross section that can fit both the recent PAMELA[250][2] and ATIC[252][3] data.

It is well known that cosmic ray nuclei interact with interstellar gaseous matter to produce positrons, however very recently PAMELA has reported a large excess of positrons between the mass range 1.5 to 100 GeV, identifying nearly 10,000 postirons in this mass range, which leads to a positron fraction well above the expectations from secondary sources[250]. Such an excess has been previously observed in other experiments (for example the HEAT and AMS experiments [253]) with very large error bars, however the results reported by PAMELA have strengthed the previous reports with a much more precise determination of the the positron fraction.

An analysis of this positron excess is given here in the framework of the Stueckelberg extension of the Standard Model which includes an extra $U(1)_X$ gauge field and matter in the hidden sector. As we have already discussed, such matter can produce the right amount of dark matter consistent with the WMAP constraints. Assuming the hidden sector matter to be composed of Dirac fermions it is shown that their annihilation can produce the positron excess with the right positron energy dependence seen in the HEAT, AMS and the PAMELA experiments. It is also found that the predictions of the $\bar{p}/p$ flux ratio can fit the data, and that the excess in cosmic ray leptons seen in the ATIC data, with the largest excess reported at a mass ~ 700 GeV, can also be accommodated in this model.

[2]PAMELA $\equiv$ Payload Anti-matter Matter Exploration and Light-Nuclei Astrophysics (satellite)
[3]ATIC $\equiv$ Advanced Thin Ionization Calorimeter (balloon)

A remarkable feature of the PAMELA positron spectrum is the turn around and increase in the positron flux with positron energy in the range of 10-80 GeV. The analysis of the positron spectrum depends both on the particle physics as well as on the astrophysical models and these features have been discussed recently in some detail in [254], [255, 256]. Recent works on fits to the data have been presented [257], [251], [258] [indeed the recent results from the PAMELA experiment have lead to a surge of papers, a nearly complete list of papers (at the present moment) can be found in [259]].

Here we focus on the fit to the recently released data by the PAMELA and ATIC experiments from annihilation of dark matter in the hidden sector in the framework of Stueckelberg extension of the Standard Model [251]. We give now the details of the analysis. In general the positron flux arising from the annihilation of dark matter (DM) particles is given by [255, 256]

$$\Phi_{e^+} = \frac{\eta B v_{e^+}}{4\pi b(E)} \frac{\rho^2}{M_{\rm DM}^2} \int_E^{M_D} \sum_k \langle \sigma v \rangle_{kH} \left(\frac{dN_{e^+}}{dE'} \right)_k \mathcal{I}_{(E,E')} dE' \tag{9.29}$$

where $M_{\rm DM}$ is the mass of the dark matter particle (here χ), $\eta = 1/2(1/4)$ for the DM particle being Majorana or Dirac[255], B is the boost factor which is expected to lie in the range (2-10) although significantly larger values have been used in the literature. In the above v_{e^+} is the positron velocity where $v_{e^+} \sim c$, and ρ is the local dark matter density in the halo so that ρ lies in the range $(0.2 - 0.7)[\mathrm{GeV/cm^3}]$ [260]. Further, $b(E)$ in Eq.(9.29) is given by [261, 262] $b(E) = E_0(E/E_0)^2/\tau_E$, where $\tau_E \sim 10^{16}$[s], with E in [GeV] and $E_0 \equiv 1$GeV. Here $\langle \sigma v \rangle_H$ is the velocity averaged cross section in the *Halo (H) of the galaxy* as emphasized by the subscript H.

In some works $\langle \sigma v \rangle_H$ is replaced by the $\langle \sigma v \rangle_{X_f}$ at the freeze-out temperature. However, such an approximation can lead to significant errors since the ratio $\langle \sigma v \rangle_H / \langle \sigma v \rangle_{X_f}$

can deviate significantly from unity depending on the part of the parameter space one is in. This point was emphasized in [251]. The halo function $\mathcal{I}_{(E,E')}$ is parametrized as in [256], and we consider both the NFW and Moore [263] profiles coupled with various diffusion models.

Generally, the positron flux can arise from multiple final state channels from the annhilations of DM. Here we consider Dirac Dark matter [169, 173, 174, 175] which annihilates via $\chi\bar{\chi} \to f\bar{f}, W^+W^-, \ldots$ where f is any quark or lepton final state of the standard model. In the parameter space investigated here, the dominant source of positrons arises from the direct channel via the Z' pole. As has been discussed in the Ch.(7), the W^+W^- final state contribution is much suppressed relative to the $f\bar{f}$ final state contribution[170]. Therefore, the dominant term in our analysis is the line source arising from the annihilation $\chi\bar{\chi} \to Z' \to e^+e^-$ and in this case one has $\sum_{F=\text{Final states}} \langle\sigma v\rangle_F \left(dN_{e^+}/dE'\right)_F \sim \langle\sigma v\rangle_{e^+e^-}\delta(E' - M_\chi) + \ldots$, where the dots stand for the background terms that contribute to the continuum flux. The continuum flux arises mostly from muons and to a much lesser degree from taus[264]. Defining R_f as the positron ratio from source f one finds $R_\mu/R_e \sim [0.90 - 1.01E_{e^+}/M_{\rm DM}]\theta(M_{\rm DM} - E_e^+)$, provides a good approximation to the muon fraction over the dark matter (DM) mass range of interest and a similar relation holds for the taus[264]. The inclusion of the flux from the continuum reduces the needed boost factor slightly, however the line source still dominates at high energies. The use of the above in Eq.(9.29) yields the primary positron flux $\Phi_{e^+} \equiv \Phi_{e^+}^{(\rm prim)}$. The background fluxes have been approximated in Refs. [265, 266], and they are given by

$$\begin{aligned}
\Phi_{e^-}^{\rm prim}(E) &= \frac{0.16E^{-1.1}}{1 + 11E^{0.9} + 3.2E^{2.15}} \quad \text{GeV}^{-1}\text{cm}^{-2}\text{sec}^{-1}\text{sr}^{-1}, \\
\Phi_{e^-}^{\rm sec}(E) &= \frac{0.7E^{0.7}}{1 + 110E^{1.5} + 600E^{2.9} + 580E^{4.2}} \quad \text{GeV}^{-1}\text{cm}^{-2}\text{sec}^{-1}\text{sr}^{-1},
\end{aligned}$$

$$\Phi^{\rm sec}_{e^+}(E) \;=\; \frac{4.5E^{0.7}}{1+650E^{2.3}+1500E^{4.2}} \quad {\rm GeV}^{-1}{\rm cm}^{-2}{\rm sec}^{-1}{\rm sr}^{-1}\ . \tag{9.30}$$

The fraction of e^+ flux is then

$$\frac{\Phi^{\rm prim}_{e+}+\Phi^{\rm sec}_{e+}}{\Phi^{\rm prim}_{e+}+\Phi^{sec}_{e+}+\Phi^{\rm prim}_{e^-}+\Phi^{\rm sec}_{e^-}}\ . \tag{9.31}$$

An analysis is given of this observable as a function of the positron energy in Fig.(9.4) for the Stueckelberg Z' model. One finds that the annihilation of Dirac fermions via the Z' pole into $e^+e^- + \mu^+\mu^-$ gives a sufficient kick to generate the necessary turn around in the positron fraction at just about the desired value of the positron energy consistent with the relic density constraints. The analysis of Fig.(9.4) (left panel) exhibits the theoretical evaluation for several model points. Here we consider NFW min (M2), med and max (M1) as well as the Moore max (M1) parametrizations for the Halo models[255, 256]. One finds that there is a significant variation in the prediction depending on the profile/diffusion model one chooses. However, one finds that the PAMELA data does lie in the range of the theoretical predictions. We note in passing that the gamma ray spectrum in this model[167] has been discussed in[173]. The theoretical predictions cover a range which includes the PAMELA data[250]. Further, such a fit determines the dark matter fermion mass to be roughly half the Z' mass.

In Fig.(9.4) (right panel) we exhibit the dependence of $\langle\sigma v\rangle$ on temperature. The analysis shows that $\langle\sigma v\rangle$ can have a significant temperature dependence. Thus the simplifying assumption often made in assuming that $\langle\sigma v\rangle$ is a constant as one moves from the freeze-out temperature to the temperature of the galactic halo is erroneous. Specifically the analysis shows that the temperature dependence is model dependent and one can generate an enhancement of $\langle\sigma v\rangle_H$ in the halo relative to freeze-out

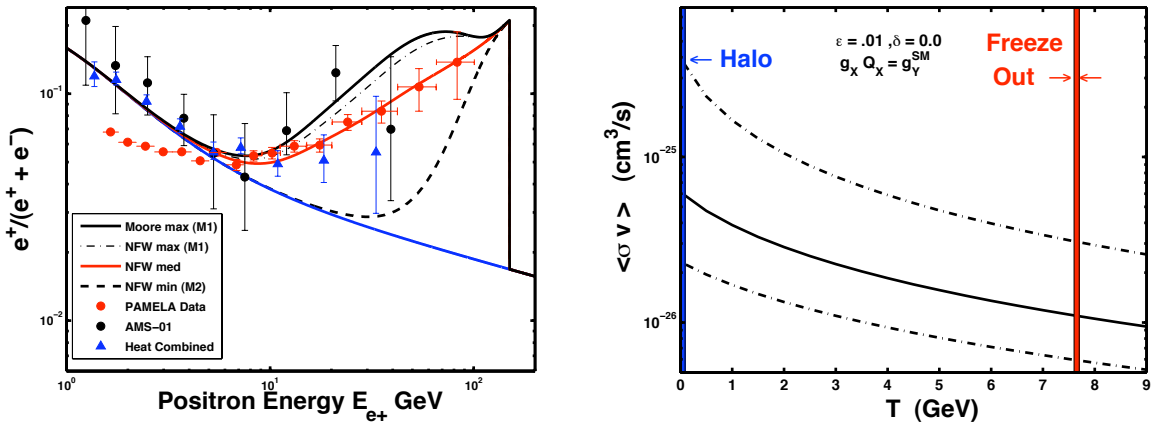

Figure 9.4: (Left Panel): Positron spectrum including the monochromatic source and continuum flux for various halo/diffusion models with ($\epsilon = 0.006, \delta = 0.00$) and $\rho = 0.35$ GeV/cm^3 with $M_{Z'} = 298$ GeV, $M_\chi = 150$ GeV, $\tau_E = 3 \times 10^{16}$s[261], and B=10; and $\Omega h^2 = 0.13$ (calculated by integration over the Breit-Wigner pole). Also plotted is the recently released PAMELA data [250], along with the AMS-01 and HEAT data [253]. The background flux ratio is the decaying curve (solid blue). (Right Panel): An exhibition of the dependence of $\langle\sigma v\rangle$ on temperature for Stueckelberg models as given in the figure with $M_\chi/\text{GeV} \in [150, 153]$ in steps of 1.5 and $M_{Z'}$ fixed as in the left panel. The annihilation near a pole generates a significant enhancement of $\langle\sigma v\rangle_H$ in the halo relative to $\langle\sigma v\rangle_{X_f}$ at freeze-out. The Breit-Wigner enhancement of $\langle\sigma v\rangle_H$ obviates the necessity of using very large boost factors. (From [251]).

$\langle\sigma v\rangle_{X_f}$ by as much as a factor of 10 or more depending on the part of the parameter space one is in. Typically the temperature dependence is enhanced when the dark matter particles annihilate near a pole from the Breit-Wigner which is the case in the analysis here. We note that the Breit-Wigner enhancement was first used in the analysis of [251]. Several papers followed suit.

The $\bar{p}/p$ flux ratio as recently reported by the PAMELA[267] collaboration indicates a smooth increase with energy up to about 10 GeV and then a flattening out in agreement with the background and with previous experiments. We note that a suppression of $\bar{p}/p$ flux ratio is possible in the model presented here. This is due in part because the $Z' \to W^+W^-$ is suppressed as already discussed. We have carried out a detailed analysis of the $\bar{p}/p$ flux ratio. Our analysis follows closely the work

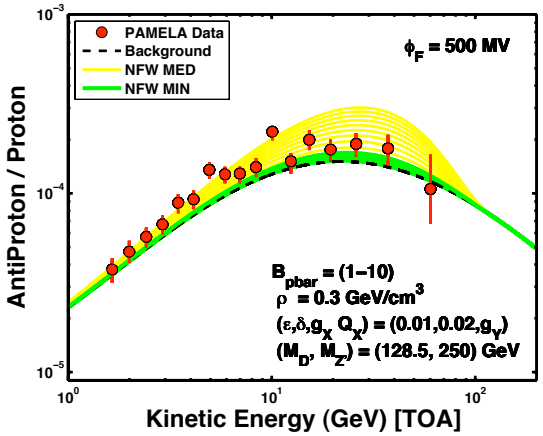

Figure 9.5: The $\bar{p}/p$ flux ratio including the TOA correction to the IS spectrum [268], and with $B_{\bar{p}} \in (1-10)$. The green (darker) curves (NFW min) are insensitive to the boost in the ratio, while the yellow (lighter) curves (NFW med) allow a boost as large as 5 or even larger. In the Figure, $M_D = M_\chi$. (From [251]).

of [256] with fragmentation functions as modeled in Bottino et al and by Bergstrom etal and $(p, \bar{p})$ backgrounds as in Donato et al and Bringmann et al [268]. The Interstellar (IS) flux has been modified for predictions at the Top of the Atmosphere (TOA) which suffers from large uncertainties. The results are given in Fig.(9.5) and compared with the recently reported results by the PAMELA collaboration. It is found that the $\bar{p}/p$ analysis of Fig.(9.5) is fully compatible with the recent PAMELA data. It is further observed that the NFW min profile, for the $\bar{p}/p$ predictions, are rather insensitive to a boost factor, while boost factors as large as 5 or larger are acceptable in the NFW med model. We note in passing that the $\bar{p}/p$ flux ratio does suffer from larger theoretical uncertainties than the e^+/e flux ratio due to a larger diffusion length. Further, it is known that local inhomogeneities in the dark matter density may lead to very different boost factors for positrons and anti-protons (see, for example, Lavalle etal in [268]).

In this work we have shown that the annihilation of the Dirac fermions in the hidden sector close to the Z' pole can generate a positron fraction compatible with the

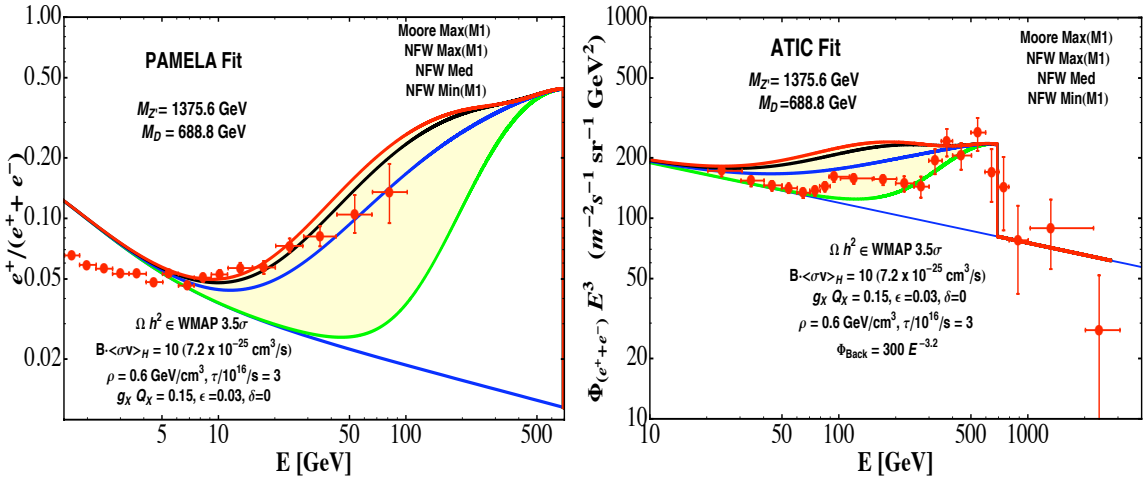

Figure 9.6: Fit to the PAMELA and ATIC[252] data for a heavy Dirac dark matter mass of 688.8 GeV with the Breit-Wigner enhancement. The curves in descending order are for the cases for the halo profiles listed on the top right hand corner. (From [251]).

current PAMELA data. Specifically the model produces the right amount of positron spectrum enhancement with increasing positron energy indicated by the AMS-01 and the HEAT data and confirmed by the PAMELA data, and additionally the model can accommodate the anti-proton constraints. In Fig.(9.5) we also give a simultaneous fit to both the ATIC and PAMELA data. Such a fit requires a larger dark matter mass, and the model can accommodate both excesses seen in these experiments. Further, the PAMELA data seems to favor the astrophysical scenario closer to the MED model, while the ATIC data seems to favor an scenario somewhat in between the MED and MIN models for the cases shown. A further support of the model can come from a direct observation of the Z' boson at the Large Hadron Collider.

9.6 Summary

In the above we have given an analysis of the Stueckelberg extension of the Standard Model with inclusion of the kinetic energy mixing in the $U(1)_X \times U(1)_Y$ sectors. Such kinetic mixings are quite generic in models with more than one $U(1)$ gauge group. It

is shown that in the model with both the mass and kinetic mixing and in the absence of matter in the hidden sector, the sensitive parameter which measures the deviation from the Standard Model is given by $\bar{\epsilon}$ which is a specific combination of ϵ and δ, where ϵ measures the mass mixing and δ measures the kinetic mixing. However, when matter in the hidden sector is taken into account, electroweak physics depends on both ϵ and δ. An analysis of the relic density of milli-charged dark matter which is generic in Stueckelberg extensions is given. Here our analysis is in agreement with the work of Ref. [173] for the case when no kinetic mixing is taken into account. Inclusion of the kinetic mixing is seen to increase the parameter space where the relic density constraints consistent with WMAP can be satisfied. We also analyze the Z' signal. As noted in Ref. [173] on the branch $M_{Z'} > 2M_{\chi}$ the di-lepton signal from the Z' decay is too small to be observed at colliders, and our results are in agreement with this analysis. However, we note that on the branch $M_{Z'} < 2M_{\chi}$, there is a significant parameter space where the relic density constraints can be satisfied and the di-lepton signal from the Z' decay via the Drell-Yan process is strong and observable at the Tevatron and at the LHC. The analysis also shows that relic density constraints can be satisfied for values of $\bar{\epsilon}$ as low as 10^{-4} and even smaller values are possible. Finally, we gave a detailed analysis of the positron excess seen in the PAMELA experiment, as well as the electron excess seen in the ATIC experiment. We found remarkably that the StKSM can fit both experiments in precisely the same region of the parameter space where the relic density is satisfied and where the di-lepton signal will be strong at the Tevatron and the LHC. It was found that the Halo cross section is enhanced significantly due to the presence of the Breit-Wigner resonance; our analysis was the first to show this phenomenon [175], and other analyses followed showing a similar effect. The model evades constraints on the $\bar{p}/p$ ratio due to enhanced leptonic branching fractions allowing MED/MIN models for DM a mass as low $\sim$150 GeV.

Chapter 10

Conclusions

The main focus of this Thesis was to make progress on the determination of the nature of fundamental physics beyond the the Standard Model of particle interactions. The analysis presented here was carried out within the framework of SUGRA unified models and models based on the $U(1)_X$ extensions of the Standard Model where mass generation arise through a mixed Higgs and Stueckelberg mechanism including the extended sector. The theoretical implications of these models were subject to currently known experimental constraints from both collider and dark matter experiments and predictions were made for new phenomena which arise in these models relevant to both current and future experiments. Summarized below are the main results and conclusions of this Thesis.

1. In Chapter (3) it was shown that collider data can be used to decode the mechanism for the production of dark matter in the early universe. For specificity the analysis was focused on a discrimination of the two prominent branches in the relic density analyses: the stau co-annihilation branch and the hyperbolic branch. It was shown that with a judicious choice of signals, namely P_T^{miss} distributions, a study of $\langle P_T^{miss} \rangle$ on these branches, cutting on the number of

jets in the events, by variable b-tagging, and correlating the signature events in heavy flavor channels, that the collider data can allow one to distinguish in a very clear way between the two branches where the dark matter may have originated in the early universe. The analysis also revealed a rather unexpected result, namely that essentially all of the hyperbolic branch is constituted of the model points in SUGRA models where the chargino is the NLSP beyond the neutralino LSP. Thus the dominant part of the hyperbolic branch sets up what may be interpreted as a Chargino Wall in the plane spanned by the possible mass of the LSP and its spin independent neutralino nuclei scattering cross section. The above implies that a very close connection exists between the composition of the LSP and what one may observe at the LHC. Indeed, correlations were given of LHC signatures with the spin independent cross section and it was found that such correlations lead to a remarkable separation of the two prominent branches where the relic density constraints on the abundance of dark matter are generally satisfied.

2. In Chapter (4), an investigation was made of a completely new way to study supersymmetric signals of new physics through the classification of the sparticle landscape of masses. A priori the hierarchies among the 32 sparticle masses can add up to as many as 10^{25-28} possibilities. However, it turns out that this number is drastically reduced if one subjects the landscape to the WMAP and other experimental constraints. Specifically, a study of the first four sparticle mass hierarchies reveals that this number reduces to a rather small set. Such analyses were carried out in the framework of mSUGRA, NUSUGRA, and in D-Brane models and less than than 50 hierarchical 4 -particle patterns were seen. The neutralino-nuclei scattering cross sections for the direct detection of dark matter were analyzed and it is found that a *spectral decomposition* of the

patterns occurs in the $\sigma^{\rm SI}_{\chi p}$ vs m_χ plane. Here the Higgs patterns (HPs) give the largest cross sections and are already being constrained by the recent data from the Xe-10 and CDMS dark matter experiments. These are followed by the chargino patterns (CPs), and then by the stau patterns (SUPs), and then by the stop patterns (SOPs) the latter having $\sigma^{\rm SI}_{\chi p}$ which are most suppressed and thus the hardest to observe experimentally. A remarkable observation of the sparticle landscape analysis is that essentially all the Higgses can be light, and sometimes even lighter than the LSP. Such patterns (HPs) give rise to rather significant Higgs $\rightarrow \tau\bar{\tau}$ signal at the hadron colliders and also give rise to a constrained signal in the Branching ratio of $B_s \rightarrow \mu^+\mu^-$. An analysis of these signals was carried out and it was found that the current data from the Tevatron is already beginning to constrain the HPs. In this regard, one observed a confluence of the constraints arising from the direct detection experiments and from the $\tau\bar{\tau}$ and flavor data from the Tevatron. Several interesting theoretical results also surfaced from this analysis.

A study of 2 classes of D-Brane models was given. Here it was found that both models can support relatively light Higgs Bosons, and specifically in one class of these models it was seen that the gaps between the various sparticle masses can be very different from one model to another. In the case of the D-Brane models it is possible to get compressed spectra, where the sparticle spectra can be significantly lighter than in the universal cases which has very important consequences for their LHC signals, as generally, the lighter the spectra, the stronger will be the LHC event rates. Finally here, we studied again correlated signatures of event rates at the LHC and dark matter direct detection cross section in the context of the landscape of sparticle mass hierarchies. It was found that the sparticle mass hierarchies act as a prism separating out both the

dark matter and the LHC signatures spaces and allow for a more general way of pin pointing the underlying model.

3. Chapter (5) began with a brief review of the Stueckelberg mechanism of mass generation for an Abelian $U(1)_X$ gauge boson . The Stueckelberg mechanism has been utilized recently to achieve a $U(1)_X$ extension of the SM and of MSSM which is characterized by the unique feature that it leads to mass generation in the electroweak sector which depends on both the Higgs mechanism and the Stueckelberg mechanism. The Stueckelberg extension of MSSM contains the possibility of a new dark matter particle (the Stino) which is R parity odd but which is a linear combination of fields mainly composed of the fields in the hidden and connector sectors. As such, its couplings with the visible sector are rather suppressed. An interesting question relates to if a Stino could satisfy the relic density constraints. This issue was investigated in Chapter (6) where it was shown that the relic density constraints consistent with the WMAP can indeed be satisfied in the parameter space of the model consistent with the current electroweak constraints.

   In Chapter (7) an investigation was carried out of the discovery potential for the Stueckelberg Z' at the Fermilab Tevatron collider using the Drell-Yan process $p\bar{p} \rightarrow Z' \rightarrow l^+l^-$. It was shown that the current data from CDF and DØ is beginning to constrain the parameter space of the Stueckelberg model. A similar analysis for the discovery potential of the Stueckelberg Z' at the LHC was carried out in Chapter (8) again using the Drell-Yan process which in this case is $pp \rightarrow Z' \rightarrow l^+l^-$. One of the many interesting issues surfacing here pertains to whether the narrow Z' from the Stueckelberg model can be distinguished from a narrow resonance arising from a massive graviton in the Randall-Sundrum

model of warped geometry. The analysis presented in Chapter (8) shows that indeed the two models of narrow resonances can be disentangled. Specifically, it was shown that the signature space of the Stueckelberg Z' model is significantly different from that of the narrow graviton of the warped geometry. This was made evident by studying both models' experimentally constrained signature spaces in the cross section - resonance mass planes and by examining the angular distributions of these models at the LHC.

4. Chapter (9) focused on an analysis of the milli charged matter that arises from the hidden sector. Here we first discussed how milli charged dark matter arises, and following this, an analysis was given of the electroweak constraints on the Stueckelberg model with both mass and kinetic mixings. It is known that the matter in the hidden sector could be a possible candidate for dark matter. We analyzed this possibility in significant detail and showed consistency of the model with the WMAP data. Correlated predictions were given on the number of di-lepton events via the Drell-Yan process and regions where WMAP constraints are satisfied. Finally, a detailed study was undertaken of the positron excess seen in cosmic rays observed by the PAMELA matter-antimatter satellite experiment. It was shown that the Stueckelberg model provides the necessary turn around to fit the excess seen in the positron spectrum, and this is precisely in the same region of the parameter space where the relic density constraints are satisfied. The model also fits the excess seen in the ATIC balloon experiment.

We end this Thesis on an optimistic note in that we stand on the edge of a new era in particle physics. The ongoing experiments at Fermilab, the onset of the LHC era, and experiments searching for dark matter, all coupled together, will shed new light on what lies beyond the SM. It is precisely this topic to which this Thesis was devoted.

Bibliography

[1] J. Wess and B. Zumino, Phys. Lett. B **49**, 52 (1974); Nucl. Phys. B **70**, 39 (1974); P. Fayet and J. Iliopoulos, Phys. Lett. B **51**, 461 (1974); A. Salam and J. A. Strathdee, Nucl. Phys. B **76**, 477 (1974); R. Haag, J. T. Lopuszanski and M. Sohnius, Nucl. Phys. B **88**, 257 (1975).

[2] P. Nath and R. Arnowitt, Phys. Lett. B **56**, 177 (1975); R. Arnowitt, P. Nath and B. Zumino, Phys. Lett. B **56**, 81 (1975); P. Nath and R. Arnowitt, Phys. Lett. B **65**, 73 (1976).

[3] D. Z. Freedman, P. van Nieuwenhuizen and S. Ferrara, Phys. Rev. D **13**, 3214 (1976); S. Deser and B. Zumino, Phys. Lett. B **62**, 335 (1976); E. Cremmer, B. Julia, J. Scherk, S. Ferrara, L. Girardello and P. van Nieuwenhuizen, Nucl. Phys. B **147**, 105 (1979).

[4] S. Dimopoulos and H. Georgi, Nucl. Phys. B **193**, 150 (1981); N. Sakai, Z. Phys. C **11**, 153 (1981). L. Girardello and M. T. Grisaru, Nucl. Phys. B **194**, 65 (1982); E. Witten, Nucl. Phys. B **202**, 253 (1982).

[5] A. H. Chamseddine, R. L. Arnowitt and P. Nath, Phys. Rev. Lett. **49**, 970 (1982).

[6] P. Nath, R. Arnowitt and A.H. Chamseddine, Applied N=1 supergravity, Trieste Lectures, 1983 (World Scientific, Singapore,1984).

[7] E. Cremmer, S. Ferrara, L. Girardello and A. Van Proeyen, Nucl. Phys. B **212**, 413 (1983).

[8] J. Polonyi, Univ. of Budapest Rep. No. KFKI-1977-93 (1977).

[9] H. P. Nilles, Phys. Lett. B **115**, 193 (1982).

[10] R. Barbieri, S. Ferrara and C. A. Savoy, Phys. Lett. B **119**, 343 (1982).

[11] P. Nath, R. L. Arnowitt and A. H. Chamseddine, Nucl. Phys. B **227**, 121 (1983).

[12] L. J. Hall, J. D. Lykken and S. Weinberg, Phys. Rev. D **27**, 2359 (1983).

[13] S. K. Soni and H. A. Weldon, Phys. Lett. B **126**, 215 (1983).

[14] G. F. Giudice and A. Masiero, Phys. Lett. B **206**, 480 (1988).

[15] I. Antoniadis, E. Gava, K. S. Narain and T. R. Taylor, Nucl. Phys. B **432**, 187 (1994).

[16] V. S. Kaplunovsky and J. Louis, Phys. Lett. B **306**, 269 (1993); A. Brignole, L. E. Ibanez and C. Munoz, Nucl. Phys. B **422**, 125 (1994).

[17] A. Brignole, L. E. Ibanez and C. Munoz, arXiv:hep-ph/9707209.

[18] G. L. Kane, "Perspectives on supersymmetry," *Singapore, Singapore: World Scientific (1998) 479 p.*

[19] L. E. Ibanez and G. G. Ross, Phys. Lett. B **110**, 215 (1982); L. Alvarez-Gaume, J. Polchinski and M. B. Wise, Nucl. Phys. B **221**, 495 (1983).

[20] J. R. Ellis, J. S. Hagelin, D. V. Nanopoulos and K. Tamvakis, Phys. Lett. B **125**, 275 (1983); L. E. Ibanez and C. Lopez, Nucl. Phys. B **233**, 511 (1984); L. E. Ibanez, C. Lopez and C. Munoz, Nucl. Phys. B **256**, 218 (1985).

[21] H. P. Nilles, Phys. Rept. **110**, 1 (1984).

[22] H. E. Haber and G. L. Kane, Phys. Rept. **117**, 75 (1985).

[23] T. R. Taylor, G. Veneziano and S. Yankielowicz, Nucl. Phys. B **218**, 493 (1983).

[24] H. Goldberg, Phys. Rev. Lett. **50**, 1419 (1983).

[25] J. R. Ellis, J. S. Hagelin, D. V. Nanopoulos, K. A. Olive and M. Srednicki, Nucl. Phys. B **238**, 453 (1984).

[26] P. Candelas, G. T. Horowitz, A. Strominger and E. Witten, Nucl. Phys. B **258**, 46 (1985).

[27] P. Nath and P. Fileviez Perez, Phys. Rept. **441**, 191 (2007) [arXiv:hep-ph/0601023].

[28] J. Ellis, S. Kelley and D. V. Nanopoulos, Phys. Lett. B249, Phys. Lett. B260, 447(1991); U. Amaldi, W. de Boer and H. Furstenau, Phys. Lett. B260, 447(1991); F. Anselmo, et. al., Nuovo Cim. 104A,1817(1991); P. Langacker and N. Polonsky, Phys. Rev. D47, 4028(1993); for a review see K. R. Dienes, Phys. Rept. **287**, 447 (1997).

[29] R. Arnowitt and P. Nath, Phys. Rev. Lett. **69**, 725 (1992); Phys. Lett. B **289**, 368 (1992); Phys. Rev. Lett. **70**, 3696 (1993); Phys. Lett. B **299**, 58 (1993).

[30] G. L. Kane, C. F. Kolda and J. D. Wells, Phys. Rev. Lett. **70**, 2686 (1993); G. L. Kane, C. F. Kolda, L. Roszkowski and J. D. Wells, Phys. Rev. D **49**, 6173 (1994).

[31] G. G. Ross and R. G. Roberts, Nucl. Phys. B **377**, 571 (1992); M. Drees and M. M. Nojiri, Nucl. Phys. B **369**, 54 (1992); V. D. Barger, M. S. Berger and P. Ohmann, Phys. Rev. D **47**, 1093 (1993); D. J. Castano, E. J. Piard and P. Ramond, Phys. Rev. D **49**, 4882 (1994).

[32] S. P. Martin and M. T. Vaughn, Phys. Rev. D **50**, 2282 (1994); I. Jack, D. R. Jones, S. P. Martin, M. T. Vaughn and Y. Yamada, Phys. Rev. D **50**, 5481 (1994).

[33] J. Wess and J. Bagger, "Supersymmetry and supergravity", *Princeton, USA: Univ. Pr. (1992) 259 p*; J. A. Bagger, arXiv:hep-ph/9604232.

[34] S. Weinberg, "The quantum theory of fields. Vol. 3: Supersymmetry," *Cambridge, UK: Univ. Pr. (2000) 419 p*;

[35] P. C. West, "Introduction to supersymmetry and supergravity," *Singapore, Singapore: World Scientific (1990) 425 p.*

[36] "Weak Scale Supersymmetry: From Superfields to Scattering Events", H. Baer and X. Tata, *Cambridge, UK: Univ. Pr. (2006) 537 p.*

[37] T. Ibrahim and P. Nath, Phys. Rev. D **57**, 478 (1998).

[38] P. Nath and R. Arnowitt, Phys. Rev. D **56** (1997) 2820; A. Corsetti and P. Nath, Phys. Rev. D **64** (2001) 125010; A. Birkedal-Hansen and B. D. Nelson, Phys. Rev. D **67**, 095006 (2003); H. Baer, A. Mustafayev, S. Profumo, A. Belyaev and X. Tata, JHEP **0507** (2005) 065.

[39] R. Blumenhagen, B. Körs, D. Lüst and T. Ott, Nucl. Phys. B **616** (2001) 3; M. Cvetic, G. Shiu and A. M. Uranga, Phys. Rev. Lett. **87** (2001) 201801 Nucl. Phys. B **615** (2001) 3; D. Cremades, L. E. Ibanez and F. Marchesano, Nucl. Phys. B **643** (2002) 93; C. Kokorelis, JHEP **0209** (2002) 029; G. Honecker and T. Ott, Phys. Rev. D **70** (2004) 126010; R. Blumenhagen, M. Cvetic, P. Langacker and G. Shiu, Ann. Rev. Nucl. Part. Sci. **55** (2005) 71.

[40] B. Kors and P. Nath, Nucl. Phys. B **681** (2004) 77.

[41] D. Lust, P. Mayr, R. Richter and S. Stieberger, Nucl. Phys. B **696**, 205 (2004); D. Lust, S. Reffert and S. Stieberger, Nucl. Phys. B **706** (2005) 3.

[42] A. Font and L. E. Ibanez, JHEP **0503**, 040 (2005).

[43] R. Blumenhagen, B. Kors, D. Lust and S. Stieberger, "Four-dimensional String Compactifications with D-Branes, Orientifolds and Fluxes," Phys. Rept. **445**, 1 (2007) [arXiv:hep-th/0610327].

[44] G. L. Kane, P. Kumar, J. D. Lykken and T. T. Wang, Phys. Rev. D **71** (2005) 115017.

[45] D. Feldman, Z. Liu and P. Nath, Phys. Lett. B **662**, 190 (2008). [arXiv:0711.4591 [hep-ph]].

[46] C. M. Chen, T. Li, V. E. Mayes and D. V. Nanopoulos, Phys. Rev. D **77**, 125023 (2008).

[47] S. P. Martin, "A Supersymmetry Primer," arXiv:hep-ph/9709356 in [18].

[48] L. E. Ibanez and G. G. Ross, Comptes Rendus Physique **8**, 1013 (2007).

[49] S. R. Coleman and E. J. Weinberg, Phys. Rev. D **7**, 1888 (1973).

[50] S. Weinberg, Phys. Rev. D **7**, 2887 (1973).

[51] G. Gamberini, G. Ridolfi and F. Zwirner, Nucl. Phys. B **331**, 331 (1990).

[52] R. L. Arnowitt, B. Dutta, T. Kamon, N. Kolev and D. A. Toback, Phys. Lett. B **639**, 46 (2006).

[53] G. L. Kane, P. Kumar and J. Shao, J. Phys. G **34**, 1993 (2007).

[54] J. P. Conlon, C. H. Kom, K. Suruliz, B. C. Allanach and F. Quevedo, JHEP **0708**, 061 (2007).

[55] H. Baer, V. Barger, G. Shaughnessy, H. Summy and L. t. Wang, Phys. Rev. D **75**, 095010 (2007).

[56] U. Chattopadhyay, D. Das, A. Datta and S. Poddar, Phys. Rev. D **76**, 055008 (2007).

[57] R. L. Arnowitt *et al.*, Phys. Lett. B **649** (2007) 73.

[58] D. Feldman, Z. Liu and P. Nath, Phys. Rev. Lett. **99**, 251802 (2007). [arXiv:0707.1873 [hep-ph]].

[59] R. L. Arnowitt, B. Dutta, A. Gurrola, T. Kamon, A. Krislock and D. Toback, Phys. Rev. Lett. **100**, 231802 (2008).

[60] D. Feldman, Z. Liu and P. Nath, JHEP **0804**, 054 (2008). [arXiv:0802.4085 [hep-ph]]

[61] G. J. Gounaris, J. Layssac and F. M. Renard, Phys. Rev. D **77**, 013003 (2008) [arXiv:0709.1789 [hep-ph]]; Phys. Rev. D **77**, 093007 (2008) [arXiv:0803.0813 [hep-ph]].

[62] S. Bhattacharya, A. Datta and B. Mukhopadhyaya, Phys. Rev. D **78**, 115018 (2008) [arXiv:0809.2012 [hep-ph]].

[63] S. P. Martin, Phys. Rev. D **78**, 055019 (2008) [arXiv:0807.2820 [hep-ph]].

[64] S. P. Martin and P. Ramond, Phys. Rev. D **48**, 5365 (1993).

[65] P. Ramond, "Journeys Beyond The Standard Model", *Westview Press (November 18, 1999), 372 p.*

[66] R. L. Arnowitt and P. Nath, arXiv:hep-ph/9309277 (select OSTI Information Bridge Server on spires).

[67] "Theory and Phenomenology of Sparticles", M. Drees, R. Godbole and P. Roy, *Hackensack, USA: World Scientific (2004) 555 p.*

[68] H. E. Haber and R. Hempfling, Phys. Rev. Lett. **66**, 1815 (1991); H. E. Haber, R. Hempfling and A. H. Hoang, Z. Phys. C **75**, 539 (1997).

[69] S. P. Martin and M. T. Vaughn, Phys. Lett. B **318**, 331 (1993).

[70] D. M. Pierce, J. A. Bagger, K. T. Matchev and R. j. Zhang, Nucl. Phys. B **491**, 3 (1997).

[71] K. L. Chan, U. Chattopadhyay and P. Nath, Phys. Rev. D **58**, 096004 (1998); J. L. Feng, K. T. Matchev and T. Moroi, Phys. Rev. Lett. **84**, 2322 (2000); H. Baer, C. Balazs, A. Belyaev, T. Krupovnickas and X. Tata, JHEP **0306**, 054 (2003). For a review see, A. B. Lahanas, N. E. Mavromatos and D. V. Nanopoulos, Int. J. Mod. Phys. D **12**, 1529 (2003).

[72] B. W. Lee and S. Weinberg, Phys. Rev. Lett. **39**, 165 (1977).

[73] K. Griest and D. Seckel, Phys. Rev. D **43**, 3191 (1991); M. Drees and M. M. Nojiri, Phys. Rev. D **47**, 376 (1993); S. Mizuta and M. Yamaguchi, Phys. Lett. B **298**, 120 (1993). J. Edsjo and P. Gondolo, Phys. Rev. D **56**, 1879 (1997); J. R. Ellis, T. Falk, K. A. Olive and M. Srednicki, Astropart. Phys. **13**, 181 (2000).

[74] K. Griest and D. Seckel, Nucl. Phys. B **283**, 681 (1987); M. Srednicki, R. Watkins and K. A. Olive, Nucl. Phys. B **310**, 693 (1988); P. Fayet, Phys. Rev. D **70**, 023514 (2004).

[75] P. Gondolo, J. Edsjo, P. Ullio, L. Bergstrom, M. Schelke and E. A. Baltz, JCAP **0407**, 008 (2004) [arXiv:astro-ph/0406204].

[76] E. W. Kolb and M. S. Turner, "The Early universe," Front. Phys. **69**, 1 (1990); *Westview Press (February 20, 1994, 592 pg.*

[77] U. Chattopadhyay, T. Ibrahim and P. Nath, Phys. Rev. D **60**, 063505 (1999).

[78] J. R. Ellis, A. Ferstl and K. A. Olive, Phys. Lett. B **481**, 304 (2000); J. R. Ellis, K. A. Olive and C. Savage, Phys. Rev. D **77**, 065026 (2008).

[79] T. Sjostrand, S. Mrenna, P. Skands, JHEP **0605**, 026 (2006).

[80] F. E. Paige, S. D. Protopopescu, H. Baer and X. Tata, arXiv:hep-ph/0312045.

[81] P. Nath, R. Arnowitt and A. H. Chamseddine, HUTP-83/A077; D. A. Dicus, S. Nandi, W. W. Repko and X. Tata, Phys. Rev. Lett. **51**, 1030 (1983).

[82] H. Baer and X. Tata, Phys. Lett. B **155**, 278 (1985); H. Baer, K. Hagiwara and X. Tata, Phys. Rev. Lett. **57**, 294 (1986).

[83] P. Nath and R. Arnowitt, Mod. Phys. Lett. A **2** (1987) 331.

[84] R. Arnowitt, R. M. Barnett, P. Nath and F. Paige, Int. J. Mod. Phys. A **2**, 1113 (1987); H. Baer, C. h. Chen, F. Paige and X. Tata, Phys. Rev. D **50**, 4508 (1994); V. D. Barger, C. Kao and T. j. Li, Phys. Lett. B **433**, 328 (1998); H. Baer, M. Drees, F. Paige, P. Quintana and X. Tata, Phys. Rev. D **61** (2000) 095007.

[85] H. Baer, C. h. Chen, F. Paige and X. Tata, Phys. Rev. D **52**, 2746 (1995); U. Chattopadhyay, A. Datta, A. Datta, A. Datta and D. P. Roy, Phys. Lett. B **493**, 127 (2000); P. G. Mercadante, J. K. Mizukoshi and X. Tata, Phys. Rev. D **72**, 035009 (2005); R. H. K. Kadala, P. G. Mercadante, J. K. Mizukoshi and X. Tata, Eur. Phys. J. C **56**, 511 (2008).

[86] J. D. Lykken and K. T. Matchev, Phys. Rev. D **61**, 015001 (2000); A. Dedes, H. K. Dreiner, U. Nierste and P. Richardson, arXiv:hep-ph/0207026.

[87] D. Feldman, Z. Liu and P. Nath, Phys. Rev. D **78**, 083523 (2008) [arXiv:0808.1595 [hep-ph]].

[88] R. N. Mohapatra, "Unification and Supersymmetry", *Springer; 3rd edition (2002) 405 p.*

[89] P. Nath, arXiv:hep-ph/0307123.

[90] D. Clowe, M. Bradac, A. H. Gonzalez, M. Markevitch, S. W. Randall, C. Jones and D. Zaritsky, "A direct empirical proof of the existence of dark matter," Astrophys. J. **648**, L109 (2006) [arXiv:astro-ph/0608407].

[91] D. N. Spergel *et al.* Astrophys. J. Suppl. **170**, 377 (2007).

[92] U. Chattopadhyay, A. Corsetti and P. Nath, Phys. Rev. D **68**, 035005 (2003).

[93] P. Nath and R. L. Arnowitt, Phys. Rev. Lett. **70**, 3696 (1993); Phys. Lett. B **299**, 58 (1993); J. L. Lopez, D. V. Nanopoulos and K. j. Yuan, Phys. Rev. D **48**, 2766 (1993); H. Baer and M. Brhlik, Phys. Rev. D **53**, 597 (1996); V. D. Barger and C. Kao, Phys. Rev. D **57**, 3131 (1998).

[94] A. Djouadi, J. L. Kneur and G. Moultaka, Comput. Phys. Commun. **176**, 426 (2007).

[95] G. Belanger, F. Boudjema, A. Pukhov and A. Semenov, Comput. Phys. Commun. **177**, 894 (2007);arXiv:0803.2360 ; Comput. Phys. Commun. **176**, 367 (2007); Comput. Phys. Commun. **174**, 577 (2006); Comput. Phys. Commun. **149**, 103 (2002);

[96] P. Skands *et al.*, JHEP **0407**, 036 (2004).

[97] PGS4, J. Conway, et. al.

[98] Z. Ahmed *et al.* [CDMS Collaboration], arXiv:0802.3530 [astro-ph]; J. Angle *et al.* [XENON Collaboration], Phys. Rev. Lett. **100**, 021303 (2008).

[99] R. W. Schnee *et al.* [The SuperCDMS Collaboration], arXiv:astro-ph/0502435.

[100] H. Baer, C. Balazs, A. Belyaev and J. O'Farrill, JCAP **0309**, 007 (2003) [arXiv:hep-ph/0305191].

[101] H. Baer, A. Mustafayev, E. K. Park and X. Tata, JCAP **0701** (2007) 017.

[102] T. Yetkin and M. Spiropulu [CMS Collaboration], Acta Phys. Polon. B **38** (2007) 661.

[103] M. Biglietti *et al.*, CERN-ATL-PHYS-PUB-2007-004; ATL-COM-PHYS-2006-095;ATL-PHYS-CONF-2007-020; ATL-COM-PHYS-2007-078.

[104] A. Migliaccio [ATLAS Collaboration], Diploma Thesis.

[105] B. Mura [CMS Collaboration], Diploma Thesis.

[106] D. Feldman, Z. Liu and P. Nath, "Recent Developments in Supersymmetric and Hidden Sector Dark Matter," AIP Conf. Proc. **1078**, 116 (2009) [arXiv:0806.4683 [hep-ph]].

[107] P. Nath, "High Scale Physics Connection to LHC Data," arXiv:0812.0954 .

[108] B. C. Allanach *et al.*, [arXiv:hep-ph/0202233].

[109] M. Battaglia, A. De Roeck, J. R. Ellis, F. Gianotti, K. A. Olive and L. Pape, Eur. Phys. J. C **33**, 273 (2004).

[110] G. L. Bayatian *et al.* [CMS Collaboration], J. Phys. G **34**, 995 (2007).

[111] R. Bernabei *et al.*, Phys. Lett. B **389** (1996) 757.

[112] V. Sanglard *et al.* [The EDELWEISS Collaboration], Phys. Rev. D **71** (2005) 122002.

[113] D. S. Akerib *et al.* [CDMS Collaboration], Phys. Rev. Lett. **96** (2006) 011302.

[114] G. J. Alner *et al.*, Astropart. Phys. **28** (2007) 287; Astropart. Phys. **23** (2005) 444.

[115] J. Angle *et al.* [XENON Collaboration], Phys. Rev. Lett. **100**, 021303 (2008).

[116] T. Stiegler et.al., Fall Meeting of the Texas Sections of the APS and AAPT, 2007.

[117] G. L. Kane, B. D. Nelson, T. T. Wang and L. T. Wang, arXiv:hep-ph/0304134.

[118] M. S. Carena, S. Heinemeyer, C. E. M. Wagner and G. Weiglein, Eur. Phys. J. C **45**, 797 (2006); Phys. Rev. Lett. **97**, 051801 (2006); M. S. Carena, A. Menon and C. E. M. Wagner, Phys. Rev. D **76**, 035004 (2007).

[119] A. Belyaev, A. Blum, R. S. Chivukula and E. H. Simmons, Phys. Rev. D **72**, 055022 (2005); T. Hahn, S. Heinemeyer, F. Maltoni, G. Weiglein and S. Willenbrock, arXiv:hep-ph/0607308; U. Aglietti *et al.*, "Tevatron-for-LHC Report: Higgs," arXiv:hep-ph/0612172.

[120] J. R. Ellis, S. Heinemeyer, K. A. Olive and G. Weiglein, Phys. Lett. B **653**, 292 (2007).

[121] G. Barenboim, P. Paradisi, O. Vives, E. Lunghi and W. Porod, JHEP **0804**, 079 (2008) [arXiv:0712.3559 [hep-ph]].

[122] M. Spira, A. Djouadi, D. Graudenz and P. M. Zerwas, Nucl. Phys. B **453**, 17 (1995); A. Djouadi, Phys. Rept. **459**, 1 (2008).

[123] J. Campbell, R. K. Ellis, F. Maltoni and S. Willenbrock, Phys. Rev. D **67** (2003) 095002; R. V. Harlander and W. B. Kilgore, Phys. Rev. D **68**, 013001 (2003); F. Maltoni, Z. Sullivan and S. Willenbrock, Phys. Rev. D **67** (2003) 093005; S. Dawson, C. B. Jackson, L. Reina and D. Wackeroth, Mod. Phys. Lett. A **21** (2006) 89.

[124] V. M. Abazov *et al.* [D0 Collaboration], Phys. Rev. Lett. **97**, 121802 (2006).

[125] S. R. Choudhury and N. Gaur, Phys. Lett. B **451**, 86 (1999); K. S. Babu and C. Kolda, Phys. Rev. Lett. **84**, 228 (2000); A. Dedes, H. K. Dreiner, U. Nierste, and P. Richardson, Phys. Rev. Lett. **87**, 251804 (2001); R. Arnowitt, B. Dutta, T. Kamon and M. Tanaka, Phys. Lett. B **538** (2002) 121; S. Baek, P. Ko, and W. Y. Song, JHEP **0303**, 054 (2003); J. K. Mizukoshi, X. Tata and Y. Wang, Phys. Rev. D **66**, 115003 (2002); T. Ibrahim and P. Nath, Phys. Rev. D **67**, 016005 (2003).

[126] A. J. Buras, P. H. Chankowski, J. Rosiek and L. Slawianowska, Nucl. Phys. B **619**, 434 (2001); [arXiv:hep-ph/0107048]. G. Isidori and A. Retico, JHEP **0111** (2001) 001; A. J. Buras, P. H. Chankowski, J. Rosiek and L. Slawianowska, Phys. Lett. B **546**, 96 (2002); A. J. Buras, P. H. Chankowski, J. Rosiek and L. Slawianowska, Nucl. Phys. B **659**, 3 (2003).

[127] C. Bobeth, T. Ewerth, F. Kruger and J. Urban, Phys. Rev. D **64**, 074014 (2001).

[128] T. C. Yuan, R. Arnowitt, A. H. Chamseddine and P. Nath, Z. Phys. C **26**, 407 (1984); D. A. Kosower, L. M. Krauss and N. Sakai, Phys. Lett. B **133**, 305 (1983); J.L. Lopez, D.V. Nanopoulos, X. Wang, Phys. Rev. **D49**, 366(1994); U. Chattopadhyay and P. Nath, Phys. Rev. D **53**, 1648 (1996); T. Ibrahim and P. Nath, Phys. Rev. D **61**, 095008 (2000).

[129] G. W. Bennett *et al.* [Muon g-2 Collaboration], Phys. Rev. Lett. **92** (2004) 161802.

[130] K. Hagiwara, A. D. Martin, D. Nomura and T. Teubner, Phys. Lett. B **649** (2007) 173.

[131] L. E. Ibanez, F. Marchesano and R. Rabadan, JHEP **0111**, 002 (2001).

[132] D. M. Ghilencea, L. E. Ibanez, N. Irges and F. Quevedo, JHEP **0208** (2002) 016; D. M. Ghilencea, Nucl. Phys. B **648** (2003) 215.

[133] D. Feldman, P. Nath et. al, [in preparation].

[134] P. Nath and T. R. Taylor, Phys. Lett. B **548**, 77 (2002) [arXiv:hep-ph/0209282].

[135] M. Atac *et al.*, New Astron. Rev. **49** (2005) 283.

[136] E. Barberio *et al.*, HFAG Collaboration], arXiv:0704.3575 [hep-ex].

[137] M. Misiak *et al.*, Phys. Rev. Lett. **98** (2007) 022002.

[138] G. Degrassi, P. Gambino and G. F. Giudice, JHEP **0012** (2000) 009; A. J. Buras et.al., Nucl. Phys. B **659** (2003) 3; M. E. Gomez, T. Ibrahim, P. Nath and S. Skadhauge, Phys. Rev. D **74** (2006) 015015; G. Degrassi, P. Gambino and P. Slavich, Phys. Lett. B **635** (2006) 335.

[139] A. Abulencia *et al.* [CDF Collaboration], Phys. Rev. Lett. **95** (2005) 221805.

[140] CDF Public Note 8956; DØ Conference Note 5344-CONF.

[141] R. Barate *et al.,* Phys. Lett. B **565**, 61 (2003); LHWG-Note 2005-01; G. Abbiendi *et al.* [OPAL Collaboration], arXiv:0707.0373 [hep-ex].

[142] G. Abbiendi *et al.* [OPAL Collaboration], Eur. Phys. J. C **35**, 1 (2004).

[143] A. Djouadi, M. Drees and J. L. Kneur, JHEP **0603**, 033 (2006).

[144] W. Porod, Comput. Phys. Commun. **153**, 275 (2003).

[145] B. C. Allanach, Comput. Phys. Commun. **143**, 305 (2002).

[146] H. Baer, J. Ferrandis, S. Kraml and W. Porod, Phys. Rev. D **73**, 015010 (2006).

[147] G. Belanger, S. Kraml and A. Pukhov, Phys. Rev. D **72**, 015003 (2005).

[148] B. C. Allanach, A. Djouadi, J. L. Kneur, W. Porod and P. Slavich, JHEP **0409**, 044 (2004).

[149] B. C. Allanach, S. Kraml and W. Porod, JHEP **0303**, 016 (2003).

[150] C. F. Berger, J. S. Gainer, J. L. Hewett and T. G. Rizzo, JHEP **0902**, 023 (2009) [arXiv:0812.0980 [hep-ph]].

[151] B. C. Allanach, K. Cranmer, C. G. Lester and A. M. Weber, JHEP **0708**, 023 (2007) [arXiv:0705.0487 [hep-ph]].

[152] J. A. Maxin, V. E. Mayes and D. V. Nanopoulos, arXiv:0809.3200 [hep-ph].

[153] K. Hagiwara, A. D. Martin, D. Nomura and T. Teubner, Phys. Lett. B **649**, 173 (2007).

[154] W. Beenakker, M. Klasen, M. Kramer, T. Plehn, M. Spira and P. M. Zerwas, Phys. Rev. Lett. **83**, 3780 (1999).

[155] S. Jadach, Z. Was, R. Decker and J. H. Kuhn, Comput. Phys. Commun. **76**, 361 (1993).

[156] CMS Collaboration, CERN/LHCC 2006-001 (2006).

[157] M. Chiorboli, M. Galanti, A. Tricomi, CERN-CMS-NOTE-2006-133; D. J. Mangeol, U. Goerlach, CERN-CMS-NOTE-2006-096.

[158] W. de Boer et. al, CERN-CMS-NOTE-2006-113.

[159] D. E. Acosta *et al.* [CDF Collaboration], Phys. Rev. D **71**, 052003 (2005).

[160] M. B. Green and J. H. Schwarz, Phys. Lett. B **149**, 117 (1984).

[161] M. Kalb and P. Ramond, Phys. Rev. D **9**, 2273 (1974).

[162] E. Cremmer and J. Scherk, Nucl. Phys. B **72** (1974) 117.

[163] T. J. Allen, M. J. Bowick and A. Lahiri, Mod. Phys. Lett. A **6**, 559 (1991).

[164] E.C.G. Stueckelberg, Helv. Phys. Acta. **11** (1938) 225; V. I. Ogievetskii and I.V. Polubarinov, JETP **14** (1962) 179.

[165] P. W. Higgs, Phys. Lett. **12** (1964) 132; Phys. Rev. Lett. **13** (1964) 508; Phys. Rev. **145** (1966) 1156. See also: G. S. Guralnik, C. R. Hagen and T. W. B. Kibble, Phys. Rev. Lett. **13** (1964) 585; F. Englert and R. Brout, Phys. Rev. Lett. **13** (1964) 321.

[166] F. Cianfrani and O. M. Lecian, 'E.C.G. Stueckelberg: a forerunner of modern physics II," Int. J. Mod. Phys. A **23**, 1105 (2008).

[167] B. Körs and P. Nath, Phys. Lett. B **586**, 366 (2004); [hep-ph/0402047].

[168] B. Kors and P. Nath, "A supersymmetric Stueckelberg U(1) extension of the MSSM," JHEP **0412**, 005 (2004); [arXiv:hep-ph/0406167].

[169] B. Kors and P. Nath, "Aspects of the Stueckelberg extension," JHEP **0507**, 069 (2005); [arXiv:hep-ph/0503208].

[170] D. Feldman, Z. Liu and P. Nath, Phys. Rev. Lett. **97**, 021801 (2006) [arXiv:hep-ph/0603039].

[171] D. Feldman, Z. Liu and P. Nath, JHEP **0611**, 007 (2006) [arXiv:hep-ph/0606294].

[172] D. Feldman, B. Kors and P. Nath, Phys. Rev. D **75**, 023503 (2007) [arXiv:hep-ph/0610133].

[173] K. Cheung and T. C. Yuan, JHEP **0703**, 120 (2007) [arXiv:hep-ph/0701107].

[174] D. Feldman, Z. Liu and P. Nath, Phys. Rev. D **75**, 115001 (2007) [arXiv:hep-ph/0702123].

[175] D. Feldman, Z. Liu and P. Nath, Phys. Rev. D **79**, 063509 (2009) arXiv:0810.5762 [[hep-ph]].

[176] I. Antoniadis, E. Kiritsis and T. N. Tomaras, Phys. Lett. B **486**, 186 (2000); D. Cremades, L. E. Ibanez and F. Marchesano, arXiv:hep-ph/0212048; L. E. Ibanez, F. Marchesano and R. Rabadan, JHEP **0111** (2001) 002; I. Antoniadis, E. Kiritsis and J. Rizos, Nucl. Phys. B **637**, 92 (2002) [arXiv:hep-th/0204153]. R. Blumenhagen, V. Braun, B. Körs and D. Lüst, hep-th/0210083.

[177] C. Coriano', N. Irges and E. Kiritsis, Nucl. Phys. B **746**, 77 (2006); R. Armillis, C. Coriano and M. Guzzi, JHEP **0805**, 015 (2008) [arXiv:0711.3424 [hep-ph]].

[178] P. Anastasopoulos, T. P. T. Dijkstra, E. Kiritsis and A. N. Schellekens, Nucl. Phys. B **759** (2006) 83 [arXiv:hep-th/0605226].

[179] J. De Rydt, T. T. Schmidt, M. Trigiante, A. Van Proeyen and M. Zagermann, JHEP **0812**, 105 (2008); M. Zagermann, arXiv:0801.1666 [hep-th].

[180] S. A. Abel, M. D. Goodsell, J. Jaeckel, V. V. Khoze and A. Ringwald, JHEP **0807**, 124 (2008) [arXiv:0803.1449 [hep-ph]].

[181] B. Holdom, Phys. Lett. B **166**, 196 (1986); Phys. Lett. B **259**, 329 (1991).

[182] K. S. Babu, C. F. Kolda and J. March-Russell, Phys. Rev. D **57**, 6788 (1998).

[183] P. Nath, arXiv:0812.0958 [hep-ph]; P. Langacker, arXiv:0801.1345 [hep-ph]; D. Feldman, Z. Liu and P. Nath, AIP Conf. Proc. **939**, 50 (2007) [arXiv:0705.2924 [hep-ph]]; K. m. Cheung and T. C. Yuan, arXiv:0710.2005 [hep-ph]; P. Nath, arXiv:hep-ph/0610414;

[184] B. Kors and P. Nath, "How Stueckelberg extends the standard model and the MSSM," arXiv:hep-ph/0411406.

[185] P. Nath, Phys. Rev. Lett. **76**, 2218 (1996).

[186] G. R. Dvali and A. Pomarol, Phys. Rev. Lett. **77**, 3728 (1996).

[187] B. Kors and P. Nath, Nucl. Phys. B **711**, 112 (2005) [arXiv:hep-th/0411201].

[188] P. Nath and M. Yamaguchi, Phys. Rev. D **60**, 116004 (1999); M. Masip and A. Pomarol, Phys. Rev. D **60**, 096005 (1999);R. Casalbuoni, S. De Curtis, D. Dominici and R. Gatto, Phys. Lett. B **462**, 48 (1999);T. G. Rizzo and J. D. Wells, Phys. Rev. D **61**, 016007 (2000); C. D. Carone, Phys. Rev. D **61**, 015008 (2000).

[189] W. J. Marciano, Phys. Rev. D **60**, 093006 (1999).

[190] W. J. Marciano and A. Sirlin, Phys. Rev. D **29**, 945 (1984).

[191] [ALEPH Collaboration], [arXiv:hep-ex/0509008].

[192] W. F. Chang, J. N. Ng and J. M. S. Wu, Phys. Rev. D **74** (2006) 095005.

[193] J. Kumar and J. D. Wells, Phys. Rev. D **74**, 115017 (2006).

[194] See: K. Griest and D. Seckel first Ref. of [73].

[195] F. Fucito, A. Lionetto, A. Mammarella and A. Racioppi, arXiv:0811.1953

[196] See: R. Arnowitt and P. Nath, first Ref. of [29].

[197] P. Nath, J. z. Wu and R. Arnowitt, Phys. Rev. D **52** (1995) 4169; B. Allanach, S. Kraml and W. Porod, J. R. Ellis, K. A. Olive, Y. Santoso and V. C. Spanos, Phys. Rev. D **69**, 095004 (2004); M. E. Gomez, T. Ibrahim, P. Nath and S. Skadhauge, Phys. Rev. D **70**, 035014 (2004).

[198] R. N. Mohapatra and G. Senjanovic, Phys. Rev. Lett. **44**, 912 (1980).

[199] R. Hamberg, W. L. van Neerven and T. Matsuura,' Nucl. Phys. B **359**, 343 (1991).

[200] U. Baur, O. Brein, W. Hollik, C. Schappacher and D. Wackeroth, Phys. Rev. D **65**, 033007 (2002).

[201] M. Carena, A. Daleo, B. A. Dobrescu and T. M. P. Tait, Phys. Rev. D **70**, 093009 (2004).

[202] J. Pumplin, D. R. Stump, J. Huston, H. L. Lai, P. Nadolsky and W. K. Tung, JHEP **0207**, 012 (2002).

[203] A. Abulencia *et al.* [CDF Collaboration], Phys. Rev. Lett. **95**, 252001 (2005).

[204] V. M. Abazov *et al.* [DØ Collaboration], Phys. Rev. Lett. **95**, 091801 (2005).

[205] For reviews see: J. L. Hewett and T. G. Rizzo, Phys. Rept. **183**, 193 (1989); M. Cvetic and P. Langacker, arXiv:hep-ph/9707451 in [18]; A. Leike, Phys. Rept. **317**, 143 (1999); P. Langacker, arXiv:0801.1345 [hep-ph].

[206] V. M. Abazov *et al.* [D0 Collaboration], Phys. Lett. B **641**, 415 (2006).

[207] L. Randall and R. Sundrum, Phys. Rev. Lett. **83**, 3370 (1999).

[208] H. Davoudiasl, J. L. Hewett and T. G. Rizzo, Phys. Rev. Lett. **84**, 2080 (2000).

[209] Information is available at http://www-cdf.fnal.gov/∼harper/diEleAna.html .

[210] A. Abulencia *et al.* [CDF Collaboration], Phys. Rev. Lett. **96**, 211801 (2006).

[211] O. Stelzer-Chilton [CDF Collaboration and D0 Collaboration], arXiv:0810.4754 [hep-ex]. T. Aaltonen *et al.* [CDF Collaboration], Phys. Rev. Lett. **102**, 031801 (2009) [arXiv:0810.2059 [hep-ex]]; K. Hatakeyama [CDF Collaboration], arXiv:0810.3681 [hep-ex]; T. Aaltonen *et al.* [CDF Collaboration], arXiv:0811.0053 [hep-ex].

[212] T. Appelquist, H. C. Cheng and B. A. Dobrescu, Phys. Rev. D **64**, 035002 (2001); M. Battaglia, A. Datta, A. De Roeck, K. Kong and K. T. Matchev, JHEP **0507**, 033 (2005); G. Burdman, B. A. Dobrescu and E. Ponton, Phys. Rev. D **74**, 075008 (2006).

[213] A. Ferroglia, A. Lorca and J. J. van der Bij, Annalen Phys. **16**, 563 (2007).

[214] T. Han, Z. Si, K. M. Zurek and M. J. Strassler, JHEP **0807**, 008 (2008) [arXiv:0712.2041 [hep-ph]].

[215] P. Anastasopoulos, F. Fucito, A. Lionetto, G. Pradisi, A. Racioppi and Y. S. Stanev, Phys. Rev. D **78** (2008) 085014 [arXiv:0804.1156 [hep-th]].

[216] S. Cassel, D. M. Ghilencea and G. G. Ross, arXiv:0903.1118 [hep-ph].

[217] J. Kang and P. Langacker, Phys. Rev. D **71**, 035014 (2005).

[218] M. Dittmar, A. S. Nicollerat and A. Djouadi, Phys. Lett. B **583**, 111 (2004).

[219] "ATLAS: Detector and physics performance, technical design report. Volume 1," CERN-LHCC-99-14
"ATLAS detector and physics performance, technical design report. Vol. 2," CERN-LHCC-99-15 .

[220] CMS Collaboration, "The CMS Physics Technical Design Report, Volume 1," CERN/LHCC 2006-001 (2006). CMS TDR 8.1 .
CMS Collaboration, "The CMS Physics Technical Design Report, Volume 2," CERN/LHCC 2006-021 (2006). CMS TDR 8.2 .

[221] R. Cousins, J. Mumford, V. Valuev, "Detection of Z' gauge bosons in the dimuon decay mode" in CMS, CMS Note 2005/002.

[222] S. Eidelman *et al.* [Particle Data Group], Phys. Lett. B **592**, 1 (2004).

[223] P. Osland, A. A. Pankov, N. Paver and A. V. Tsytrinov, Phys. Rev. D **78**, 035008 (2008).

[224] S. Godfrey, eConf **C010630**, P344 (2001).

[225] M. Cvetic and S. Godfrey, arXiv:hep-ph/9504216.

[226] M. Gogberashvili, Int. J. Mod. Phys. D **11**, 1635 (2002).

[227] A. V. Kisselev, Phys. Rev. D **73**, 024007 (2006).

[228] T. Han, J. D. Lykken and R. J. Zhang, Phys. Rev. D **59**, 105006 (1999).

[229] G. F. Giudice, R. Rattazzi and J. D. Wells, Nucl. Phys. B **544**, 3 (1999).

[230] J. Bijnens, P. Eerola, M. Maul, A. Mansson and T. Sjostrand, Phys. Lett. B **503**, 341 (2001).

[231] E. Dvergsnes, P. Osland and N. Ozturk, Phys. Rev. D **67**, 074003 (2003); T. Buanes, E. W. Dvergsnes and P. Osland, Eur. Phys. J. C **35**, 555 (2004).

[232] P. Mathews, V. Ravindran, K. Sridhar and W. L. van Neerven, Nucl. Phys. B **713**, 333 (2005); P. Mathews, V. Ravindran and K. Sridhar, JHEP **0510**, 031 (2005); P. Mathews and V. Ravindran, Nucl. Phys. B **753**, 1 (2006).

[233] B. C. Allanach, K. Odagiri, M. A. Parker and B. R. Webber, JHEP **0009**, 019 (2000).

[234] M. Schafer, F, Ledroit, and B. Tracome, "$Z' \to e^+e^-$ studies in full simulation (DCI)", ATL-PHYS-PUB-2005-010.

[235] T. G. Rizzo, eConf **C960625**, NEW136 (1996).

[236] P. Traczyk and G. Wrochna, arXiv:hep-ex/0207061.

[237] C. Collard and M. C. Lemaire, Eur. Phys. J. C **40N5**, 15 (2005).

[238] M.-C. Lemaire , V. Litvin , H. Newman "Search for Randall-Sundrum excitations of gravitons decaying into two photons for CMS at LHC" CMS Note 2006/051

[239] M. E. Peskin and T. Takeuchi, Phys. Rev. D **46**, 381 (1992).

[240] G. Altarelli, R. Barbieri and S. Jadach, Nucl. Phys. B **369**, 3 (1992).

[241] H. Davoudiasl, J. L. Hewett and T. G. Rizzo, Phys. Rev. D **63**, 075004 (2001).

[242] B. C. Allanach, K. Odagiri, M. J. Palmer, M. A. Parker, A. Sabetfakhri and B. R. Webber, JHEP **0212**, 039 (2002).

[243] R. Cousins, J. Mumford, J. Tucker and V. Valuev, JHEP **0511**, 046 (2005).

[244] D. Y. Bardin,M. Grunewald and G. Passarino, [arXiv:hep-ph/9902452].

[245] J. Erler and P. Langacker, [arXiv:hep-ph/0407097].

[246] [LEP Collaboration], arXiv:hep-ex/0312023; [ALEPH Collaboration], arXiv:hep-ex/0609051.

[247] M. L. Perl, P. C. Kim, V. Halyo, E. R. Lee, I. T. Lee, D. Loomba and K. S. Lackner, Int. J. Mod. Phys. A **16**, 2137 (2001) [arXiv:hep-ex/0102033].

[248] M. Ahlers, J. Jaeckel, J. Redondo and A. Ringwald, Phys. Rev. D **78**, 075005 (2008) [arXiv:0807.4143 [hep-ph]].

[249] CDF Public Note : CDF/ANAL/EXOTIC/8421.

[250] O. Adriani *et al.*, arXiv:0810.4995 [astro-ph] (Submitted to Nature).

[251] D. Feldman, Z. Liu and P. Nath, Phys. Rev. D **79**, 063509 (2009) arXiv:0810.5762 [[hep-ph]].

[252] J. Chang *et al.*, Nature **456**, 362 (2008).

[253] S. W. Barwick *et al.* [HEAT Collaboration], Astrophys. J. **482**, L191 (1997); M. Aguilar *et al.* [AMS-01 Collaboration], Phys. Lett. B **646** (2007) 145.

[254] P. Grajek, G. Kane, D. J. Phalen, A. Pierce and S. Watson, arXiv:0807.1508 .

[255] T. Delahaye, R. Lineros, F. Donato, N. Fornengo and P. Salati, Phys. Rev. D **77**, 063527 (2008); P. Brun et. al, G. Bertone, J. Lavalle, P. Salati and R. Taillet, Phys. Rev. D **76**, 083506 (2007).

[256] M. Cirelli, R. Franceschini and A. Strumia, Nucl. Phys. B **800**, 204 (2008).

[257] V. Barger, W. Y. Keung, D. Marfatia and G. Shaughnessy, Phys. Lett. B **672**, 141 (2009).

[258] P. Grajek, G. Kane, D. Phalen, A. Pierce and S. Watson, arXiv:0812.4555 .

[259] K. Cheung, P. Y. Tseng and T. C. Yuan, arXiv:0902.4035 [hep-ph].

[260] M. Kamionkowski and S. M. Koushiappas, Phys. Rev. D **77**, 103509 (2008).

[261] M. S. Longair, *Cambridge, UK: Univ. Pr. (1994) 393 p.*

[262] J. Hisano, S. Matsumoto, O. Saito, M. Senami, Phys. Rev. D **73** (2006) 055004.

[263] J. F. Navarro et. al, C. S. Frenk and S. D. M. White, Astrophys. J. **490**, 493 (1997); B. Moore, T. R. Quinn, F. Governato, J. Stadel and G. Lake, Mon. Not. Roy. Astron. Soc. **310**, 1147 (1999).

[264] M. Cirelli, M. Kadastik, M. Raidal and A. Strumia, arXiv:0809.2409 [hep-ph].

[265] I. V. Moskalenko and A. W. Strong, Astrophys. J. **493**, 694 (1998).

[266] E. A. Baltz and J. Edsjo, Phys. Rev. D **59**, 023511 (1999).

[267] O. Adriani *et al.*, Phys. Rev. Lett. **102**, 051101 (2009).

[268] A. Bottino, C. Favero, N. Fornengo and G. Mignola, Astropart. Phys. **3**, 77 (1995); L. Bergstrom, J. Edsjo and P. Ullio, Astrophys. J. **526**, 215 (1999); T. Bringmann and P. Salati, Phys. Rev. D **75**, 083006 (2007); A. Bottino, F. Donato, N. Fornengo and P. Salati, Phys. Rev. D **58**, 123503 (1998); J. Lavalle, Q. Yuan, D. Maurin and X. J. Bi, arXiv:0709.3634 [astro-ph].